UNIVERSITY OF MANITOBA

Early-Age Cracking of Concrete Bridge Deck Slabs Reinforced with GFRP Bars

by

Amir Ghatefar

A Thesis submitted to the Faculty of Graduate Studies of the University of Manitoba in partial fulfillment of the requirements of the degree of

DOCTOR OF PHILOSOPHY

Department of Civil Engineering
University of Manitoba
Winnipeg, Manitoba, Canada

ABSTRACT

Since concrete bridge deck slabs are much longer in the traffic direction, they experience transverse early-age cracks due to volumetric instability and restraint. In the last decade, the lower cost of the non-corrodible Glass Fiber Reinforced Polymer (GFRP) bars, as alternative to steel reinforcement, has made them attractive to the bridge construction industry. However, low modulus of GFRP bars may lead to wider cracks in GFRP-RC structures. This serviceability issue can be aggravated by harsh environmental conditions. Hence, the main objective of this thesis is to investigate the effect of early-age cracking in restraint bridge deck slabs reinforced with GFRP bars subjected to different environments. This research consists of two phases: an experimental investigation and a numerical study. In the experimental phase, four full-scale cast-in-place slabs reinforced with different longitudinal GFRP reinforcement ratios (0.30, 0.50, 0.70 and 1.1%) and one with steel reinforcement ratio of 0.7% measuring 2500 mm long × 765 mm wide × 180 mm thick were constructed and tested in the laboratory. Three environmental conditions were implemented; normal (laboratory) adiabatic conditions as well as freezing-thawing and wetting-drying cycles. The main test results are presented in terms of cracking pattern, width and spacing, and strains in the reinforcement and concrete. Test results indicated that the minimum reinforcement ratio (0.7%) recommended by CHBDC for bridge deck slabs reinforced with GFRP bars satisfied the serviceability requirements after being subjected to the simulated exposures of normal laboratory conditions, freezing-thawing, and wetting-drying cycles. In the numerical phase of this research, a finite element model (FEM) was constructed using ATENA software package (ver. 5) to simulate the behaviour of the test specimens. According to the FEM results, a reinforcement ratio of 0.45% Carbon FRP (CFRP) can control the early-age crack width and reinforcement strain in CFRP-RC members subjected to restrained

shrinkage. Also, the results indicated that changing the bar surface texture (sand-coated and ribbed bars) or concrete cover had an insignificant effect on the early-age crack behavior of FRP-RC bridge deck slabs subjected to shrinkage. However, reducing bar spacing and concrete strength resulted in a decrease in crack width and reinforcement strain.

ACKNOWLEDGMENT

In the name of **GOD**

I would like to express my deepest gratitude to my supervisor, Dr. Ehab El-Salakawy, P.Eng., Professor of Civil Engineering and Canada Research Chair in Durability and modernization of Civil Structures in the Department of Civil Engineering at the University of Manitoba. I greatly appreciated his open door policy whenever problems, of which there were many, arose. He was the one who initiated the idea of this research and he has been always my first resource for creative ideas and helpful advices. Also, I would like to expresses my gratitude to my co-advisor Dr. Mohamed Bassuoni, P.Eng., Associate Professor in the Department of Civil Engineering at the University of Manitoba, for his encouragement and insightful and thoughtful feedbacks. His deep, broad knowledge and experience have been of great value to me. This thesis would not have been possible without his support.

In addition, the author would like to thank his colleagues for their support during all work stages. Also, the assistance of the McQuade Heavy Structures Laboratory manager, Mr. Chad Klowak, P.Eng and the technicians, Mr. Brendan Pachal and Mr. Grant Whiteside for providing valuable technical support for the construction and testing of the specimens is greatly acknowledged.

The financial support provided by the Natural Science and Engineering Research Council of Canada (NSERC) through Canada Research Chairs (CRC) program and the Network of Centers of Excellence on Intelligent Sensing for Innovative Structures (ISIS Canada) are gratefully appreciated.

Finally, I would like to acknowledge the undeniable role that my family had in all my life and also in the past four years in the completion of my graduate studies. Mom and Dad, you were always very supportive for the decisions that I have made in my life. Special thanks to my wife

"Mehrnaz" for her endless and enduring love and support. Raheleh, you are the best sister anyone can have. I love you all and I am always grateful for having such a wonderful family.

Amir Ghatefar

NOTATIONS

A_c: A_{gross} - A_{frp}

A_{gross}: overall gross section area of member (mm^2)

AF: effect of air flow on concrete shrinkage (με)

A_{GFRP}: total GFRP section area (mm^2)

A_s: steel bar section area (mm^2)

CFRP: carbon fiber reinforced polymer

C_1: $\frac{2s_0}{3L - 2s_0}$

C_{th}: coefficient of thermal expansion ($\times 10^{-6}$/°C)

d_b: re-bar diameter (mm)

d: effective depth (mm)

dt: temperature difference with respect to interior temperature (°C)

$E_{c\,(day)}$: concrete modulus of elasticity at different age (days)

$E_{c\,(day)}$: concrete modulus of elasticity at different age (days)

E^*_e: effective concrete modulus of elasticity, E^*_e: $\frac{E_{c(3)}}{1+\phi^*}$

E_{GFRP}: GFRP bar modulus of elasticity (GPa)

E_s: steel modulus of elasticity (GPa)

$f'_{c\,(day)}$: concrete compressive strength at different age (days)

f'_{co}: starting point of the non-linear curve (MPa)

f'_{cu}: concrete cube strength (MPa)

$f_{cm28(ACI\ 318\text{-}11a)}$: concrete mean compressive strength(MPa)

$f'_{t\ (day)}$: concrete tensile strength at different age (days)

$f_{t\ (GFRP)}$: tensile strength of GFRP bars (MPa)

f_y: steel yield strength (MPa)

E_F: FRP modulus of elasticity (GPa)

GFRP: glass fiber reinforced polymer

G_f: concrete fracture energy (MN/m)

h: ambient relative humidity (%)

h: overall height of member (mm)

$K_{(h)}$: ambient relative humidity factor for Bazant model (%)

K_R: internal restraint factor

l: length parameter (m or mm)

L_c: element length scale parameter

m: number of cracks

N_{cr}: restraining force immediately after first cracking, $N_{cr}: \frac{n\ \rho f_t A_c}{C_1+n\rho(1+C_1)}$

$N_{(\infty)}$: final tensile force (KN)

n: $\frac{E_s}{E_{c(3)}}$

n^*: $\frac{E_s}{E_e^*}$

RC: reinforced concrete

S: average crack spacing (m), S: $\frac{L}{m}$

s_0: $\frac{1.33d_b}{10\rho}$

t: slab thickness (mm)

t(day): time (day)

t_c: concrete curing time (day)

T: ambient temperature (ºC)

v: volume of the submerged GFRP bars (ml.)

v/s: member's volume-to-surface ratio (mm)

w: final cracking width (mm)

w_d: end point of the softening curve (mm)

Δu*:* support displacement (mm)

$\beta_{(h)}$: ambient relative humidity factor for GL200 model (%)

$\beta_{RH(h)}$: ambient relative humidity factor for CEB-MC90 model (%)

$\beta_{as(t)}$: time development function of autogenous shrinkage

γ_{sh}: cumulative product of the applicable correction factors for fresh concrete properties and ambient humidity conditions (using *ACI 209.2R-08*)

ΔT: temperature change (ºC)

ε^*_{sh}: ultimate shrinkage strain (using *ACI 209.2R-08*)

$\varepsilon_{sh\infty}$: notional ultimate shrinkage for Bazant model (mm/mm)

ε_{shu}: notional ultimate shrinkage for GL 2000 model (mm/mm)

ε_{cso}: notional ultimate shrinkage for CEB-MC90 model (mm/mm)

$\varepsilon_{cdso(\,fcm28)}$: nominal drying shrinkage coefficient (mm/mm)

ε_{Total}: shrinkage strain of concrete subjected to different environmental conditions (mm/mm)

ε_c^p: value of plastic strain at the max compressive strength

ρ_{frp}: reinforcement ratio, A_{frp}/A_c

σ: concrete compressive stress (MPa)

σ_{av}: estimate of the average concrete stress in the period after first cracking, $\sigma_{av}: \frac{\sigma_{c1}+f_{t(7)}}{2}$

σ_{c1}: concrete stress away from the crack immediately after first cracking, $\sigma_{c1}: \frac{N_{cr}\,(1+C_1)}{A_c}$

σ^*_{c1}: final concrete stress away from the crack, $\sigma^*_{c1}: \frac{N_{(\infty)}-\sigma^*_{s1}A_s}{A_c}$

σ^*_{s2}: final bar stress at the crack, $\sigma^*_{s2}: \frac{N_{(\infty)}}{A_s}$

σ^*_{s1}: final bar stress away from the crack, $\sigma^*_{s1}: \frac{-2As_0m}{3L-2s_0m}\sigma^*_{s2} + \frac{3\Delta_u E_s}{3L-2s_0m}$

ϕ*: creep coefficient (using *ACI 209.2R-08)*

TABLE OF CONTENTS

LIST OF TABLES

LIST OF FIGURES

CHAPTER 1: INTRODUCTION

1.1 GENERAL

In field conditions, transportation structures such as bridge deck slabs and barrier walls will likely be subjected to temperature and humidity changes due to daily or seasonal conditions. Typically, while the concrete is still plastic during the first 24 hours after casting, thermal changes from hydration processes and environmental conditions increase the cracking tendency (Byard et al. 2010). After hardening, ambient temperature and humidity fluctuations affect the volume instability of concrete. Therefore, at early ages, these structural elements may be subjected to different combinations of shrinkage and swelling due to thermal cycles (e.g. heating-cooling, or freezing-thawing) and internal relative humidity fluctuation (e.g. wetting-drying). It is well-documented that the primary cause of early-age transverse cracking of bridge deck slabs is restraint to volumetric instability of concrete (Hadidi and Sadeghvaziri 2005; Mehta and Montherio 20014). There are many factors affecting this type of cracking such as materials properties, construction techniques, design practices, and environmental conditions.

Early-age cracking of concrete bridge deck slabs is a common problem in bridge construction all over the world. As bridge deck slabs are typically much longer in one direction than the other, volumetric changes due to shrinkage are more pronounced in the longitudinal direction. The girders, however, restrain the deck slabs against shrinkage which induces stresses that result in transverse cracks. The cracks, usually penetrating the full slab depth, are typically spaced 1.0 to 3.0 m apart along the span, and are commonly observed above the transverse reinforcing bars. Full-depth cracks are generally considered the most severe form of bridge deck slab cracking because they are additionally wide, which allows moisture and aggressive chemicals (e.g. de-

icing salts) to infiltrate into the concrete rapidly. As a result, transverse deck slab cracking can cause accelerated deterioration of reinforcing bars and concrete itself (Krauss and Rogalla 1996).

Recently, the non-corrodible fibre reinforced polymer (FRP) bars have been used as reinforcement for concrete members to mitigate the corrosion problem of conventional steel reinforcement. Among different types of FRP materials, the low cost of glass fibre reinforced polymer (GFRP) bars makes them more amenable for the construction industry. Compared to steel, GFRP bars have a lower modulus of elasticity, therefore, concrete elements reinforced with GFRP bars exhibit larger deformation which causes wider cracks. Unlike steel, GFRP materials do not corrode by nature; however, they may be susceptible to other forms of deterioration due to harsh environments such as de-icing chemicals, sulfates, UV and alkali (ISIS Canada 2006). This serviceability issue can be aggravated by harsh environmental conditions. A maximum crack width of 0.5 mm is recommended by the Canadian Highway Bridge Design Code-CHBDC, CAN/CSA-S6-06 (CSA 2006) for FRP-RC bridge components subjected to aggressive environments and 0.7 mm for other bridge members. Cracks are the easiest place for moisture and aggressive chemicals to accelerate the deterioration of GFRP bars as well as to shorten the service life of concrete structures. Design codes and previous studies proposed different models to calculate the maximum allowable crack width. These studies were based on cracks that are perpendicular to the main reinforcing bars as a result of flexural loading. Although reinforcement cannot stop cracking, placing longitudinal reinforcement can control both crack spacing and crack width in bridge deck slabs. Guidelines for designing bridge deck slabs typically specify a minimum amount of reinforcement to control cracks due to shrinkage or temperature changes. However, limited research has investigated the effect of longitudinal GFRP bars on the early-age transverse cracking of bridge deck slabs (Myers et al. 2003).

1.2 PROBLEM DEFINITION

Early-age cracking is one of the main problems facing concrete structures reinforced with GFRP bars, especially those having high surface-to-volume ratio such as bridge deck slabs, parking garage structures, concrete pavements, and industrial floors. These structures have high tendency to wide cracking, resulting from the restraint conditions, exposure to different environmental conditions and low modulus of elasticity of reinforcement.

Currently, there are several codes and guidelines providing recommendations for the design and construction of concrete structures reinforced with FRP materials, especially in USA and Canada. Most of these codes and guidelines are based on modifying corresponding formulas originally developed for steel bars and take into account the difference in properties and behaviour between FRP and steel material. For example, in the CHBDC (CAN/CSA-S6-06), the empirical design method for FRP-reinforced concrete (RC) cast-in-place bridge deck slabs provides 0.0035 for each layer as a minimum reinforcement ratio in the longitudinal direction. Moreover, based on an experimental study, Koenigsfeld and Myers (2003) concluded that the equation listed in ACI-440.1R-03 (ACI Committee 440 2003) [earlier version of ACI Committee 440 2006] for minimum FRP reinforcement ratio was overly conservative; however, they did not recommend any new equation to calculate minimum FRP reinforcement ratio. Although numerous studies have investigated the cracking and fracture behavior of RC elements, scarce data on restrained shrinkage cracking in FRP-RC elements have been reported under different environmental conditions. Consequently, further research is still needed in this area. The current study presents a research program evaluating the effect of longitudinal (secondary) GFRP reinforcement ratio and configuration on early-age cracking of bridge deck slabs subjected to

different environmental conditions such as adiabatic laboratory conditions as well as freezing-thawing and wetting-drying cycles.

1.3 SCOPE OF RESEARCH

This research is mainly investigating the contribution of the longitudinal reinforcement in controlling early-age cracking in FRP-RC structures. The scope of this program is to study cast-in-place bridge deck slabs reinforced with sand-coated GFRP bars. Normal strength concrete mix with silica fume admixture is used to represent the ultimate practical shrinkage strain. Only direct tension induced as a result of restraint and volumetric changes of concrete is considered; while, actions in the form of flexural loading causing flexural cracks are not included in the scope of this study.

1.4 RESEARCH OBJECTIVES

This research is among the early studies investigating the effect of longitudinal (secondary) GFRP reinforcement ratio on the early-age cracking of bridge deck slabs. Although many researchers have examined the flexural cracking of reinforced concrete structures, very few researches on restrained shrinkage cracking in reinforced concrete elements have been investigated. Even fewer to no research has addressed the shrinkage cracking in concrete elements reinforced with FRP under different environments, particularly for bridge deck slabs; therefore, further research in this area is urgently needed.

The main objective of this research is to develop a suitable design methodology for determining the minimum FRP reinforcement in bridge deck slabs to resist early-age cracking (with normal strength concrete) under different environmental conditions, such as wetting-drying and freezing-thawing cycles.

In this context, the following specific objectives are identified:

- Better understanding of the early-age behaviour of the GFRP-RC bridge deck slabs with experimental set-up simulating restrained field conditions.
- Investigating the applicability of currently available prediction/design models, design codes and construction practices.
- Investigating the effects of different ambient conditions such as freezing-thawing and wetting-drying cycles on early-age transverse cracking of GFRP-RC bridge deck slabs.
- Determining the minimum GFRP and CFRP reinforcement ratio for longitudinal bars in the top and bottom assembly.
- Investigating the effect of FRP bar spacing, bar surface texture, concrete cover and concrete strength on early-age transvers cracking of FRP-RC bridge deck slabs.

1.5 METHODOLOGY AND APPROACH

This research consists of two phases: an experimental investigation and an analytical study. The full-scale experimental study is performed to understand the restrained shrinkage cracking problem. A novel test set-up is introduced which allows for simulating the restrained shrinkage at early ages of bridge deck slabs.

The experimental phase includes two series. Series (I) consists of six full-scale specimens, which are constructed and tested in the laboratory to investigate the effect of reinforcement ratio under laboratory environmental conditions on early-age cracking in FRP-RC bridge deck slabs. These specimens have variable longitudinal reinforcement ratio (cross-sectional area of GFRP bars). Series (II) includes two specimens subjected to freezing-thawing and wetting-drying cycles. The objective of the second series was to investigate the effect of harsh environmental conditions on

the development of early-age cracking. The two specimens in this series are reinforced with the minimum-acceptable reinforcement ratio as obtained by first series. All specimens are properly instrumented to monitor strains, humidity, temperature history, and crack development. In addition, tests to obtain concrete properties such as tensile and compressive strength and modulus of elasticity are conducted. Also, to evaluate the internal conditions of the cementations matrix and the interconnectivity of the pore structure, in the concrete slabs subjected to different environmental conditions, materials tests are performed. These tests include the rapid chloride penetrability test (RCPT) and the dynamic modulus of elasticity (DME) from the ultrasonic pulse velocity (UPV).

The analytical phase of the research program consists of two stages. In the first stage, the computer software ATENA (ver. 5 2013) is utilized to construct a finite element model (FEM) for simulating restrained shrinkage bridge deck slabs. The most important parameters to consider in a computer simulation of RC bridge deck slabs subjected to restrained shrinkage are tensile fracturing of concrete and the effects of internal reinforcement to control the crack width. The constructed numerical models are verified against the results of the laboratory specimens. In the second stage, the verified model is used to investigate five key parameters known to affect early-age cracking; namely, reinforcement spacing, reinforcement type and bar surface texture, concrete compressive strength and thickness of concrete cover (top and bottom).

1.6 THESIS ORGANIZATION

This thesis consists of seven chapters. A brief description of each chapter is presented in the following paragraphs.

- Chapter one presents a general view of transverse early-age cracking in bridge deck slabs reinforced with GFRP bars and the problems associated with it. It identifies the need for further research that is required to improve the understanding of the early-age behaviour of the GFRP-RC bridge deck slabs with experimental test set-up simulating restrained field conditions, and describes the main objectives and scope of the Ph.D. research.
- A review of the characterization of GFRP reinforcement in concrete structures and parameters that influence the early-age volumetric instability and restraint degree in high surface-to-volume ratio structures are presented in Chapter two.
- Chapter three describes the test set-up, instrumentation, materials used, specimen details, and testing procedure. Also, the environmental schemes applied in this study scheme are presented in this chapter.
- The experimental results of Series (I) slabs subjected to shrinkage under normal laboratory conditions are presented in Chapter 4. The results are presented in terms of cracking pattern, crack width, strains in concrete and reinforcement in the vicinity of the main crack location.
- The test results of Series (II) specimens exposed to freezing-thawing and wetting-drying cycles are presented in Chapter 5. The results are presented in a similar manner to those of Chapter 4.
- All the necessary steps to construct the FEM including material types, boundary conditions, and the elements used in modeling along with verification of the model against the experimental data are explained in Chapter 6. Also, the effect of five key factors (concrete compressive strength, concrete cover, reinforcement surface texture,

spacing and type) on early-age cracking in FRP-RC bridge deck slabs subjected to shrinkage are presented in this chapter.

- Lastly, Chapter 7 presents a summary of the main findings and conclusions of the research study and recommendations for further research.

CHAPTER 2: LITERATURE REVIEW

2.1 GENERAL

In order to fully understand the transverse early-age cracking in bridge deck slabs, an extensive literature review was performed. The problem in concern is controlling shrinkage cracking width in concrete bridge deck slabs reinforced with GFRP bars. It should be noted that the research in this area, including steel-RC structures, is very limited due to the difficulty in simulating restrained conditions required to investigate shrinkage cracking problem in full-size specimens. Since there are many factors affecting early-age cracking, such as material properties, construction techniques, and design practices, part of the problem may arise from the fact that materials engineers consider it as a structural problem, and the structural engineers consider it as a material issue. Even when it is treated, both aspects are not usually considered. Although in this study we are focusing upon the structural aspect, material aspects will be also considered to fully understand the problem.

2.2 FRP COMPOSITE MATERIALS

2.2.1 Constituent Materials

The FRP products are composed of reinforcing fibres embedded in a matrix (resin) with some additives and fillers. The high strength fibres exhibit ideal elastic behaviour providing strength responsible for carrying the load (Fig. 2.1). The cohesive resin keeps the fibres together and provides lateral support for them against buckling. Also, the resin can protect the fibres from environmental and mechanical damage.

The mechanical properties of the FRP composite depend on different parameters such as fibres volumetric ratio, quality, shape, and orientation and resin type. Also, the manufacturing quality control is an important consideration to guarantee a high quality product.

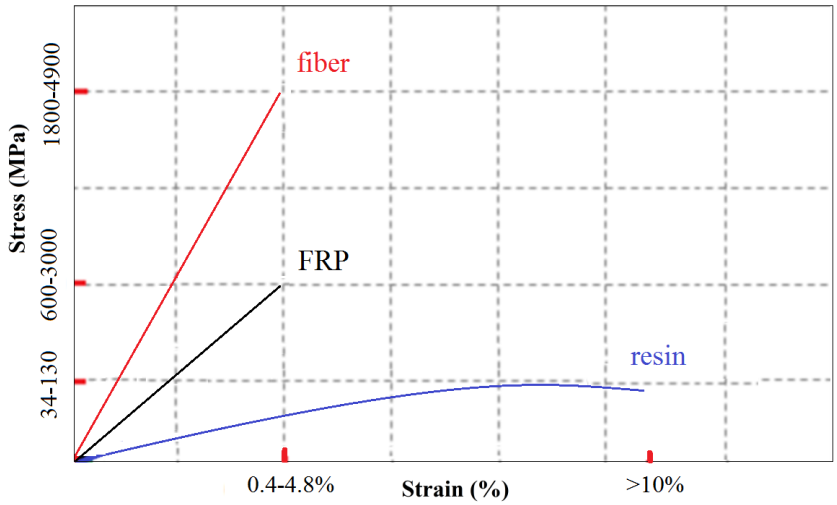

Fig. 2.1: Stress strain relationship for fibrous reinforcement and matrix (reproduced from ISIS manual No.3 2007).

Aramid, carbon, and glass are the mostly used fibres for FRP reinforcement products (ACI 1996). The aromatic polyamide fibre (AFRP) offers the highest tensile strength-to-weight ratio, impact resistance, and toughness in comparison with CFRP and GFRP fibres. Also they are resistant to carbon-based solvents, lubricants, and fuels. Aramid fibres are mainly used in aerospace and marine applications. The main disadvantages of AFRP products are their difficulty in cutting or machining and also low compressive strengths. The carbon fibres' precursors are one of the three types of pitch, rayon or polyacrylonitrile (PAN) fibres. The high tensile modulus-to-weight ratio as well as tensile strength-to-weight ratio, and high fatigue strengths are the main advantageous of CFRP products. They are most commonly used in the aerospace industry. Nevertheless, the disadvantages of these composites are their low impact resistance, high cost and high electrical conductivity. Two forms of Glass fiber can be produced, continues

and staple fiber. Both forms are made by the same production method up to the fiber-drawing stage. Ingredients such as sand, limestone, and alumina are dry-mixed and melted in a refractory furnace. The temperature of the melt varies for each fiber-drawing furnace in the direct melt process, or flows into drawn into fibers. Most glass fibers are currently produced by the direct melt process. The advantages of glass fibres are lower cost (compared to other types), high tensile strength, excellent resistance to compact and very low conductivity for both thermal and magnetic. However higher density, weak stiffness, lower resistance to fatigue, sensitively to abrasion and corrosion to alkaline solutions, and absorption of moisture can be considered as disadvantages of glass fiber reinforced polymer.

The selection of appropriate resin plays an important role in the final mechanical properties and quality of the FRP composite. Thermosetting and thermoplastic are the two main types of polymeric matrices (resin) used for FRP products. Thermoplastic polymer are connected together by weak bonds that can be broken by pressure or heat, while thermosetting polymers form a solid matrix that once set, cannot be reformed again by neither pressure nor heat.

The use of additives and fillers in the FRP composites can perform number of additional advantages such as fire resistance, coloration, and viscosity control. Also they can improve the performance of the FRP products that might not be achieved by the other FRP components.

2.2.2 Physical Properties

Generally, the physical properties of the composite material are attributed to their coefficients of thermal expansion (CTE) and density features. Fibre reinforced polymers bars as heterogeneous materials have different CTE values in the transverse and longitudinal directions. Basically the coefficient of thermal expansion in the longitudinal direction is dominated by the fibre properties,

while the transverse coefficient is governed by the resin properties (ACI 2006). Typical CTE values for steel and different FRP composite bars are shown in Table 2.1.

2.2.3 Mechanical Properties

Figure 2.2 shows the typical linear-elastic performance of different FRP reinforcements along with steel bars up to failure. It should be noted that, none of the FRPs show ductile behaviour with typical yielding plateau as the steel bars do. However, they have higher tensile strength and lower modulus of elasticity than that of the conventional steel.

The mechanical properties of FRP bars rely on the volumetric ratio and type of fibres in the composite, type of resin, and manufacturing quality control. Table 2.2 shows the typical mechanical properties of available FRP reinforcing bars.

2.2.5 Design of Concrete Structure Using FRP

The design philosophy of the concrete structures using FRP reinforcement is different from that of conventional steel-reinforced concrete. This is referred to the following differences in their mechanical behaviour. The FRP are characterized by high tensile strength only in the direction of the longitudinal fibres (as anisotropic material). This anisotropic behaviour affects the dowel action and shear strength of FRP bars. Moreover, FRP materials do not show ductile behaviour with yielding plateau, they are elastic until failure, and consequently design procedures should account for a sudden failure in FRP-RC structures.

2.3 SHRINKAGE OF CONCRETE

Shrinkage is observed in both hardened and fresh states of concrete. The loss of water from the capillary or gel pores is the main cause of shrinkage from its fresh state to later in life. The loss of water from the capillaries or gel-pores results in internal relative humidity gradients in the

concrete. The empty capillaries attract water molecules from the surface of the calcium silicate hydrates; therefore, attraction force develops between calcium silicate hydrate particles. This attraction force causes the concrete mass to shrink (Newman and Choo 2003). According to the time of the appearance of the shrinkage, it can be classified in three main types; plastic, autogenous, and drying shrinkage that occurred approximately within 30 min. to 6 hours, 1-28 days, and 1 day to 1 year, respectively (Mehta and Monterio 2014). The risk of early-age cracking of concrete will be increased when the amount of early-age shrinkage of concrete exceeds 1000 μm/mm (0.001 in./in.) (Transportation Research Circular E-C107 2006).

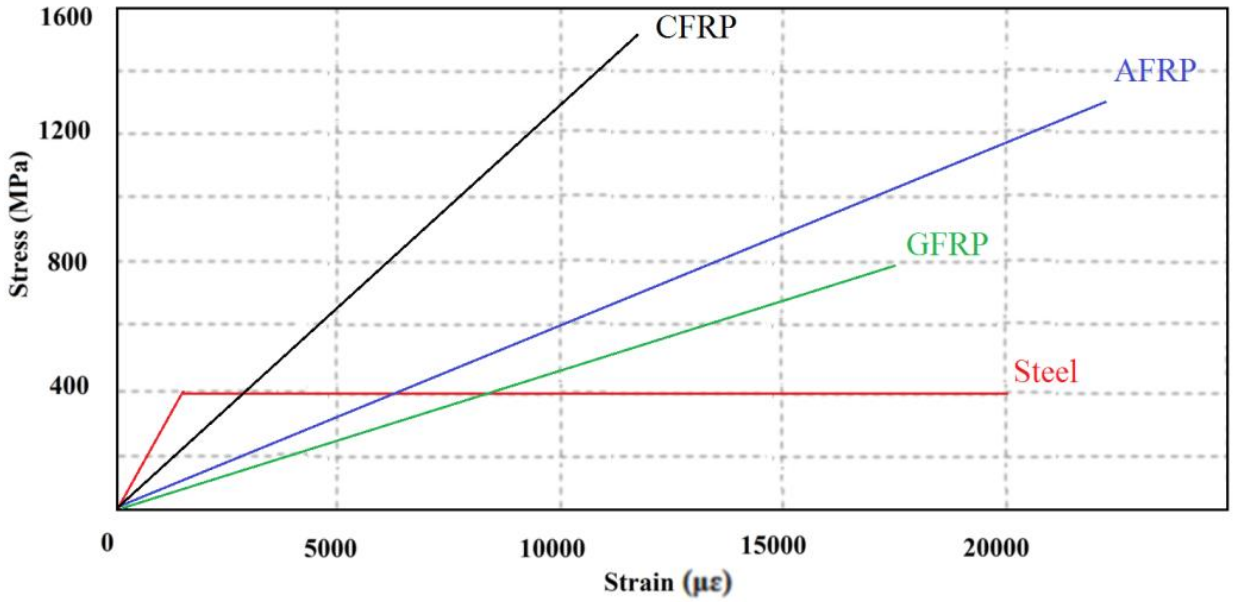

Fig. 2.2: Stress-strain curve for different reinforcing materials (reproduced from ISIS Manual No.3 2007).

Table 2.1: Typical coefficients of thermal expansion (Reproduced from ACI, 2006)

Direction	**Coefficient of Thermal Expansion ($\times 10^{-6}$/°C)**			
	CFRP	Steel	AFRP	GFRP
Longitudinal	-1 to 0	11.7	-6 to -2	6 to10
Transverse	22 to 23	11.7	60 to 80	21 to 23

Table 2.2: Typical mechanical properties of FRP reinforcing (reproduced from ISIS Canada, 2007 and Pultrall Inc. 2014)

FRP Type	**Trade Name**	**Modulus of Elasticity (GPa)**	**Tensile Strength (MPa)**	**Ultimate tensile Strain**
Glass Fibre	V-ROD™ (LM)	42	940	0.022
	V-ROD™ (HM)	63	1200	0.019
	Aslan™	41	690	0.017
	V-ROD™ (LM)	30	600	0.02
Carbon Fibre	V-ROD™	121	1597	0.014
	Aslan™	123	2069	0.018
	Leadline™	148	2251	0.016
	NEFMAC™	1000	1201	0.013

2.3.1 Plastic Shrinkage

The evaporation rate of fresh concrete surface water in excess of 1.0 kg/m^2 per hour is considered to be critical where surface dries and plastic shrinkage occurs. Fresh concrete surface water (due to bleeding) can be described as the upward movement of grout along with downward movement of the heavier suspended aggregates within fresh concrete (Mehta et al. 2014).

2.3.2 Drying Shrinkage

Concrete drying shrinkage can be described by three mechanisms: disjoining pressure, surface tension, and capillary stress. However capillary stress appears to be the major mechanism in the relative humidity range from 45% to 85%. During drying shrinkage the water evaporates from the capillary or gel pores in the hardened concrete, consequently the tensile stresses, confined to the surface tension of the water, are moved to the capillary pores resulting in the concrete contraction (Newman and Choo 2003).

2.3.3 Autogenous Shrinkage

The water is consumed during the hydration process of cement paste, which reduces the relative humidity of the concrete resulting in the autogenous shrinkage. This reduction of relative humidity results in increasing the surface tension in capillary water. Autogenous shrinkage occurs even if the concrete specimen is completely sealed from outer environment (TRB 2006). This is contrary to drying shrinkage that occurs due to moisture transfer between concrete and environment.

2.3.4 Carbonation Shrinkage

Cement paste reacts with carbon dioxide (CO_2) during the hardening process; this reaction increases the temperature (exothermal reaction) and weight of the concrete (Issa 1999). This phenomenon causes shrinkage in the concrete. Carbonation shrinkage occurs only at early-age of fresh concrete and it is not as significant as the other shrinkage types at early age.

2.3.5 Shrinkage Strain Prediction

ACI-209.2R 2008 offers different models such as ACI 209R-92 (Eq. 2.1), Bažant-Baweja B3 (Eq. 2.2), GL2000 (Eq. 2.3), and CEB MC90-99 (Eq. 2.4) to predict time dependent shrinkage of

concrete. These empirical based models are applicable for the concrete moist cured at least for one day. The shrinkage predicted methods were calibrated for the concrete containing silica fume and fly ash less than 30% and compressive strength within 20-80 MPa. According to the provided experimental data bank by Muller et al. 1999 for shrinkage, the Bažant-Baweja B3, GL2000, and CEB MC90-99 methods can predict closest shrinkage value, while the ACI 209R-92 model underestimates the concrete shrinkage.

$$\varepsilon_{sh(t)(ACI\ 209)} = -780\gamma_{sh} f_{(t)(ACI\ 209)} \times 10^{-6} \quad \textbf{[Eq. 2.1]}$$

$$\varepsilon_{sh(t)(B3)} = -\varepsilon_{sh\infty} k_{(h)} S_{(t)(B3)} \quad \textbf{[Eq. 2.2]}$$

$$\varepsilon_{sh(t)(GL2000)} = -\varepsilon_{shu} \beta_{(h)} \beta_{(t)(GL2000)} \quad \textbf{[Eq. 2.3]}$$

where: γ_{sh} is the correction factor, $f_{(t)(ACI\ 209)}$, $S_{(t)(B3)}$, and $\beta_{(t)(GL2000)}$ are the time functions for ACI 209, Bazant, and GL 2000 models, respectively. $\varepsilon_{sh\infty}$ and ε_{shu} are the nominal ultimate shrinkage for Bazant, and GL 2000 equations, respectively. $K_{(h)}$ and $\beta_{(h)}$ is environmental relative humidity factors for Bazant and GL 2000 models, respectively.

Among these models, CEB MC90-99 has been modified to take into account the particular characteristics of concrete strength (for high strength concrete). This approach consists of autogenous and drying shrinkage components. The total shrinkage of concrete can be calculated by Eq. 2.4.

$$\varepsilon_{sh(t,tc)} = \varepsilon_{caso}(f_{cm28})\beta_{as(t)} + \varepsilon_{cdso}(f_{cm28})\beta_{RH}(h)\beta_{ds(t)} \quad \textbf{[Eq. 2.4]}$$

where: $\varepsilon_{caso}(f_{cm28})$ is the nominal autogenous shrinkage coefficient, and $\beta_{as}(t)$ is the time function for autogenous shrinkage, $\varepsilon_{cdso}(f_{cm28})$ is the nominal drying shrinkage coefficient, $\beta_{RH}(h)$ is the environmental relative humidity, and $\beta_{ds(t)}$ is time function for drying shrinkage.

2.4 THERMAL CONTRACTION OF CONCRETE

Temperature changing can be associated with heat from an external (weather), and/or internal sources (heat of cement hydration). Internal heat is produced during the hydration reaction between cement and water (cement hydration is an exothermic process). The temperature rises during time and reaches the peak temperature after approximately 10 to 20 hours after casting. The peak temperature, which is derived as shown in the Eq. 2.5, depends on several factors such as the content cement type, the environmental conditions at casting time, the type of formwork, and the geometry of the member (Newman and Choo 2003). After reaching peak temperature, the concrete starts to cool and reduce the volume.

Heat generated from hydration of 1 kg cement is about (Table 2.3):

$$H = 0.108 \times 867 + 0.541 \times 502 + 0.166 \times 260 + 0.091 \times 419 = 446 \text{ kJ/kg} \quad \textbf{[Eq. 2.5]}$$

Assuming the specific heat of concrete (energy) required to raise temperature of a material of unit mass by one degree for normal concrete: 1~1.5 kJ/kg·°C and for water: 1 Cal/kg·°C = 4.18 kJ/kg·°C is around 1.3 kJ/kg °C, the concrete cured in an adiabatic condition and cement content per cubic meter of concrete is 470 kg, density of the concrete 2400 kg/m3, and coefficient of thermal expansion (for concrete: gravel 12, granite 9, limestone 6, and Cement paste: 11 ~ 20) is 10-6/°C:

The temperature increased due to hydration heat is

$$T = \frac{(446kJ/kg) \times 420kg/m^3}{2400kg/m^3 \times 1.3kJ/kg \cdot °C} = 60°C \quad \textbf{[Eq. 2.6]}$$

In the real situation, no matter how big is the concrete pour, concrete is not in adiabatic condition, so temperature rise due to cement hydration is always lower than the derived value from the compound hydration heat assuming adiabatic condition. It would be a rough guess that 470 kg per cubic meter of concrete would raise the temperature inside large concrete pour by around 60°C. The strain due to thermal gradient in concrete can be determined by Eq. 2.7 given in ACI 209.2R 2008.

$$\varepsilon = (C_{th})(dt)(K_R) \quad \textbf{[Eq. 2.7]}$$

Where:

ε: Induced tensile strain ($\times 10^{-6}$), C_{th}: coefficient of thermal expansion ($\times 10^{-6}$/°C), dt: temperature difference with respect to interior temperature (°C), and K_R: internal restraint factor.

Assuming the concrete coefficient of thermal expansion: C_{th} = 19 × 10^{-6}/°C, temperature difference with respect to interior temperature (°C): dt = (60-20) °C, and internal restraint factor: $K_R = 1$

The induced concrete strain due to the hydration temperature gradient is:

$$\varepsilon = 19 \times 10^{-6} \times 40 \times 1 = 760\ \mu\varepsilon \quad \textbf{[Eq. 2.8]}$$

Table 2.3: Heat of hydration kJ/kg (Cal/kg) of typical cement components (Newman and Choo 2003)

Compound	**Typical content (%)**	**Heat of hydration kJ/kg (Cal/kg)**
C_3A	10.8	867 (207)
C_3S	54.1	502 (120)
C_2S	16.6	260 (62)
C_3AF	9.1	419 (100)
Minor Compound	-	

2.5 SHRINKAGE AND TEMPERATURE CRACKING OF RESTRAINED CONCRETE

If the volumetric change (specifically contraction) of concrete is restrained, tensile stresses will induce in the concrete. If the developed tensile stresses are higher than the concrete tensile strength, the concrete will crack (Fig. 2.3**)**. The restraint can be internal, from reinforcement and aggregate, or external, from the sub-base or superstructure of a bridge (Frosch et al. 2003). If strains are not uniform throughout a member, as though produced by a thermal gradient, the member itself can serve as a restraint. The magnitude of induced tensile stresses depends on both the degree of restraint (how much movement is restricted) and the amount of shrinkage.

Bridge deck slabs are typically much longer in one direction than the other, thus volumetric changes due to shrinkage and temperature changes are more pronounced in longitudinal direction. Composite bridge deck slabs are continuously restrained with the girders. Since the girders restrain the concrete bridge deck slabs against its volumetric instability (change), stresses are induced on the bridge deck slabs that result in transverse cracks (Fig. 2.4) (Hadidi and Sadeghvaziri 2005). Volumetric changes of concrete and degree of restraint against these changes are greatly influenced by several factors, which are mainly related to concrete materials,

concrete properties, structural design, construction practices and environmental conditions. These factors are discussed in the following sections.

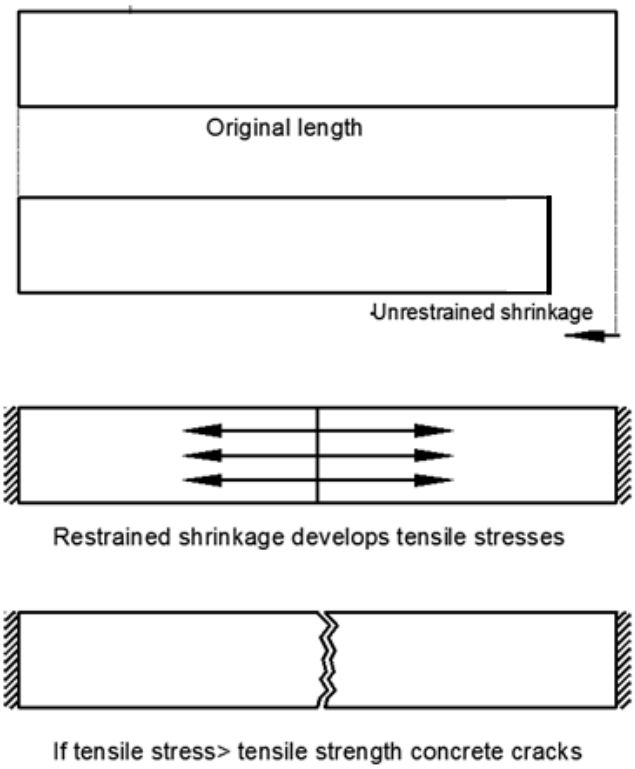

Fig. 2.3: Restrained shrinkage cracking (reproduced from ACI Committee 224 2001).

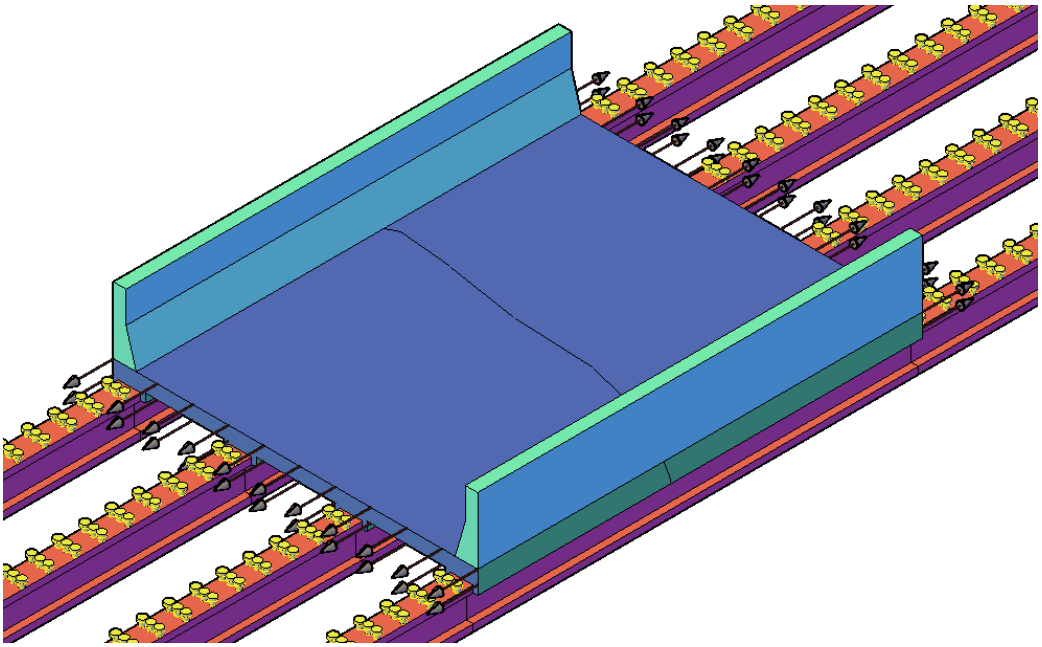

Fig. 2.4: Continuously restrained full length bridge deck slab (reproduced from Frosch et al. 2003).

2.6 FACTORS RELATED TO DESIGN

Influences of different design factors on transverse cracking of bridge deck slabs are mainly due to the restraint of volumetric instability of concrete. The effects of different design factors are described briefly in the following sections.

2.6.1 Longitudinal Reinforcement

Transverse cracking of concrete bridge deck slabs are commonly observed directly above the top reinforcing bars (Krauss and Rogalla 1996; Ramey et al. 1997). The effect of reinforcement on the cracking tendency of concrete is found in both phases (fresh and hardened) of concrete. The settlement of solids in the fresh concrete is hindered due to the presence of reinforcement consequently; tensile stresses are produced above the reinforcing bars which cause plastic settlement cracks (Fig. 2.5). Reinforcing bar size and spacing as well as clear concrete cover thickness affect the magnitude of differential settlement greatly. Larger plastic settlement cracks

develop for larger bar size and smaller cover thickness (Weyers et al. 1982; Dakhil et al. 1975). The volumetric contraction of hardened concrete due to shrinkage or thermal changes is restrained by reinforcement and produces tensile stress in the concrete. Reinforcing bar size, type, spacing, and alignment affect the cracking tendency of concrete bridge deck slabs. Larger bar size, and aligned transverse top and bottom bars create weakened cross-section of concrete deck slab which is more susceptible to cracking.

On the other hand, the reinforcement can limit the concrete crack widening when the shrinkage or thermal changes create tensile forces large enough to exceed the tensile strength of concrete. Though the tensile stress is developed due to the internal restraint of reinforcement, it is very small or negligible compared to external restraint such as restraint from composite girders and the continuity of concrete deck slabs in bridges. Reinforcement cannot stop cracking of a composite bridge deck slab but it can control the crack width.

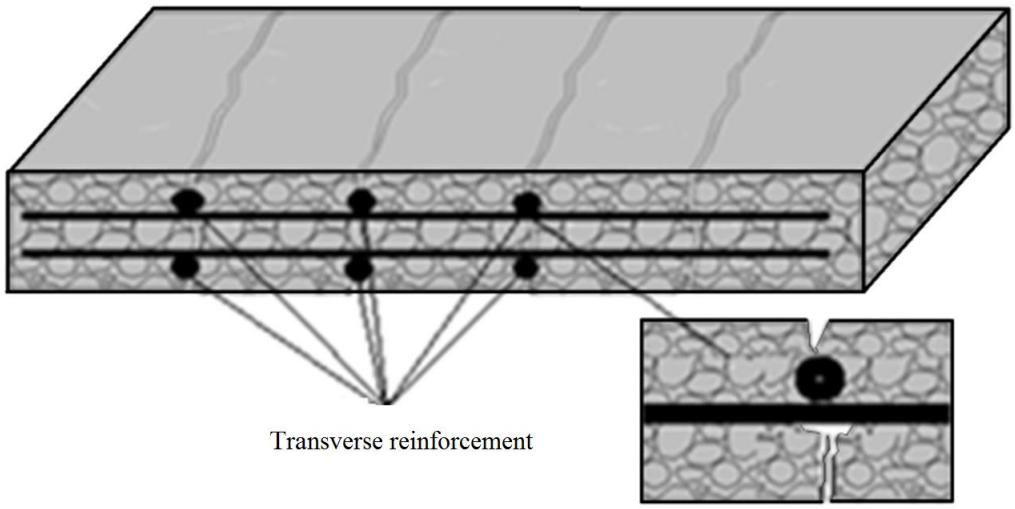

Fig. 2.5: Swelling and plastic settlement cracks.

Crack width depends on the bond between steel and concrete, reinforcement and concrete quantity, distribution and size of bars, and degree of restraint (Gilbert 1992). Finer crack widths

with uniform spacing can improve the serviceability and durability of bridge deck slabs. For durability issues, shrinkage and temperature reinforcement as a minimum reinforcement is mandatory in the most codes. Shrinkage and temperature reinforcement according to different codes are presented in Table 2.4.

The amount of shrinkage and temperature reinforcements are suggested in the codes to control cracking, however, problems related to early-age cracking still exist. Moreover, many researchers introduced recommendations related to shrinkage and temperature reinforcement to limit cracking, which can be summarized as follows:

- As longitudinal steel reinforcing bars control transverse cracking, at least size 10M (11.3 mm-diameter) bars should be placed at a maximum spacing of 150 mm (6 in.) (Krauss and Rogalla 1996).
- About 0.60% of gross concrete area (A_g) is required as minimum steel reinforcement (A_s) percentage to control cracks to a more acceptable level (ACI Committee 224 2001).
- For restrained shrinkage, about three times the amount of minimum steel reinforcement specified in ACI 318 code (Section 7.12) is required to control cracks (MacGregor and Wight 2005).
- For a fully-restrained slab, the shrinkage and temperature reinforcement should be two times of that required by ACI 318 code (Gilbert 1992).
- The total amount of longitudinal steel reinforcement to prevent uncontrolled crack growth from yielding of the reinforcement can be calculated according to the following equation (Frosch et al. 2003):

$$A_s = \frac{6\sqrt{f'_c}}{f_y} A_g \qquad \textbf{[Eq. 2.9]}$$

2.6.1.1 Code provisions

The minimum FRP reinforcement ratio for shrinkage and temperature recommended in ACI-440.1R-06 guidelines (ACI Committee 440 2006) has no experimental basis. It is noted that the ACI-440.1R-06 limited the upper range for the ratio of temperature and shrinkage reinforcement to 0.0036 (Table 2.4). Based on an experimental study, Koenigsfeld and Myers (2003) concluded that the equation listed in ACI-440.1R-03 (ACI Committee 440 2003) [same as in ACI Committee 440 2006] for minimum FRP reinforcement ratio was overly conservative; however, they did not recommend any new equation to calculate minimum FRP reinforcement ratio. Koenigsfeld and Myers (2003) found three times larger crack widths for GFRP specimens (1830 mm × 591 mm × 127 mm) than specimens of similar steel reinforcement ratio when subjected to restraint shrinkage. They also concluded that twice as much GFRP reinforcement as steel is required to achieve similar crack control characteristics when subjected to flexural loading. Due to lower stiffness of GFRP bars, lower internal tensile stresses in concrete will develop due to internal restraint from reinforcement against concrete shrinkage or temperature variations, which leads to larger crack spacing followed by wider crack widths (Chen and Choi 2002). Though the larger crack width is not a problem for FRP bars, maximum crack width must be limited due to aesthetic reasons, aggressiveness of the environment, and anticipated service life of the structure (ISIS Canada 2007). A maximum crack width of 0.5 mm is recommended by CHBDC (CSA 2006) for FRP-reinforced concrete components subjected to aggressive environment and 0.7 mm for other members.

2.6.2 Concrete Cover

Concrete cover is essential to protect the reinforcement from aggressive environments and to provide sufficient bond between reinforcing bars and concrete. All design codes for RC

structures suggest minimum concrete cover depending on the exposure conditions of the structure. Literature review indicates that concrete cover has an inconsistent influence on crack development in bridge deck slab. Increased cover thickness reduces the tendency of cracking (Ramey et al. 1997); however, concrete deck slabs with more than a 75-mm (3 in.) thick cover are more susceptible to cracking (Myers 1982). Gilbert (1992) concluded that under direct tension (due to shrinkage or thermal changes) cracks are more parallel-sided, which is different from flexural cracks hence the magnitude of the crack width is less dependent on the concrete cover.

2.6.3 Thickness of Concrete Deck Slab

Literature review indicates that thinner deck slabs are more susceptible to cracking than thicker ones (Myers 1982; Ramey et al. 1997; French et al. 1999; Hadidi and Saadeghvaziri 2005). Different minimum deck slab thicknesses were proposed to reduce deck slab cracking. Krauss and Rogalla (1996) suggested a minimum of 200 to 300 mm (8 to 9 in.) thick deck slab; French et al. (1999) recommended deck slab thickness not less than 160 mm (6 ¼ in.); Myers (1982) observed that deck slabs thicker than 250 mm (10 in.) are less susceptible to cracking. On the other hand, the deck slab itself can serve as a restraint if uniform shrinkage or temperature changes are not developed throughout the deck slab. As shrinkage and temperature changes are more uniform in thinner deck slabs than thicker one; thicker deck slabs may experience increased stresses (Krauss and Rogalla 1996).

2.6.4 Stiffness of Bridge Girders

Several researchers suggested that lower section stiffness decreases the tendency of deck slab cracking as the restraint of volume change of the deck slab is the main reason for deck cracking (Krauss and Rogalla 1996; French et al. 1999; Ducret et al. 1997). Using finite-element models,

Hadidi and Saadeghvaziri (2005) studied numerically the effect of section stiffness through changing the moment of inertia of the composite section and found that the potential for the deck slab cracking increased with the increase of composite section moment of inertia.

2.6.5 Type and Spacing of Girders and End Support Condition

Deck slabs compositely supported on steel girders (Fig. 2.6) have more cracking than those supported on concrete girders (Krauss and Rogalla 1996; Frosch et al. 2003). It may be due to the different coefficient of thermal expansion and higher thermal conductivity of steel girders compared to those of concrete girders. Cracking is more prevalent on spans with fixed-ended girders when compared to spans with pinned girders (Krauss and Rogalla 1996; French et al. 1999). Increased fixity (for example, bridge decks integrally built with abutment) increases crack density near the supported end (Darwin et al. 2004).

Composite bridge deck slabs are more economic in comparison with the isolated deck slabs (deck slabs just resting on girders). In order to get the benefits of arch action, the girder must be connected to the concrete slab to transfer of longitudinal shear forces at the girder top flange-concrete slab interface. When steel girders are used, the adequate connection is provided by installing shear studs to the top flange of the steel girder. Furthermore, composite bridge deck slab enhances the flexural capacity of the bridge deck slabs by providing internal arching actions between the girders. Transverse cracking in bridge deck slabs are mainly due to this type of high amount of external restraint. So, transverse cracking would be decreased with the decreasing of this external restraint (Krauss and Rogalla 1996; French et al. 1999; Saadeghvaziri and Hadidi 2005). As deeper girders with closer spacing (stiffer girders) make deck slabs more susceptible to cracking, shallower girders with wider spacing are recommended to control deck slab cracking (Krauss and Rogalla 1996; Saadeghvaziri and Hadidi 2005).

Table 2.4: Code provisions for temperature & shrinkage FRP reinforcement

Code [Clause]	**Rebar Type**	**Area and/or Ratio**	**Formula**	**Spacing**	**Comments from codes**
ACI 440.1R-06 [Chapter 10]	FRP	A_{frp}/d	$= 0.0018 \times (414/f_{fu}) \times (E_s/E_f)$ ≤ 0.0036	$\leq 3h$ $\leq 300\ mm$	No experimental data are available for the minimum FRP reinforcement ratio for shrinkage and temperature.
CHBDC (CSA 2006) [16.8.8.1]	GFRP	A_{frp}/d	≤ 0.0035 (based on empirical method for the longitudinal bars in the bottom assembly and the transverse and longitudinal bars in the top assembly)	$\leq 300\ mm$	
CSA/S806-12 [8.4.2.3]	FRP	A_{frp}	$= (400/E_F)A_g > 0.0025A_g\ mm^2$ (in each of the two orthogonal direction)	$\leq 3h$ $\leq 300\ mm$	

E_s: Steel modulus of elasticity (GPa), E_F: FRP modulus of elasticity (GPa), A_{frp}: FRP bar area (mm^2), d: effective depth (mm), f_{fu}: design tensile strength of FRP (MPa), h: overall height of member (mm), A_g: overall gross section area of member (mm^2).

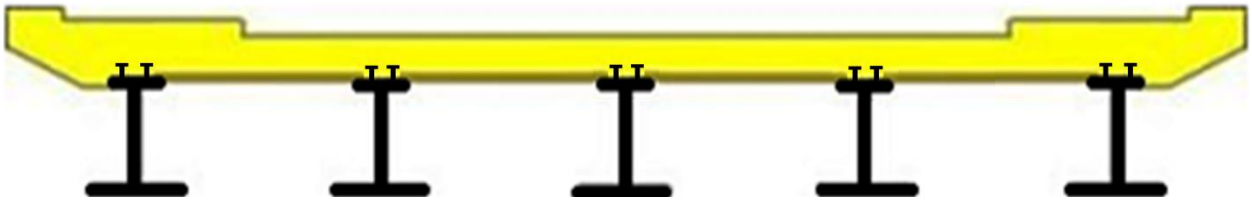

Fig. 2.6: Typical composite bridge decks.

2.7 FACTORS RELATED TO CONCRETE MATERIALS

Concrete is composed of cement paste and aggregates where cement paste acts as matrix and aggregates act as rigid inclusion. The amount of shrinkage and heat of hydration are fully dependent on the material properties of concrete and the ratio of constituent materials used in concrete mixture. The following section describes the effects of different concrete constituent materials on bridge deck slabs cracking.

2.7.1 Cement Type

The use of Type II cement is recommended in lieu of Type I cement by several researchers to reduce the cracking tendency of concrete deck slab (Krauss and Rogalla 1996; Xi et al. 2003; Hadidi and Saadeghvaziri 2005; Ramey et al. 1997). Type II cement has low heat of hydration and thus lower thermal gradient and shrinkage. To fulfill the requirement of high early strength to speed up form removal and access to the deck, fineness and composition of cement have been changed during the last 20 to 30 years. The cement has become progressively finer. Higher heat of hydration and greater shrinkage are the result of finer cement (Chariton and Weiss 2002; Darwin et al. 2004). Type K shrinkage-compensating cement (ASTM C-845 1996) is another type of cement that has been used to reduce early age cracking tendency in the bridge deck slabs (Krauss and Rogalla 1996).

2.7.2 Cement Content

The use of low amount of cement in concrete mix is recommended by many researchers as higher cement content produce higher temperature during hydration, shrinkage, and early-age modulus of elasticity, and low creep (Krauss and Rogalla 1996; Xi et al. 2003). All of these properties of concrete produced from the use of high content of cement have the marked adverse effect on cracking tendency of concrete bridge deck slabs. Maximum amount of cement content

has been recommended in different studies. French et al. (1999) and Hadidi and Saadeghvaziri (2005) recommended minimizing the cement content to 386-392 kg/m^3, while Xi et al. (2003) recommended limiting the cement content to a maximum of 279 kg/m^3 or less if possible.

2.7.3 Water Content

As the increase of water content increases the cracking tendency of concrete, reduction of water content is recommended in many studies (Issa 1999; Darwin et al. 2004; NCHRP 2004). However, Krauss and Rogalla (1996) found no correlation between cracking and water content in the concrete deck slabs.

2.7.4 Water-to-Cement Ratio

Water-cement ratio has a very strong influence on the shrinkage of concrete and cement paste. It is certain that high water-cement ratio leads to high shrinkage. Several studies recommended reduction in the water-cement ratio in the concrete mix to reduce the cracking tendency of concrete (French et al. 1999; Ramey et al. 1997; Xi et al. 2003). Maximum water-cement ratio has been recommended in different studies, which ranges from 0.40 to 0.45. Some studies also encouraged using water reducer to maintain water-cement ratio at 0.40 or lower. On the other hand, resistivity against early-age cracking is questioned for using low water-cement ratio as it results in high autogenous and plastic shrinkage, and less creep. High amount of shrinkage was observed before initial set for low water-to-cement ratio; and after little expansion between initial set and final set, shrinkage was continued after final set even under sealed condition (Fig. 2.7).

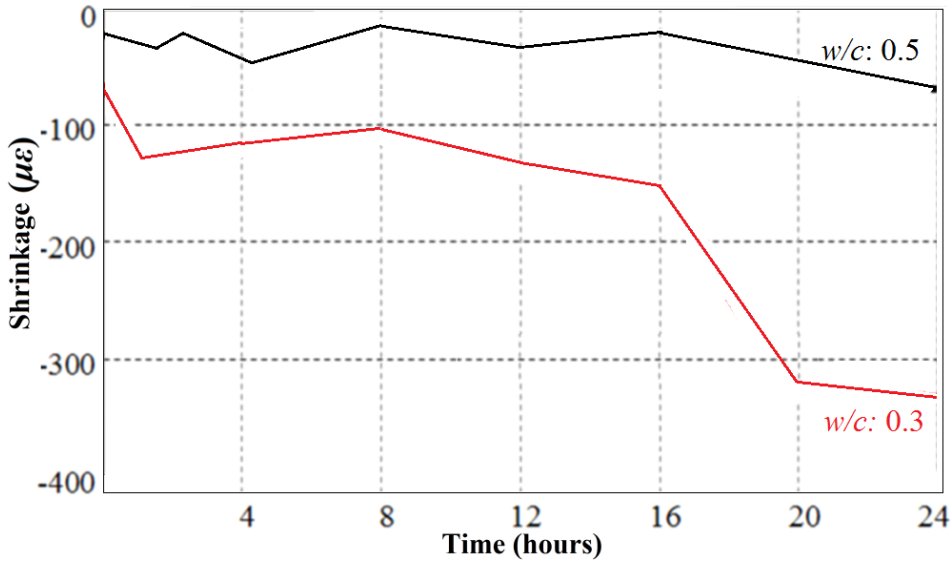

Fig. 2.7: Early-age shrinkage for different water-cement ratios in a mortar with 45% aggregate (reproduced from Pease et al. 2005).

2.7.6 Air Content

French et al. (1999) suggested air entrainment of minimum 5.5 to 6 percent to reduce cracking. Air entrainment is usually used to protect cracking due to freeze-thaw cycles by encapsulating tiny air bubbles in the hardened concrete. Water freezing in the capillary pores leads to 9% increase in volume. The resultant expansive force causes disruption of the pores if there is no room for the ice to expand into. With sufficient air bubbles within the capillary network, the ice can expand without causing disruption of the capillaries and thus prevents cracking. Again, the addition of air entrainment will produce a more workable concrete for the same water-cement ratio and thus less water (low water-cement ratio) can be used to get the desired level of workability. Decreasing the water-cement ratio of concrete is believed to reduce drying and plastic shrinkage and cracking tendency of concrete (French et al. 1999; Ramey et al. 1997).

2.7.7 Silica Fume

Silica fume (micro-silica) is a by-product of the production of silicon and ferrosilicon alloys in electric arc furnaces. The size of silica fume particles is approximately 100 times finer than normal Portland cement. During the hydration of cement, calcium hydroxide is produced. Micro-silica reacts with calcium hydroxide and produces calcium silicate hydrate (pozzolanic reaction). Calcium silicate hydrate fills pores and decreases the permeability of concrete. The spaces between cement grains are filled up by finer silica fume particles and also the spaces between cement paste and aggregates. The result benefits to increase the strength of the concrete. Higher heat of hydration is produced in silica fume concrete which causes higher thermal stress.

2.7.7.1 Effect of silica fume on plastic shrinkage and drying shrinkage

The loss of surface water (due to evaporation) cannot be readily replaced as the total amount and the rate of bleeding of the concrete are decreased due to the hindrance of fine silica fume particle. The result increases the shrinkage both in plastic and hardened concrete (Mehta et al. 2014).

2.7.7.2 Effect of silica fume on autogenous shrinkage

As the water chemically combined with the cement during hydration and specific volume of chemically bound water is lower than specific volume of free water, volume of hydrated cement paste is lower than the volume of cement and water (Powers and Brownyard 1947). This shortage of free water supply results in an overall shrinkage as the cement hydrates. In the normal concrete (where silica fume is not present), hydrated cement gel absorb the surrounding free water and expansion of gel structure reduce the effect of shrinkage. However, when silica fume is used with lower cement ratio, surrounding free water of concrete cannot enter into the very low permeable gel to swell (silica fume form finer cement gel which occupies lower

specific volume) and thus autogenous shrinkage is increased. The early-age cracking tendency of silica fume concretes is higher than conventional concrete (Krauss and Rogalla 1996; Darwin et al. 2004; Bloom and Bentur 1995). Whiting et al. (2000) found that the addition of silica fume has little effect on both early-age and long-term shrinkage cracking if the silica fume concrete is cured properly for at least seven days under moist condition. However, Whiting et al. (2000) concluded that, the concrete mixtures with silica fume produces higher shrinkage than those mixtures not containing micro-silica. Some studies suggested limiting the use of the amount of silica fume to achieve the optimum results.

2.7.8 Fly Ash

Fly ash, similar to micro-silica, is also a pozzolanic material. Micro-silica accelerates the rate of early-age strength gain and increases early concrete temperature, while fly ash retards the rate of early-age strength gain and reduces the early concrete temperature. Fly ash is found to reduce the calcium hydroxide content at 12 hours by delaying the formation of calcium hydroxide and pozzolanic reaction can begin after 3 days (Weng et al. 1997). It is also found that reactivity of calcium hydroxide with micro-silica is decreased when silica fume is used combined with fly ash. Class C fly ash had smaller drying and autogenous shrinkage than the general used cement paste mixture (Tangtermsirikul and Sudsangiam 1995). Brown et al. (2007) found that the use of high volume of fly ash (55% of the Portland cement was replaced with Class F fly ash) in concrete mixture had the best resistance to drying shrinkage cracking in concrete bridge deck slabs. However, Mokarem et al. (2003) showed that the mixture containing fly ash exhibits greater drying shrinkage compared to general used Portland cement mixture. Also Li et al. (1999) showed that the width of early-age crack increases with increasing fly ash, micro-silica, and calcium nitrate inhibitor.

2.7.9 Fibre-Reinforced Concrete

The application of small fibres (steel, glass, polyvinyl alcohol, cellulose and polypropylene) in concrete can reduce the shrinkage and thermal crack width. The distributed small fibres in the concrete change the large discrete cracks into finer cracks along with improving the post-peak ductility and increasing the concrete tensile strength (Hadidi and saadeghvaziri 2005).

2.7.10 Shrinkage Reducing Admixture

The main function of shrinkage reducing admixtures (SRA) is to reduce the drying shrinkage by reducing the surface tension of the water in the capillary pores. If the surface tension of the water is reduced, there is less tension transferred to the capillary walls, and consequently less shrinkage. Weiss et al. (1998) found that the use of SRA in concrete mixture will prevent or delay of cracking. Up to 45% reduction in free shrinkage was found after adding 2% SRA in concrete mixture.

2.7.11 Aggregate Size

Largest possible size of a high quality, low shrinkage aggregate is suggested in several studies to minimize the shrinkage of concrete. Maximum possible aggregate content that is high aggregate to binder ratio is also recommended. The shrinkage of aggregates is very low (almost negligible) compared to binder, which implies that the use high aggregate to binder ratio will reduce the total amount of shrinkage of concrete. Also larger aggregate size is recommended to minimize concrete shrinkage. They produce a rigid framework with the help of cement paste, consequently, movement of aggregate is reduced as the shrinkage of cement paste cannot pull the surrounding large aggregates closer (TBR 2006). Only micro cracks will be developed in cement paste surrounding the aggregates. The water demand of the aggregate has also a major influence on the shrinkage of concrete. ACI Committee 224 (2001) suggested aggregates with low

absorption and high modulus of elasticity will provide a low shrinkage concrete. Lopez et al. (2008) showed high performance concrete with pre-wetted expanded slate light weight aggregate produces lower shrinkage and total creep than air-dried expanded slate light weight aggregate. Lopez also concluded that compressive strength (56-day and 1-year) of pre-wetted expanded slate light weight aggregate was higher than that of air-dried expanded slate light weight aggregate due to the improved hydration afforded by the pre-wetted lightweight aggregate.

2.7.12 Concrete Properties

The properties of concrete are the reflection of mix design of concrete. Different concrete properties such as creep, modulus of elasticity, compressive strength, and thermal expansion of concrete have pronounced effect on bridge deck slabs cracking. Summary of the effect of different concrete properties are given below:

2.7.13 Creep of Concrete

Creep has beneficial effects in reducing the restrained drying shrinkage. Tensile stress is developed in the concrete from restrained drying shrinkage and thermal contraction. Creep leads the concrete to flow in small amounts and can serve to relax shrinkage tensile stresses and thereby, reduces the risk of cracking as shown in Fig. 2.8 (Brown et al. 2007). Therefore, higher creep means lowering the cracking tendency.

2.7.14 Modulus of Elasticity of Concrete

Restrained shrinkage and temperature changes induce tensile stress in concrete which are proportional to the modulus of elasticity of concrete. This means higher stress will develop for higher modulus of elasticity, and thus, cracking tendency of concrete will increase (Hadidi and Saadeghvaziri 2005).

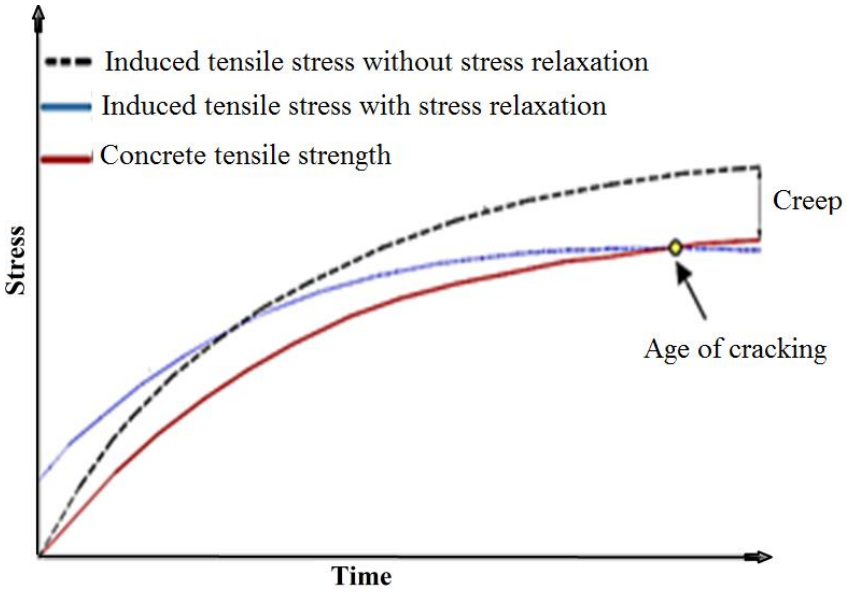

Fig. 2.8: Delayed cracking tendency from creep relaxation (reproduced from Brown et al. 2007).

2.7.15 Concrete Strength

The application of high strength concrete (HSC) has been increased during the past decades. In general, HSC is accompanied by an increase in the cement content and a decrease in the water-to-binder ratio, which results in an increment of hydration temperature and autogenous shrinkage. Therefore, compared to normal strength concrete, RC structures with HSC are more susceptible to early-age cracking. The HSC offers high sectional stiffness (Sooriyaarachchi 2005); thus structures made of HSC experience high tensile stress, and consequently, high cracking potential for the same amount of shrinkage (Hadidi and Saadeghvaziri 2005). However, due to the higher tensile strength of HSC, it also provides higher resistance to shrinkage and thermal cracking. Hence, it is a challenge to maintain a proper balance between concrete strength, shrinkage and other long-term properties (e.g. creep). Several studies investigated the effect of high strength concrete on early-age cracking in bridge deck slabs. Darwin et al. (2004) found that high compressive strength of concrete increased crack density for monolithic bridge decks. Petrou et al. (2001) concluded that more appropriate high performance concrete (HPC) mix design (for

enhanced durability characteristics not high-strength) is needed to be used in bridge deck slabs. Weiss et al. (1998) recommended the use of a shrinkage reducing admixture (SRA) in HSC to reduce the early-age cracking tendency in the structures with high surface-to-volume ratios.

2.7.16 Coefficient of Thermal Expansion

As the stresses developed in the deck slabs from a temperature change are linearly depend on the concrete coefficient of thermal expansion (CTE), consequently, transverse thermal cracking can be reduced by using lower CTE of concrete (Krauss and Rogalla 1996). They also suggested using less thermally expansive concrete and increasing aggregate content by reducing more thermally expansive cement paste content.

It should be noted that, GFRP bars are used mostly as internal reinforcement in lieu of steel reinforcement to overcome the corrosion problem. GFRP bars are also composite materials consist of continuous glass fibres in a polymer matrix (resin). Radial CTE of GFRP is higher than the longitudinal CTE of GFRP as the radial CTE depends on resin and longitudinal CTE depends on fibres. The coefficient of thermal expansion of GFRP is different from CTE of concrete which may lead to thermal restraint stresses when subjected to temperature changes.

Especially radial CTE of GFRP may cause to such stress field in the surrounding concrete that may lead to cracks along the bars in the concrete cover and consequently to bond failure (ISIS Canada 2007).

2.8 FACTORS RELATED TO ENVIRONMENT

Bridge deck slabs are usually exposed to harsh environments such as freezing-thawing cycles, temperature fluctuations and wetting-drying cycles within temperature and humidity ranges from –40°C to +35°C and 30 to 100 %, respectively (Laoubi et al. 2006). Therefore, at early-ages,

these structural elements may be subjected to different combinations of shrinkage and swelling. Figure 2.9 shows the influence of three different curing environments on the magnitude of shrinkage. It is believed that cracking tendency of concrete will increase with decreasing relative humidity and increasing temperature and wind speed.

The effects of different environmental conditions on concrete cracking are discussed below. In RC structures, damage due to severe environmental conditions can take various forms such as reinforcement de-bonding, scaling, and micro cracking (Bishnoi 2004 and Alves et al. 2011). Other forms of damage include large-scale spalling and crumbling of concrete and material fatigue, resulting in loss of strength and stiffness.

2.8.1 Hot Weather

High temperature increases water demand for given workability and increased water content increases drying shrinkage and thus increases the tendency of concrete cracking. The evaporation rate of moisture from fresh concrete increases with increasing temperature and thus increases the tendency of plastic shrinkage cracking (Koenigsfeld and Myers 2003). If the concrete placement ambient temperature is higher, the hydration reaction reacts more rapidly and the rate of heat evolutions is increased. Therefore, peak temperature of concrete is increased and thus the tendency of concrete cracking increased as the concrete shrinks as it cools from the peak temperature. Allowable maximum temperature during placement of concrete was suggested in several studies. Krauss and Rogalla (1996) suggested maximum concrete placement temperature of 27 °C (80 °F) and concrete temperature of at least 5-10 °C (41-50 °F) cooler than ambient temperature. French et al. (1999) recommended placing concrete at maximum temperature of 32 °C (90 °F) and avoiding pouring concrete on days when temperature variation is greater than approximately 10°C (50 °F). Xi et al. (2003) suggested, to avoid casting deck slabs when air

temperature is higher than 27 °C (80 °F) and avoid large temperature variation during concrete placement. For reinforced concrete elements with thickness of section less than 30 mm, the allowable maximum temperature of the concrete as placed should be less than 35 °C (CSA A23.1-09 2009).

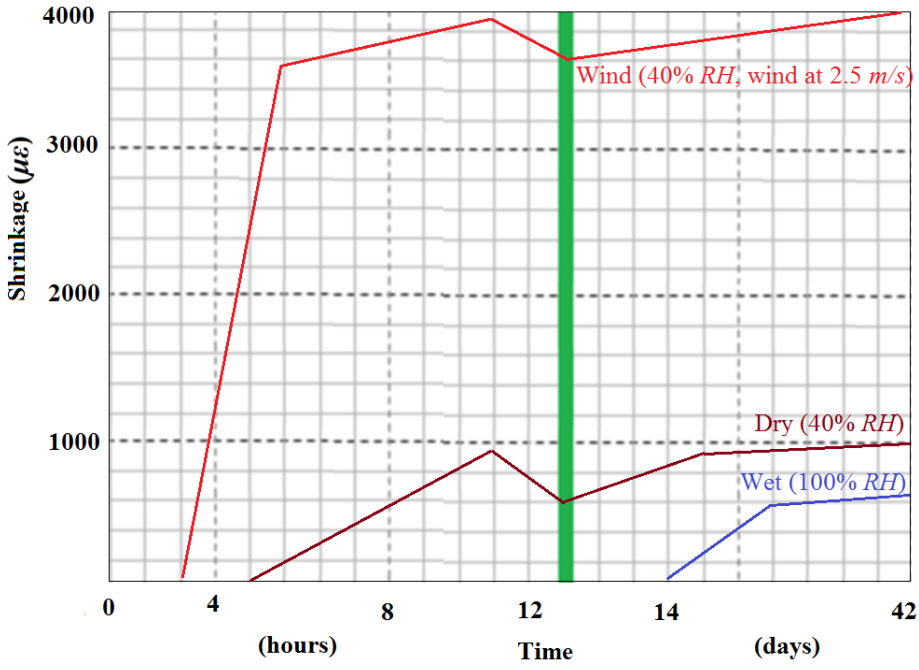

Fig. 2.9: The magnitude of shrinkage for Three Different Curing Environments (reproduced from Holt and Leivo 2000).

2.8.2 Cold Weather

Frost damage to fresh concrete and slow gain in strength is the main problems of cold weather concreting. Expansion of water (approximately below 4 °*C* water starts to expand) in fresh concrete may suffer permanent damage. Slower setting time may be the problem of concrete cracking as it allows greater evaporation while the concrete is plastic (Krauss and Rogalla 1996). Xi et al. (2003) recommended avoiding casting deck slabs when the temperature is lower than 7.2 °C (45 °F), and maintaining concrete mix temperature above 10 °C (50 °F) for the first 72 hrs and above 4 °C (40 °F) for the remaining curing period. French et al. (1999) suggested placing

concrete deck slabs only where the ambient air temperature is above approximately 4 to 7 °C (40 to 45 °F). For reinforced concrete elements with thickness of section less than 30 mm, the allowable minimum temperature of the concrete as placed should be more than 10 °C (CSA A23.1-09 2009).

2.8.3 Relative Humidity

Drying and plastic shrinkage are the cause of loss of water from concrete and the magnitude of water loss is due to the difference in relative humidity from the internal concrete to the external environment. The ultimate shrinkage and rate of shrinkage of concrete will increase with decreasing relative humidity as shown in Fig. 2.10 (ACI Committee 224 2001) and thus increasing the cracking tendency of concrete.

2.8.4 Effect of Wind

High wind speed increases the evaporation rate and consequently plastic shrinkage crack. The plastic shrinkage cracks occur when the rate of surface evaporation is higher than the bleeding rate. Xi et al. (2003) recommended avoiding concrete placement when the evaporation rate is above 1.0 kg/m2/hr. for normal concrete and 0.5 kg/m2/hr. for concrete with low water-cement ratio. The use of fogging equipment and windbreaks were suggested in NCHRP Synthesis of Highway Practice 333 (2004) to reduce the surface evaporation from fresh concrete. CSA (2014) Standard A23.1-14 also suggested taking special protection to avoid plastic shrinkage cracking when the rate of surface moisture evaporation exceeds 1.0 kg/m2/hr. Concrete mixtures with pozzolans are susceptible for early-age cracking if the rate of evaporation exceeds 0.5 kg/m2/hr. The rate of evaporation can be measured from Fig. 2.11 using measurements of air and concrete temperature, wind velocity, and relative humidity close to the surface of the concrete.

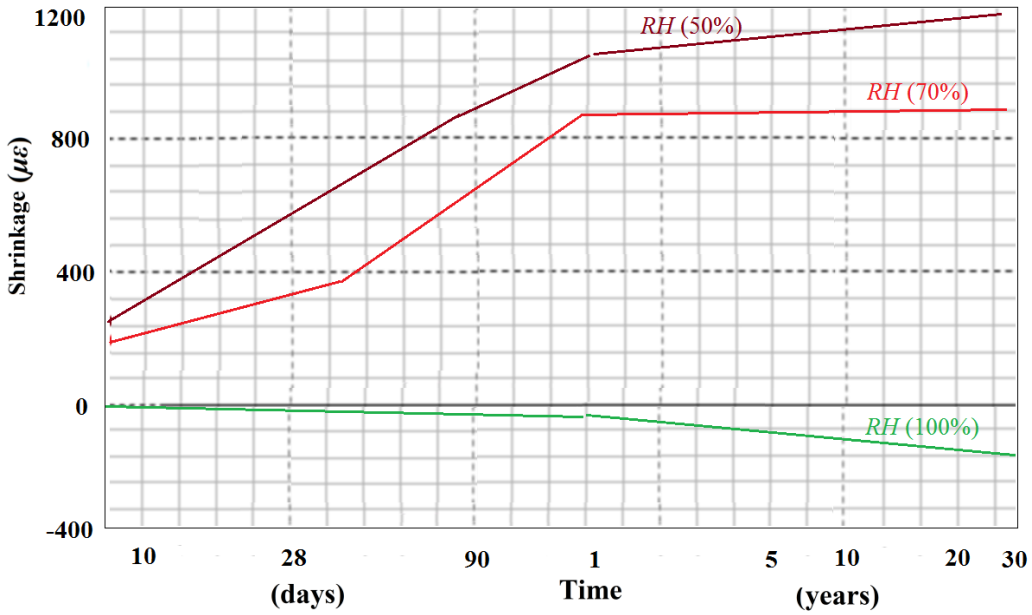

Fig. 2.10: Shrinkage vs. Time for Different Relative Humidity (reproduced from ACI Committee 224 2001).

2.8.5 Effect of Freeze-Thaw Conditions

Further deterioration can occur due to expansion of absorbed moisture in FRP and concrete under freeze-thaw cycling. In addition, freeze-thaw cycles can lead to degradation of the fiber-matrix bond and further damage the fibers through local notching due to ice formation on their surfaces (El-Badry et al. 2000). Temperature changes, due to difference in thermal properties between FRP bars and surrounding concrete, can result in further damage to FRP-RC structures. For example, GFRP can experience an expansion of 5-8 times greater than that of concrete in the transverse direction due to temperature variations. This thermal incompatibility can cause de-bonding of the bars from concrete under temperature changes (Gentry et al. 1999). Moreover, under freeze/thaw cycles, ice formation at the FRP-concrete interface leads to damage of FRP-concrete bond increasing existing crack width under sustained loads (Alves et al. 2011).

2.8.6 Effect of Wet-Dry Conditions

Among the actions that may lead to variations in moisture content in concrete, the wet/dry cycle is one of the aggressive environments suffered by concrete. Wetting-drying cycles are considered critical in the durability-based design of concrete structures since volume changes due to repetitive shrinkage/swelling may lead to material fatigue and de-bonding of reinforcement (Zhang et al. 2012, Ayano et al. 2002).

2.9 FACTORS RELATED TO CONSTRUCTION PRACTICE

Different types of construction techniques have a significant effect on the early-age cracking of concrete deck slabs. The effect of different construction practice factors are outlined below.

2.9.1 Curing

The water loss from concrete must be reduced to eliminate plastic shrinkage cracking and to reduce drying shrinkage cracking. Therefore, effective curing is mandatory immediately after proper finishing the surface of deck slabs. Almost all studies gave an emphasis on proper curing to avoid early-age deck slabs cracking. Whiting et al. (2000) and Xi et al. (2003) recommended a 7-day continuous moist curing for concrete contains silica fume and/or fly ash to reduce early-age cracking. After the 7-day wet curing period, application of curing compound was suggested in NCHRP (2004) to decelerate the shrinkage and to improve the concrete properties. Saadeghvaziri and Hadidi (2005) recommended the continuation of curing for a minimum of 7 consecutive calendar days immediately after finishing and to consider 14-day wet curing if "early-open" is not an issue.

2.9.2 Formwork

The effect of stay-in-place (SIP) forms on cracking appears inconsistent. Frosch et al. (2003) have shown that additional restraint from stay-in-place forms can increase early-age cracking tendency. However, Cheng and Johnson (1985) concluded that the use of SIP or timber forms have negligible effect on early-age cracking in bridge deck slabs.

2.10 CRACK WIDTH

Concrete can provide an excellent first line of defense to keep internal reinforcement intact. However, permeability and different types of cracking of concrete allow moisture and other corrosive elements into the internal reinforcement causing deterioration of bond, strength of internal reinforcement and strength of concrete itself (Gilbert 1992). Less permeable concrete is obviously more durable when evaluated from the material point of view; but it may not always be desirable or even essential to specify the lowest possible permeability for bridge deck slabs when the bridge deck slabs crack. The increase in the number of cracks reduces the benefits of the low permeability (high dens) concrete. As stated "We have managed to get excellent concrete between the cracks" (Concrete Cracking Workshop 2005).

Though reinforcement cannot stop the crack, it can control the crack width. The finer the crack width is the higher the durability. ACI Committee 224 (2001) limits the crack widths at the tensile face of steel reinforced concrete structures for different exposure condition Table 2.5.

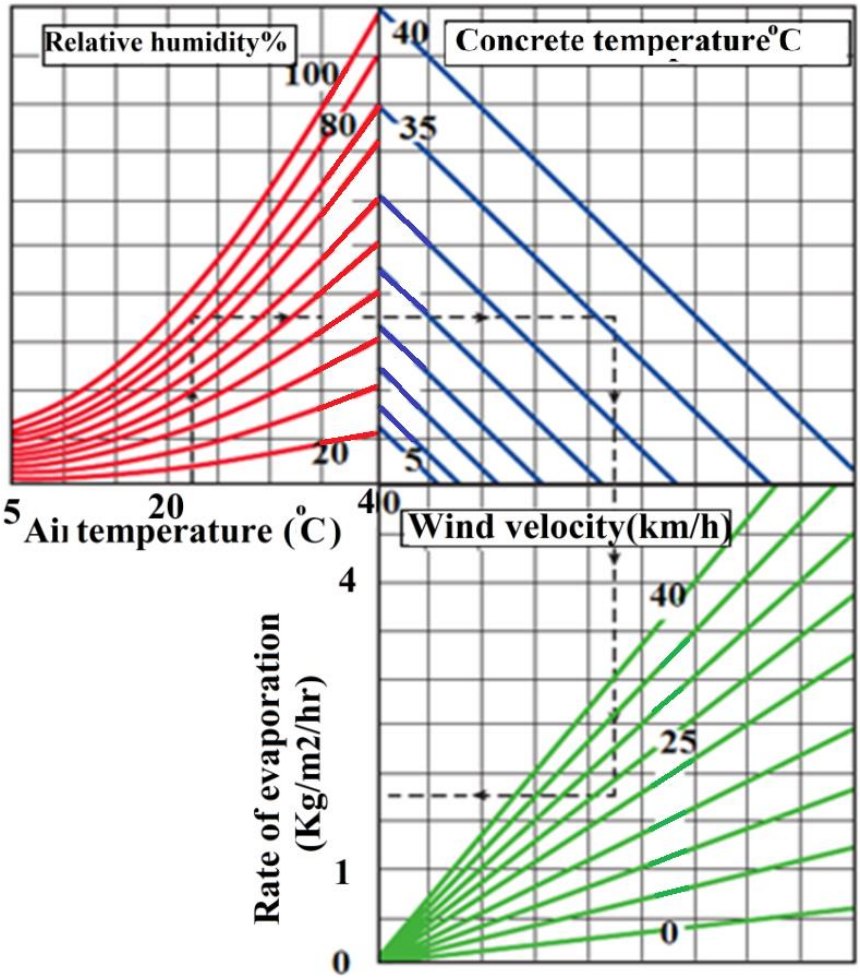

Fig. 2.11: The effect of concrete and air temperatures, relative humidity, and wind velocity on rate of evaporation of surface moisture from concrete (reproduce from CSA/A23.1-14 2014).

Table 2.5: Limits of crack widths for steel-reinforced structures (ACI Committee 224 2001)

Exposure Condition	Crack Width	
	in.	mm
Dry air or protective membrane	0.016	0.41
Humidity, moist air, soil	0.012	0.30
De-icing chemicals	0.007	0.18
Seawater and seawater spray; wetting and drying	0.006	0.15
Water retaining structures	0.004	0.010

As mentioned earlier, for lower stiffness of GFRP bars, lower internal tensile stress in concrete will develop due to internal restraint from internal reinforcement against concrete shrinkage or temperature variations and cause larger crack spacing followed by wider crack widths compared to that of same steel reinforcement ratio (Chen and Choi 2002). Koenigsfeld and Myers (2003) found three time larger crack widths for GFRP-RC specimens than specimens reinforced with similar steel reinforcement ratio when subjected to restraint shrinkage. They also concluded that twice as much GFRP reinforcement as steel is required to achieve similar crack control characteristics when subjected to flexural loading. Though FRP do not corrode like conventional steel re-bars, they are susceptible to deteriorate due to other degradation factors in potentially aggressive environments and conditions such as thermal actions, alkali, salt, freeze-thaw actions, ultraviolet rays; therefore, maximum crack width must be limited. Other than the aggressive environmental conditions acceptable crack width limits include aesthetics and shear effect. Canadian Standard Association (CSA 2006) limits the acceptable crack widths of 0.5 mm for exterior exposure and 0.7 mm for interior exposure. ACI Committee 440 (2006) also recommends using the crack width limitation of Canadian Standard Association (CSA 2006).

CHAPTER 3: EXPERIMENTAL PROGRAM

3.1 GENERAL

Based on literature, early-age cracking of concrete bridge deck slabs depends on various factors related to concrete materials, structural design, environmental condition, and construction practices. It is also found that transverse cracking in restrained bridge deck slabs is almost inevitable no matter what precautions taken to minimize shrinkage. Therefore, control of crack width and crack pattern is the main focus of this study by optimizing GFRP reinforcement ratio and configuration subjected to different environmental conditions. This chapter includes design, construction, and testing procedures of all eight test prototypes representing bridge deck slabs. These specimens are categorised in two series. Series (I) consists of six slabs subjected to normal laboratory conditions. Series (II) consists of two slabs subjected to freeze-thaw and wet-dry cycling one week after casting.

3.2 MATERIAL PROPERTIES

3.2.1 Concrete

Normal-strength, ready-mixed concrete incorporating 13% silica fume by mass of binder (Table 3.1) with a target 28-day compressive strength of 40 MPa was used to provoke high tendency of shrinkage as an extreme scenario that might be encountered in practice. The slump and fresh air content of this concrete were in the ranges of 100-120 mm and 6±1%, respectively. The US-Federal Highway Administration Guidelines [Silica fume user manual (Holland 2005)] reports on the use of 4 to 15% silica fume in concrete for various infrastructure applications.

3.2.2 Reinforcements

Two different types of longitudinal reinforcement, steel and GFRP, were used in this study. Sand-coated GFRP bars (Pultrall Inc. 2014) and deformed steel Grade 40 bars were used to reinforce the slab prototypes in both layers (top and bottom). The GFRP bars are made of continuous E-glass fibers with modified vinyl-ester resin with a fiber content of 75% by weigh (Pultrall Inc. 2014). The mechanical properties of the GFRP reinforcement were obtained according to the CSA S806-12 and ACI 440.3R-12 test specifications, while ASTM A370-14 standard method was used for the steel bars. The CSA/S806-12, Annex A (CSA 2012), provides a new test method for measuring the gross cross-sectional area of FRP reinforcement (including effective fibers and surface coating). According to the test specification, 8, 6, 3 and 1 specimen(s) with the same length of 290±0.5% mm were cut from the FRP bars No. 10, 13, 16 and 19, respectively. The average cross-sectional area of the bar equals to volume change divided by length for the submerged GFRP bar in the cylindrical transparent container (glass or plastic) (Eq. 3.1). The container has a dimension of 40 mm (internal diameter) and 300 mm (height).

$$A_{FRP} = \frac{v}{l} \times 1000 \qquad \textbf{[Eq. 3.1]}$$

where:

A_{FRP} is the bar cross-sectional area (mm^2), v is the volume of the submerged GFRP bars (ml.), and l is the GFRP bars length (290 mm).

The longitudinal and transverse coefficients of thermal expansion for the used GFRP bars are 6.2 and 23.8 [×10^{-6}/°C], respectively, while the longitudinal and transverse coefficients of thermal

expansion for the steel bars used are 11.7 [$\times 10^{-6}$/°C]. Table 3.2 summarizes the mechanical properties of the steel and GFRP bars used in this research.

Table 3.1: Proportions of concrete per cubic meter

Ingredient	**Amount/m^3**
Cement Type GU*	365 kg
Coarse aggregate (max. aggregate size, 20 mm)	1020 kg
Fine aggregate	650 kg
Air entraining agent	250 ml
Silica Fume	54.6 kg
Water	170 ml

*GU = General use.

Table 3.2: Mechanical properties of sand-coated GFRP and steel bars

Bar type	**Bar diameter (mm)**	**Bar area (mm^2)**		**Modulus of elasticity (GPa)**	**Tensile strength (MPa)**	**Tensile strain (%)**
		Nominal*	**CSA S806-12 Annex A**			
GFRP No.10	9.5	71	170	65	1572	2.4
GFRP No.13	12.7	127	197	65	1453	2.23
GFRP No.16	15.9	198	291	62	1450	2.33
GFRP No.19	19.1	285	394	63	1484	2.33
Steel No. 15M	16	200	NA	200	f_y^* = 420	ε_y^* = 0.21

*f_y: Steel yield strength, ε_y: Steel yield strain,

It should be noted that the nominal cross-sectional area of GFRP bars have been used to obtain the reinforcement ratio and the mechanical properties of the bars.

3.3 EXPERIMENTAL PROGRAM

3.3.1 Characterization of the Concrete Mix

Concrete properties in terms of compressive and tensile strength, and modulus of elasticity were measured at different ages. These tests were conducted based on the average value of five standard cylinders of 100 × 200 mm for compressive strength and 150 × 300 mm for tensile strength and modulus of elasticity tests at 3, 7, 14, 28 days after casting (Fig. 3.1). Also, the concrete coefficient of thermal expansion was measured using three 76.2 × 152.4 mm cylindrical samples at age 28 days. For each sample, metal reference disk were attached to the surface of the sample using epoxy to identify three gauge lengths as shown in Fig. 3.2. The three gage lengths are at 120 degrees apart. Each gage length measures 102 mm at room temperature (23 ºC). An environmental chamber was used to cycle the temperature between +10 and +50 ºC. A dummy sample was used to monitor the core temperature of the samples and ensure that the thermal equilibrium was reached. A DEMEC gauge with 0.00254 mm accuracy was used to measure the change in gage length with temperature change. Coefficient of thermal expansion was calculated for the heating cycle from +10 to +50 ºC and for the cooling cycle from +50 to +10 ºC. The tests were carried out based on the following test standard methods for each concrete batch to evaluate the properties of the concrete:

- Compressive strength tests (ASTM C 39/C 39M-03);
- Modulus of elasticity test (ASTM C 469-02);
- Tensile strength test (ASTM C 496/C 496M-04);

- Concrete thermal deformation test (ASTM E831);
- Creep coefficient tests (using formulas recommended by ACI 209.2R-08).

Fig. 3.1: Casting test cylinders.

Fig. 3.2: Coefficient of thermal expansion sample.

3.3.2 Test Setup and Prototypes

This study included eight full-size, cast-in-place deck slab prototypes, which were designed to investigate the influence of reinforcement ratio and bar type (GFRP and steel) on transverse early-age cracking in bridge deck slabs under different environmental conditions for a period of 112 days. The test slabs are divided into two series (Fig. 3.3). Series (I), which includes 6 specimens, is related to slabs investigating the effect of changing the longitudinal reinforcement ratio and bar type subjected to shrinkage under laboratory conditions. Series (II), which includes 2 specimens, investigates the effect of freeze-thaw and wet-dry cycles on early-age cracking of GFRP-RC bridge deck slabs. Series (I) consists of five end-restrained RC slabs (SG1, SG2, SG3, SG4 and SS) and one unrestrained/unreinforced slab (F). The five RC slabs includes four GFRP-RC slabs, SG1, SG2, SG3 and SG4, with four different GFRP reinforcement ratios of 0.3%, 0.5%, 0.7%, and 1.1%, respectively, in addition to one steel-RC slab (SS) with a reinforcement ratio of 0.7%. Series (II) includes two slabs, G-FT and G-WD, reinforced with the minimum-acceptable reinforcement ratio as obtained from series (I), which were tested under freeze-thaw and wet-dry cycling conditions.

Figure 3.4 shows prototypes dimensions. According to CHBDC, (Clause 14.13.1.2), the minimum allowable thickness of bridge deck slabs is 175 mm. Accordingly, in this study, a thickness of 180 mm for all test slabs was selected. The full-size, cast-in-place concrete bridge deck slabs (2500-mm long by 765-mm wide) of Series (I) and (II) were constructed and tested under the normal laboratory conditions (Fig. 3.5) and environmentally controlled walk-in chamber (Fig. 3.6), respectively. The effective width-to-length ratio was selected less than 1/3 to ensure that the amount of shrinkage in the longitudinal direction is much more than that in the transverse direction. In other words, there was three times as much concrete that tended to shrink

in the longitudinal direction than in the transverse direction. Consequently, a transverse crack is expected to develop in order to relieve the larger tensile stress in the longitudinal direction. The reinforcement configuration of the test specimens was selected based on the empirical design method recommended by Section 16 of the CHBDC (Clause 16.8.8.1). According to this section, the minimum FRP reinforcement ratio in the longitudinal bottom and top assemblies is 0.35% with top and bottom covers equal to 35±10 mm (CHBDC, Clause16.4.4). All test prototypes had similar top and bottom clear covers (25 and 30 mm, respectively) and a constant spacing of 255 mm for the longitudinal reinforcement (Fig. 3.4 (c)).

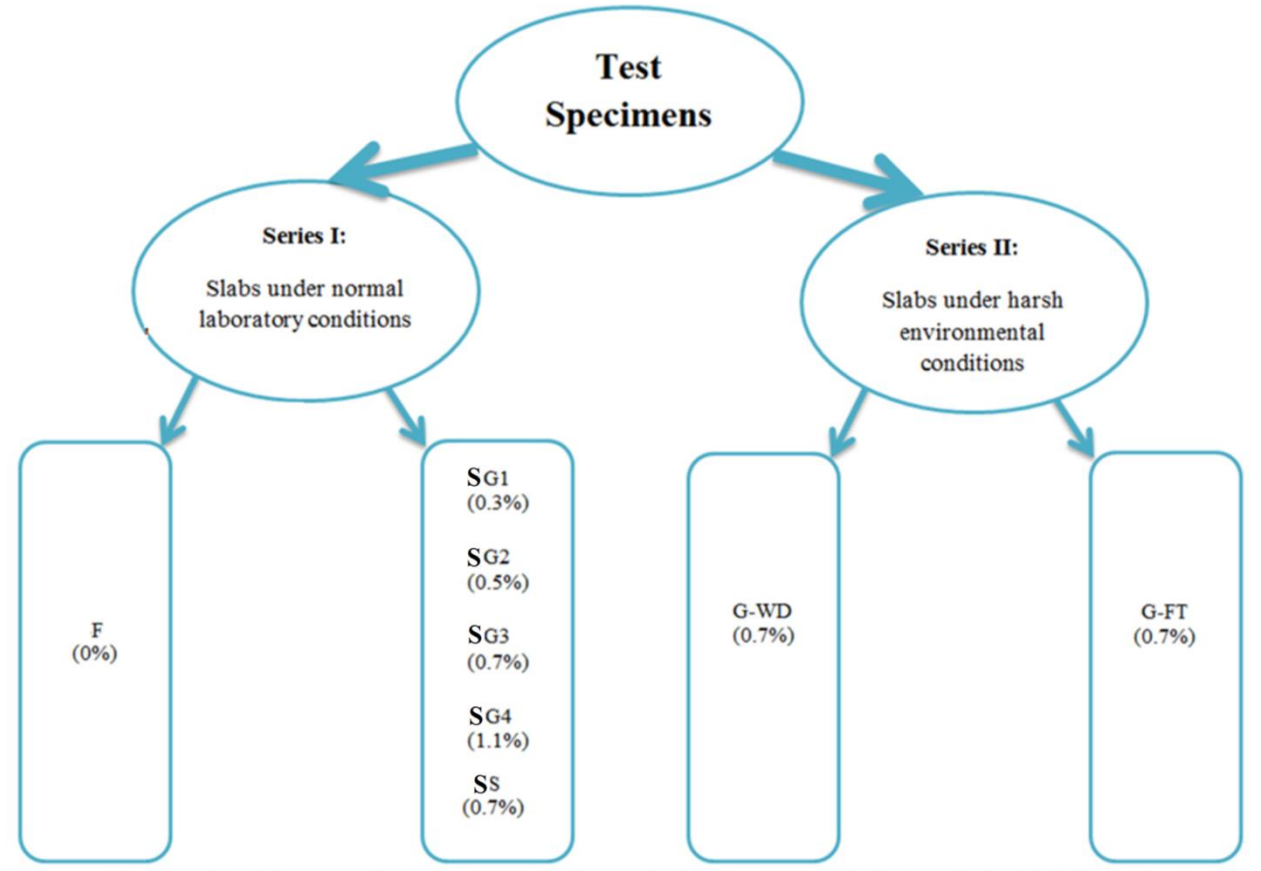

Fig. 3.3: Schematic diagram for test matrix.

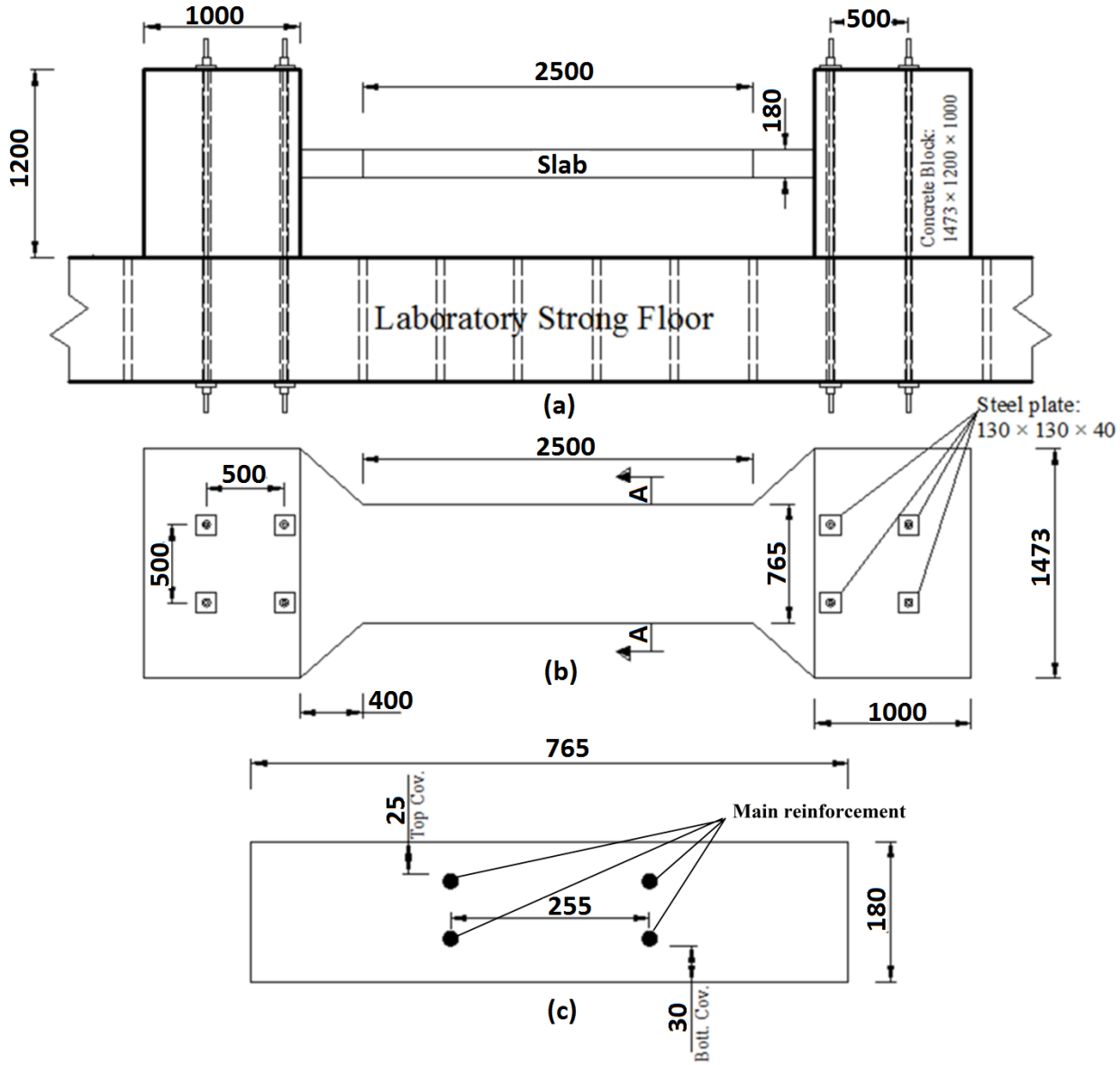

Fig. 3.4: Deck slab dimensions (all dimensions are in mm): (a) side view, (b) top view, and (c) cross-sections A-A

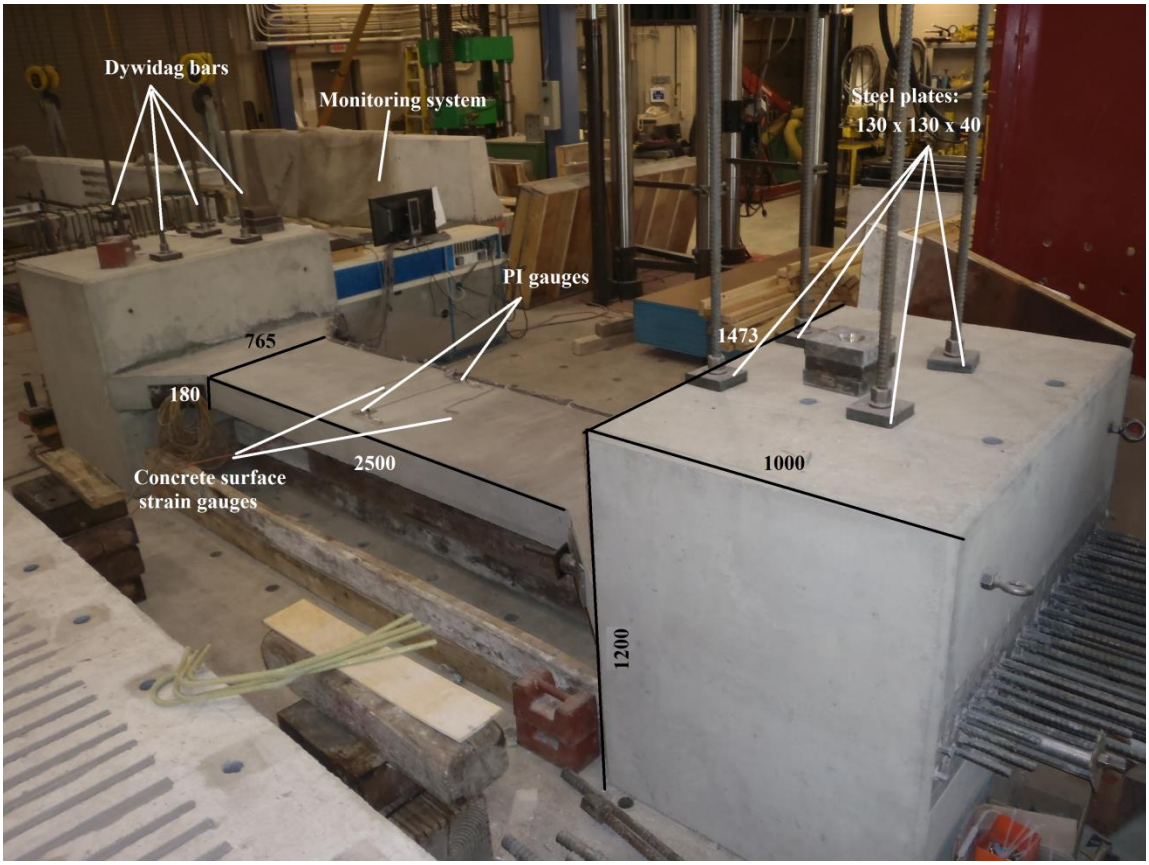

Fig. 3.5: General view of the test setup and specimen under normal laboratory conditions (all dimensions are in mm).

It is well documented in the literature (Nejadi and Gilbert 2004 and Saliba et al. 2011) that the reduction in the cross section can force the main crack to occur at the well-instrumented location. Therefore, in this study the cross section was reduced (notched) to 565 × 150 mm by steel section attached to the forms to ensure that main cracking always occurs at this location (Fig. 3.7), which was depicted by experimental results.

3.3.3 Test Parameters

The effects of following parameters were studied on early-age cracking of RC bridge deck slabs in this research (Table 3.3):

a) Longitudinal reinforcement ratio;

b) Longitudinal reinforcement material (GFRP and steel);

c) Different environmental conditions (wet-dry and freeze-thaw cycles).

For this study, the above parameters are implemented in the experiments as follows:

- ✓ The results of slabs S1 and SG3 were used as control specimens ($\rho = 0.7\%$) to investigate the effect of different reinforcement material on early-age cracking.
- ✓ Using the results of specimens SG1, SG2, SG3, and SG4 to study the effect of GFRP reinforcement ratio with the similar bar spacing (different bar size) were investigated.
- ✓ Specimen G-FT was subjected to freeze-thaw cycling after 7 days of casting for a period of 105 days to evaluate optimum GFRP reinforcement ratio under freeze/thaw conditions.
- ✓ Specimen G-WD was subjected to wet-dry conditions (after 7 days of casting) to investigate the effect of wet/dry conditions on existing early-age cracking

3.3.4 Instrumentations

To measure strains in the GFRP bars in the vicinity of the first crack, three strain gauges were attached to each bar at the top and bottom layers; one centered at the mid-span, and the other two at 50 mm on each side as shown in Fig. 3.8. Two types of strain gauges were used: embedment strain gauges (EGP series) in concrete and linear pattern strain gauges (20CBW series) on the surface of concrete. For each slab, one strain gauge was embedded at the cracking (mid-span) location. The other strain gauge was attached to the surface of concrete at an arbitrary distance of 270 mm (1.5 times slab thickness) away from the mid-span (cracking location) to avoid gauge damage upon the occurrence of first cracking. The internal strain gauge was used to capture the development of tensile strains within concrete up to failure by first cracking, while the surface strain gauge measured the deformation of concrete in the vicinity of the cracking location during

the entire period of exposure. The width of the cracks developed was recorded throughout the test using two PI-gauges. Also, the internal relative humidity was monitored by humidity sensors embedded at the level of the reinforcement layers and mid-depth at an arbitrary distance of 625 mm away from the mid-span (cracking location) to avoid further stress concentration at cracking place. All instrumentation was connected to a DAQ (data acquisition system) controlled by a computer (Fig. 3.9).

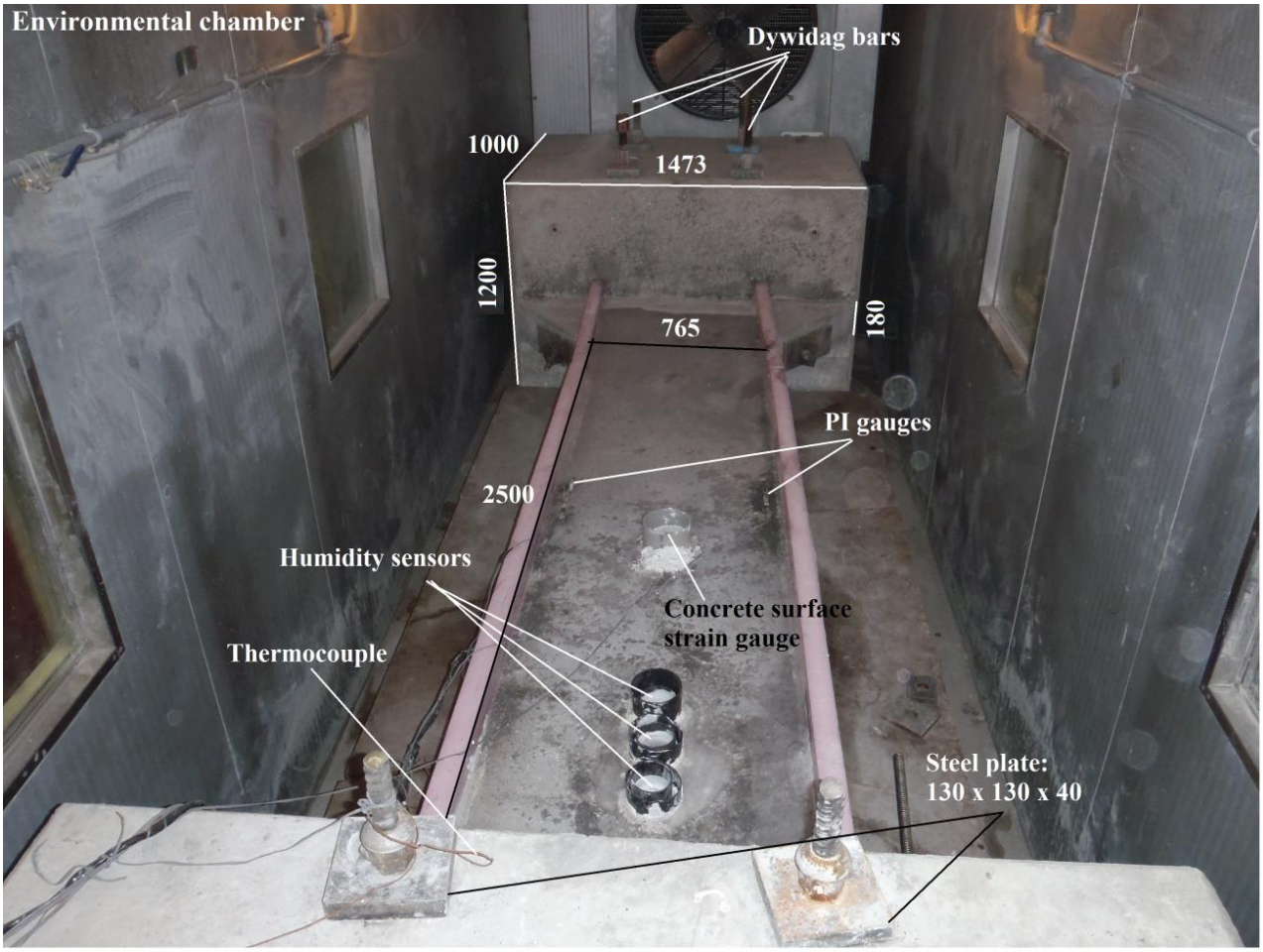

Fig. 3.6: General view of the test setup and specimen into the environmental chamber (all dimensions are in mm).

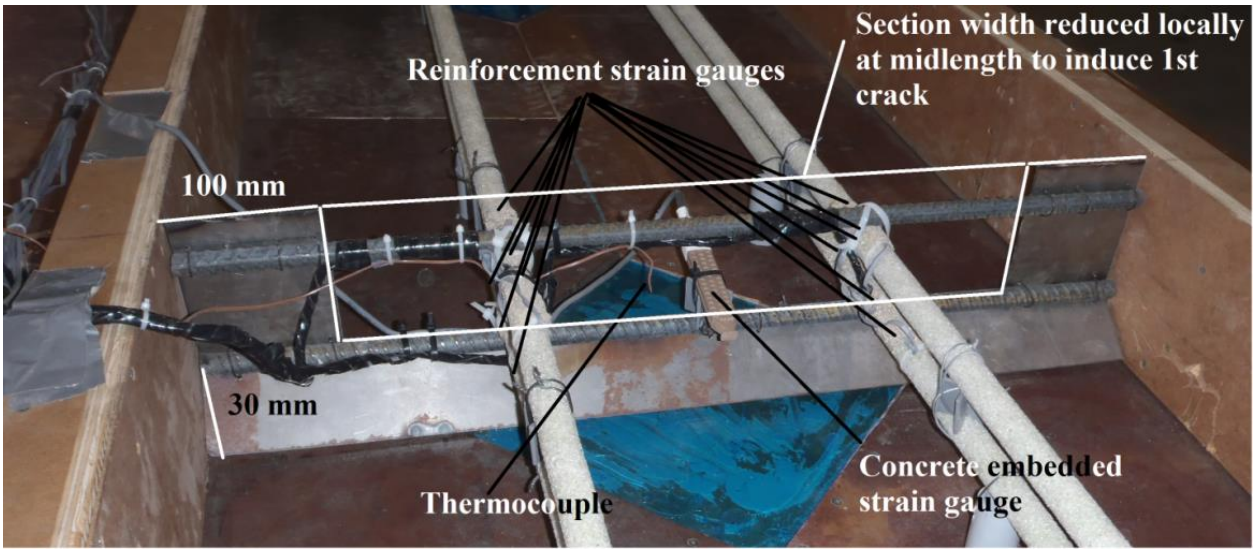

Fig. 3.7: Mid-length details.

Table 3.3: Details of the parameters varied in the tests

Specimen	Bar Dia. (mm)	A_r * (mm^2)	ρ (%)	E×A (kN)	$\frac{\rho_{provided}}{\rho_{min}}$	Temperature (°C)
SG1	9.5	285	0.30	18,525	0.4	20±2
SG2	12.7	508	0.5	33,020	0.7	20±2
SG3	15.9	791	0.7	49,042	1.0	20±2
SG4	19.1	1140	1.1	71,820	1.5	20±2
G-FT	15.9	791	0.7	49,042	1.0	frezze-thaw cycling applied after 7 days of casting
G-WD	15.9	791	0.7	49,042	1.0	Wet-dry cycling applied after 7 days of casting
SS	16	800	0.7	160,000	1.2	20±2
F	-	-	-	-	-	20±2

A_r^*: Total area of 4 longitudinal bars (2 top and bottom)

3.3.5 Test Procedure

Prior to casting, the 2500-mm long slabs were effectively anchored at its ends by 1473×1000×1200 mm concrete blocks (Fig. 3.10), which were clamped (pre-stressed) to the laboratory strong floor using 38-mm diameter dywidag-bars; then the inside surface of the formwork was cleaned and thinly coated with a releasing agent (oil) to prevent adhesion of the concrete (Fig 3.11).

The bottom surface of the slab was supported by three stay-in-place smooth, greasy plates (300 mm × 300 mm, spaced at 1250 mm as shown in Fig. 3.12) to reduce the effect of slab's self-weight on the reinforcement strains. For the first 24 hours after casting, a plastic tent was built around the test prototypes and cylinders while electrical heaters were used to maintain the internal concrete temperature at 35 °C without moist curing (Fig. 3.13).

Subsequently, the tent and formwork was removed, then PI-gauges were attached to the concrete surface, and initial strain measurements were recorded. During the first 24 hours, the ambient conditions around the slab (under tent) were 40 °C with 30-40% RH. In the meantime, the average internal temperature and RH measured at the top reinforcement level were 35 °C and 90 %, respectively. After the tent was removed, the specimens were left in laboratory conditions (20 ± 2 °C and 50-70 % RH) over 111 days. During that period the internal temperature at the top reinforcement level was 20 ± 2 °C while the RH decreased from 95 to 70%. In order to increase internal relative humidity (RH) for the slabs of Series (II) (G-FT and G-WD), water was poured into the surface reservoir (approximately 5-mm thick) constructed by peripheral foam dykes at the outer edge of the slabs G-FT and G-WD for freezing-thawing and wetting cycles (Fig. 3.14).

Using the concrete cylinders (Fig. 3.15), the average compressive (ASTM C39M-03) and splitting tensile (ASTM C496M-04) strengths and the modulus of elasticity (ASTM C469-02) were obtained after 1, 3, 7, 14, 21 and 28 days (Table 3.4) to determine the development of concrete properties (within a standard deviation of 10% from the average value).

3.3.6 Environmental Conditioning Schemes

3.3.6.1 Freezing-thawing cycles

Different freezing-thawing conditioning schemes had been used by researchers to study the behaviour of RC elements externally or internally reinforced with FRP bars (Laoubi et al. 2006 and Alves et al. 2011). In this research, the temperature profile of Standard Test Method for Resistance of Concrete to Rapid freezing-thawing (ASTM C-666 M-03 2008) was adopted. In this standard, the freezing-thawing cycles consist of alternately lowering the temperature from +4 to -18 ºC for freezing and raising it from -18 to +4 ºC for thawing. Thawing time should not be less than 25% of the total freezing-thawing time. In order to reach the standard conditions in the bottom reinforcement level of the slab, the applied freezing-thawing cycles consisted of alternately decreasing the environmental chamber temperature from +22 to -25 ºC for freezing and raising it from -25 to +35 ºC for thawing at a rate of 1.55 cycles/day to achieve the ASTM temperature and duration requirements at the level of GFRP reinforcement. Figure 3.16 shows the reading of thermocouples embedded in specimen G-FT at the level of bottom reinforcement compared to the air temperature inside the chamber. Specimen G-FT was subjected to 163 freezing-thawing cycles over 105 days. Figure 3.17 indicates that ponded water (3-5 mm) on the top of slab G-FT increased the average internal humidity to approximately 99% (i.e. beyond the critical saturation level of 90%).

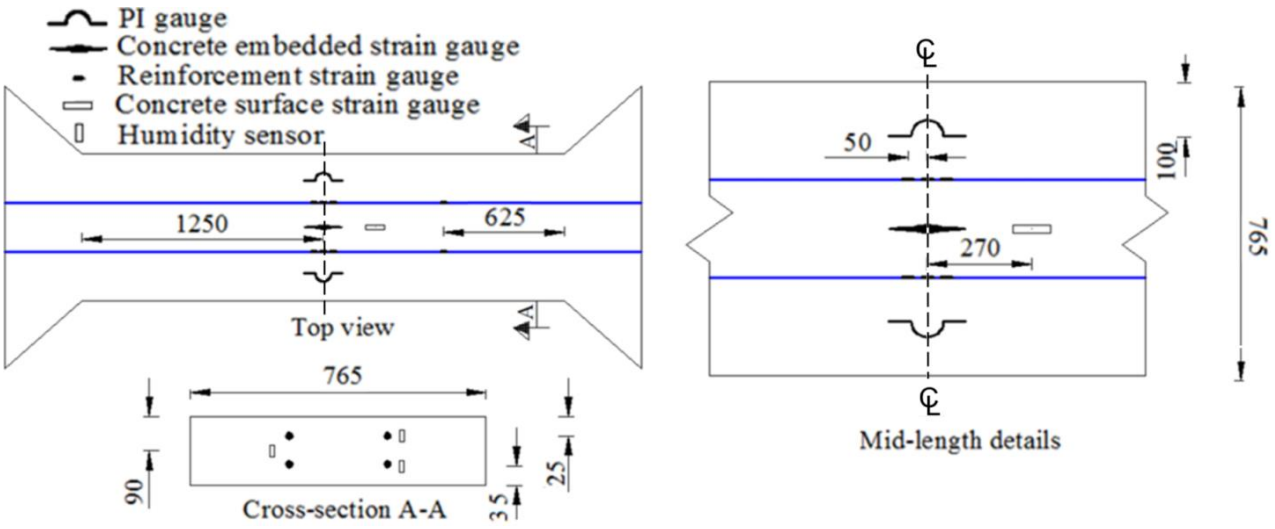

Fig. 3.8: Typical instrumentation of deck slabs (all dimensions are in mm).

Fig. 3.9: Measurement instruments; DAQ Amplifier, PI gauges, and Microscope.

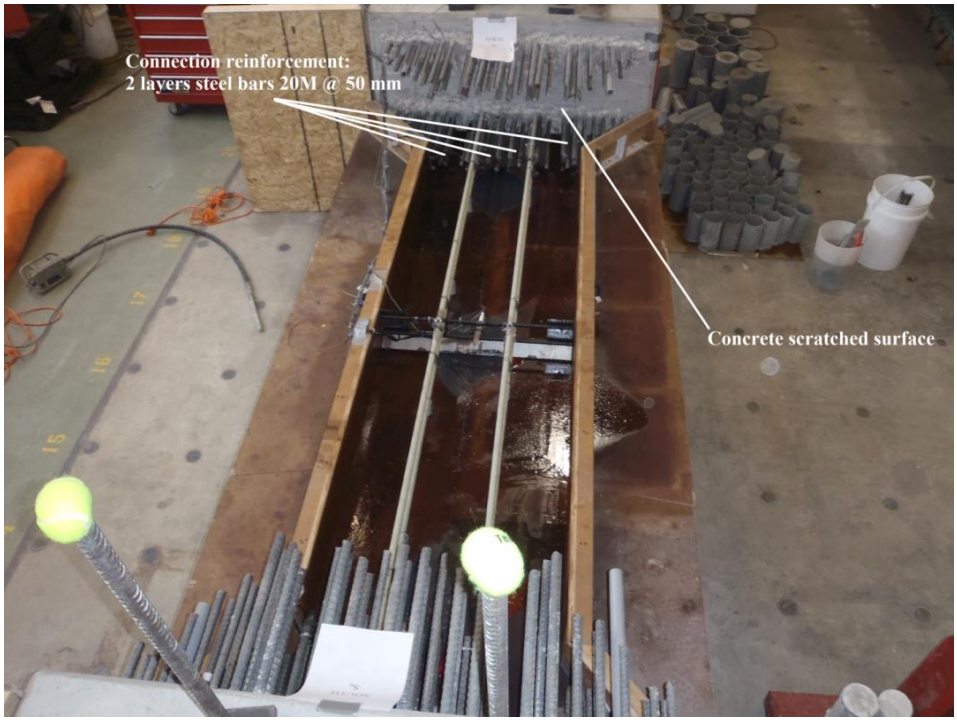

Fig. 3.10: Slab ends effectively held in position and restrained against translation.

Fig. 3.11: Formwork is thinly coated with oil to prevent adhesion of the concrete.

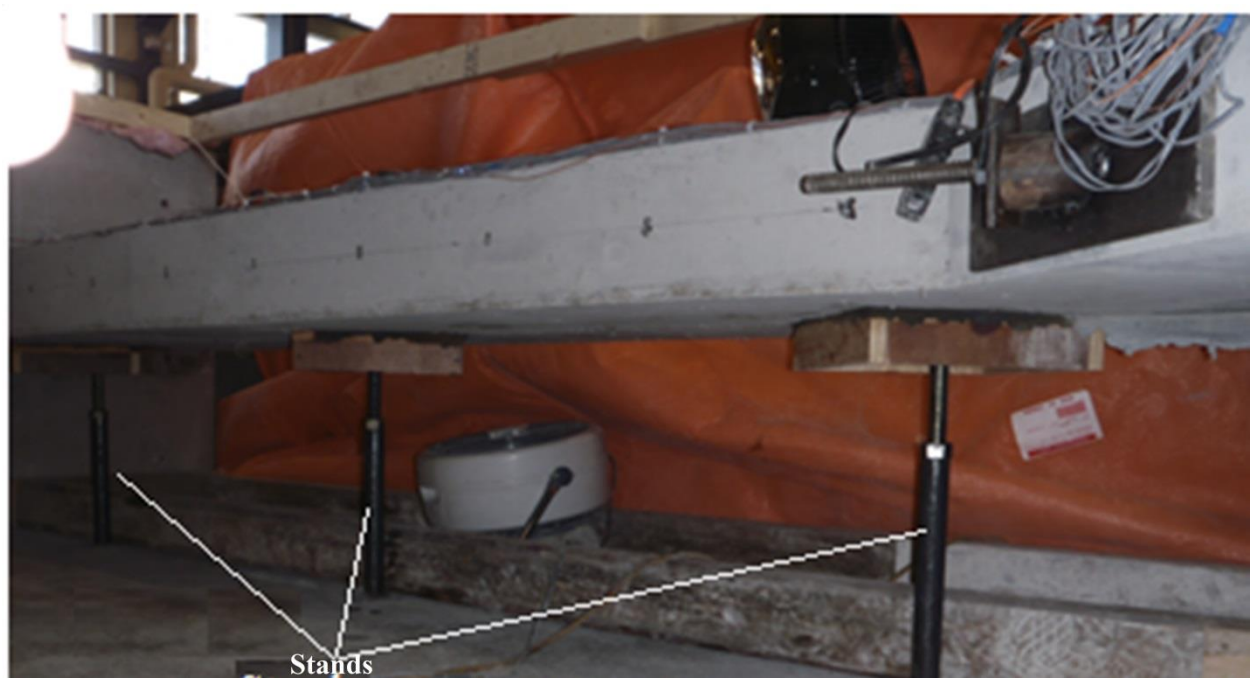

Fig. 3.12: Smooth supports at the bottom surface of the slabs to eliminate flexural action.

Fig. 3.13: Temperature control during the first 24 hours.

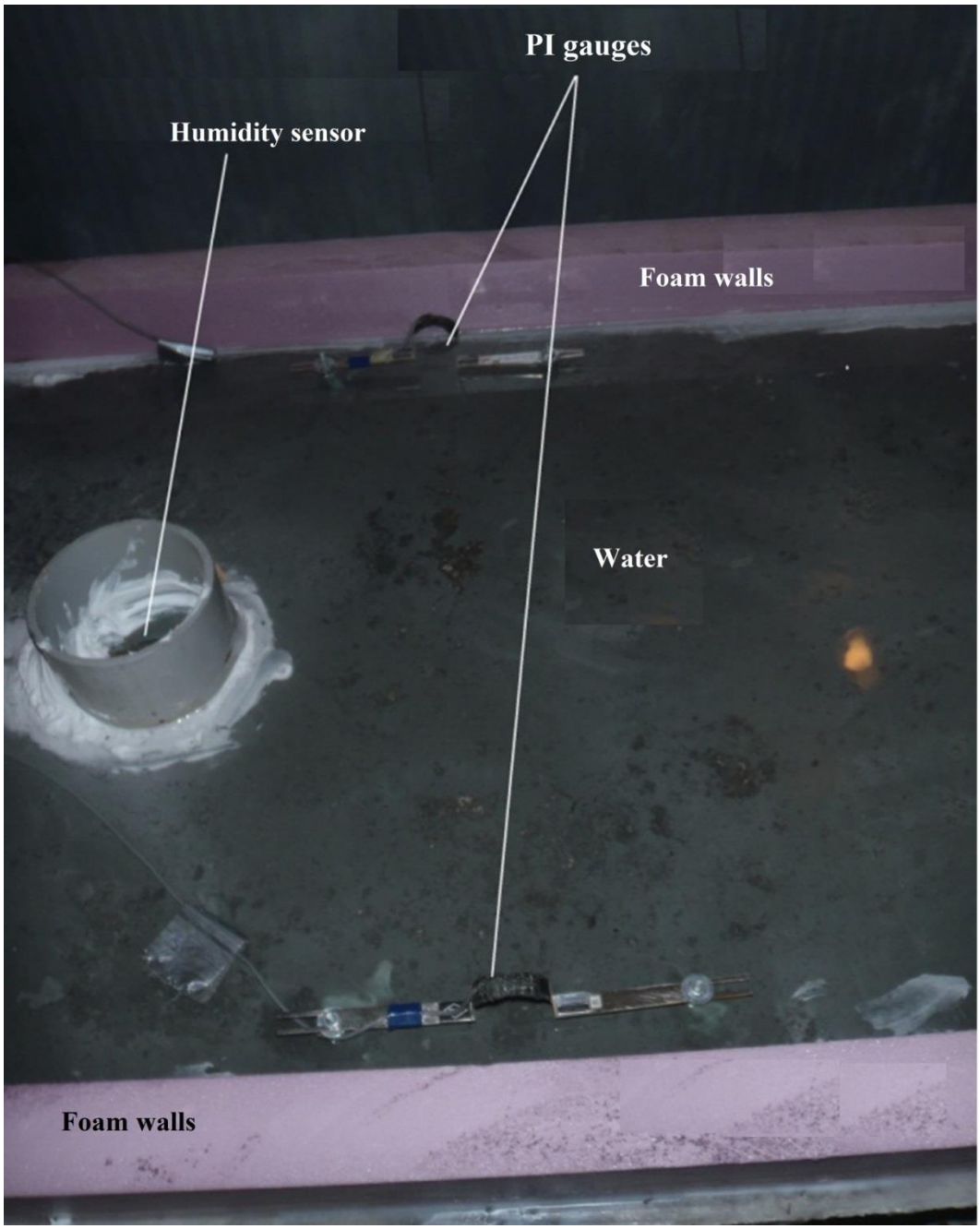

Fig. 3.14: Water was poured into the surface reservoir (for slabs G-FT and G-WD).

Fig. 3.15: Equipment used in concrete material testing.

Table 3.4: Compressive, tensile and E-modulus test results for concrete under different environmental conditions

Ambient conditions	**N**	**N**	**N**	**N**	**D/W**	**F/T**	**N**	**D/W**	**F/T**	**N**	**D/W**	**F/T**
Property	Age (days)											
	1	3	7	14	14	14	21	21	21	28	28	28
Compressive Strength (MPa)	7±0.50	14±0.27	34±2.60	35±3.40	37±1.70	33±1.58	36±0.91	38±0.50	32±1.90	38±1.40	41±2.50	35±2.3
Tensile Strength (MPa)	0.6±0.05	1.3±0.09	3.4±0.33	3.5±0.26	3.9±0.30	3.3±0.20	3.6±0.10	3.7±0.17	3.1±0.38	3.7±0.20	3.9±0.19	3.3±0.26
Modulus of Elasticity (GPa)	-	18±0.72	21.1±1.15	21.2±2.09	21.8±1.21	21.3±1.90	21.1±1.01	21.8±1.31	21.1±1.21	21.8±1.66	22.2±1.47	21±1.73

N: Normal laboratory conditions (22°C and 50 to 60% RH), D/W: Drying and wetting cycling (35°C to 22°C and 100 to 30 % RH respectively), and F/T: Freeze-thaw cycling (-18 °C to +4 °C and 100% RH).

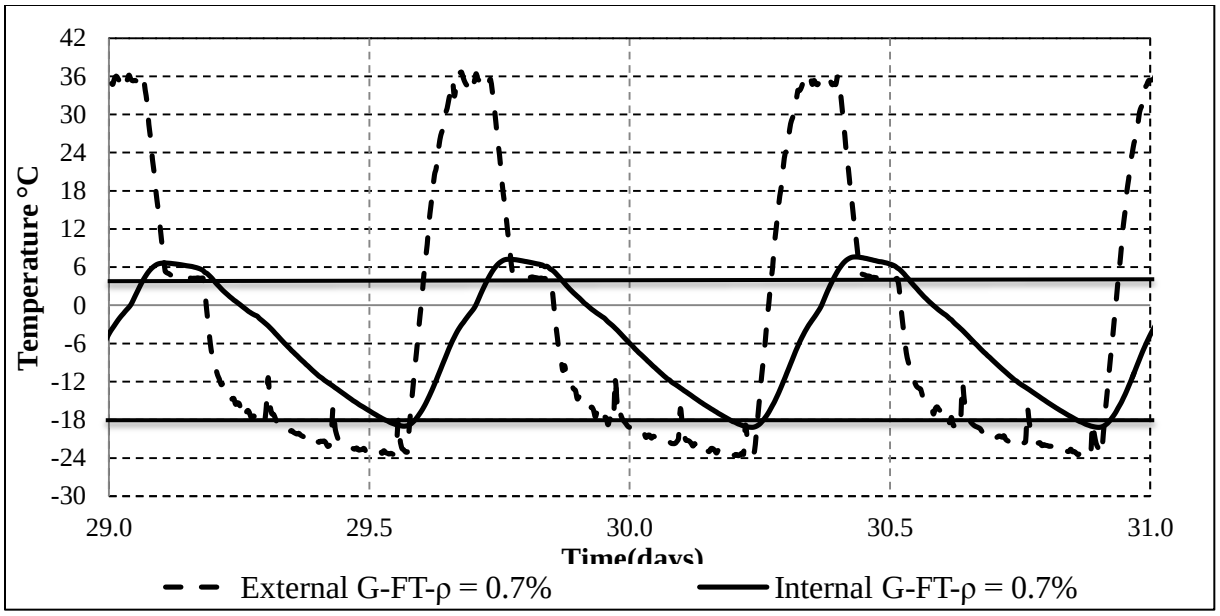

Fig. 3.16: A part of the freeze-thaw profile for specimen G-FT.

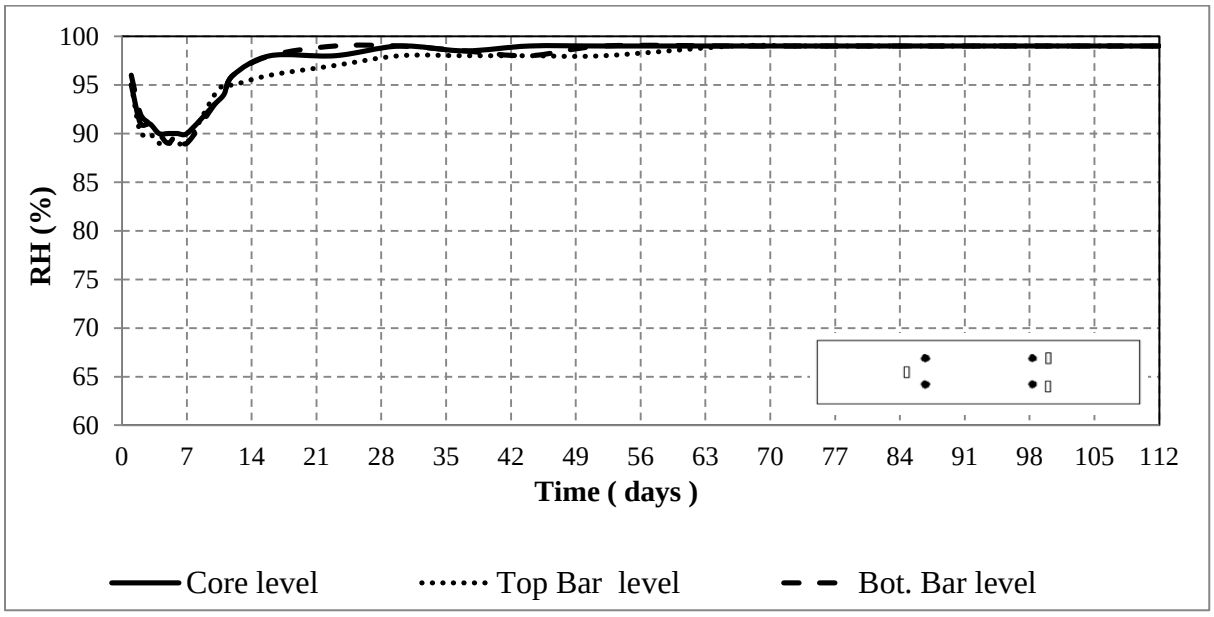

Fig. 3.17: Relative humidity readings for the slab G-FT subjected to the freeze-thaw.

3.3.6.2 Wetting-drying cycles

It should be noted that there are no standard test methods for the wetting-drying exposure of concrete. The cyclic regime and the total number of cycles (five cycles) in this study were selected similar to that adopted by Zhang et al. (2012) to achieve significant humidity changes at the reinforcement level of the bridge deck slabs. Each wetting-drying cycle started with 14 days of drying at 35±2 °C and 30% RH followed by 7 days of wetting at 22±2°C and 100% RH. Figure 3.18 shows the reading of humidity sensors embedded in the test specimen at the different levels of the cross section compared to the humidity in the chamber.

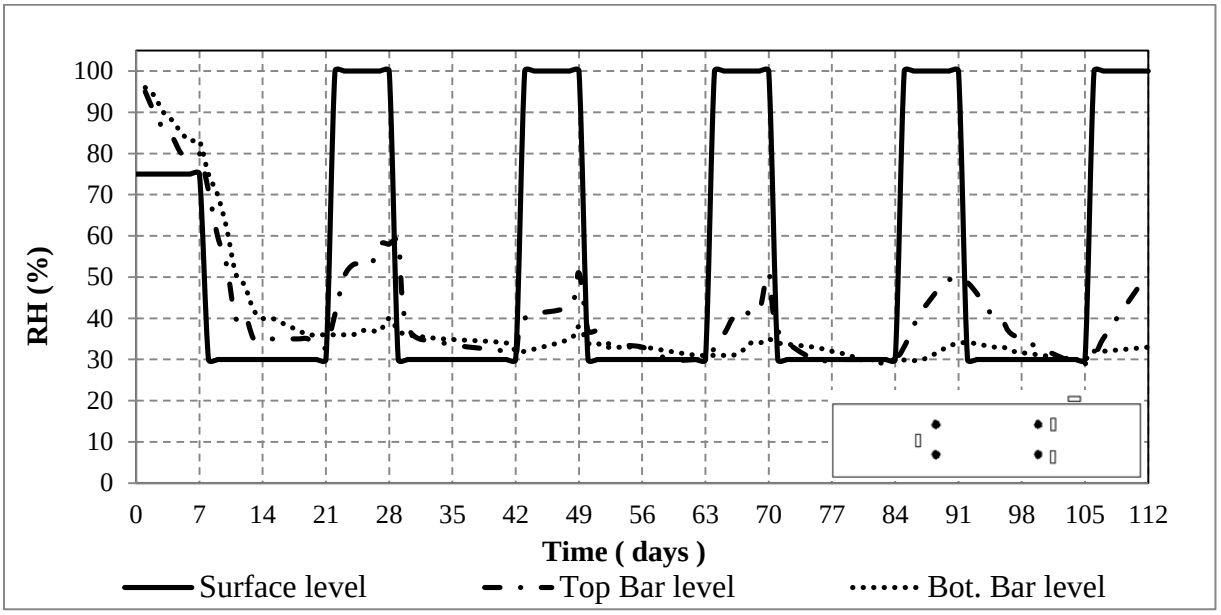

Fig. 3.18: Relative humidity readings for the G-WD subjected to wet-dry exposure.

3.4 MICROSTRUCTURE TESTS

In additional to the early-age cracking of restrained concrete slabs exposed to harsh conditions, they were vulnerable to material degradation especially at the mid-length (in the vicinity of the crack) due to temperature and humidity variations. To capture this trend, three materials tests Dynamic Modulus of Elasticity (DME), Rapid Chloride Permeability Test (RCPT), and

Scanning Electron Microscopy (SEM) were conducted on cores extracted from the three GFRP-RC slabs. A total of twelve 100-mm diameter cores were extracted; four cores for each slab (close and away from left and right sides of the crack). All cores were extracted from slabs at the end of the test period (112 days). For the DME test, full length cores were used while for the other two tests, top 50-mm thick slices were cut from the cores extracted from different locations in the slabs, as shown in the Fig. 3.19.

Fig. 3.19: Taking cores from the slab.

3.4.1 UPV Test

To determine the internal conditions of the cementitious matrix in terms of structural stiffness and integrity, the dynamic modulus of elasticity (DME) was determined for all cores from the ultrasonic pulse velocity (UPV) measurements (Fig. 3.20) according to ASTM C597 (2009).

Fig. 3.20: UPV test machine.

According to the ASTM C597 specifications, DME test was performed based on the average value of three pulse velocities, were measured, from the longitudinal direction of the cores (cylinders) using the Eq. 3.1.

$$E_d = \frac{\vartheta^2 \rho(1+\mu)(1-2\mu)}{(1-\mu)} \qquad \textbf{Eq. 3.1}$$

Where, E_d = Dynamic Modulus of Elasticity (DME) (GPa), ϑ = Pulse Velocity (PV) (m/s), ρ = Concrete density (kg/m^3), μ = Dynamic Poisson's ratio (assumed to be 1.5).

3.4.2 Rapid Chloride Penetrability Test (RCPT)

To evaluate the interconnectivity of the pore structure in the concrete slabs after being subjected to different environmental conditions, the rapid chloride penetrability test (RCPT) was performed for the cores according to ASTM C1202 (2012) (Standard Test Method for Electrical Indication of Concrete's Ability to Resist Chloride Ion Penetration). The 50-*mm* thick discs were cut from top layer of the cores as the test samples (Fig. 3.21). These discs were air-dried in the laboratory for one hour and then their side surfaces were coated with rapid setting epoxy to reduce moisture evaporation and leakage of solution during testing. Subsequently, the concrete discs were placed in a vacuum desiccator under vacuum pressure for three hours.

Fig. 3.21: Disks preparation for RCPT.

In the meantime, the required amount of water was boiled for de-aeration and allowed to cool down to ambient temperature. After three hours of vacuuming, de-aerated water was allowed to enter into the desiccator while the vacuum pump was still running. Subsequently, for additional one hour, the vacuum pump was operated and then the valve was opened to allow air to enter

into the desiccator. The specimens were kept in the desiccator and soaked under water for 18 hours before the actual test. On the following day, the concrete discs were put in the test cells, where one compartment was filled with 3% NaCl solution (cathode) while the other compartment was filled with 0.3 N NaOH solution (anode). During the test period (six hours), 60 V DC was applied to the cell compartments, while the temperature of sodium chloride solution was continuously monitored by a thermocouple. The computer connected to the microprocessor power supply recorded all the data during the entire test in terms of passing charges in Coulombs through concrete to determine the penetrability class according to ASTM C1202 (Fig. 3.22).

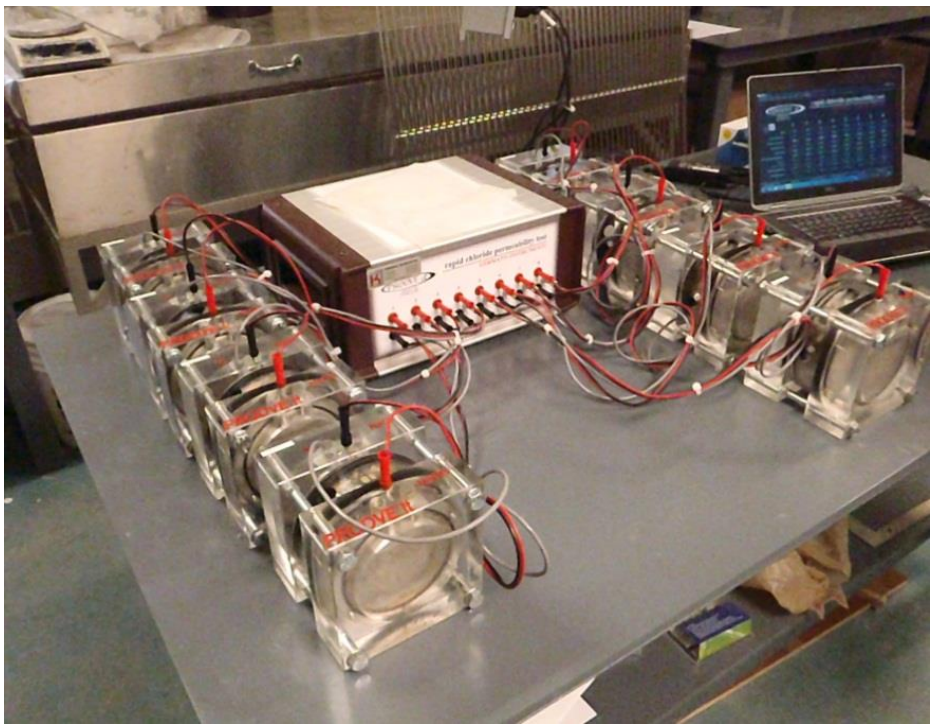

Fig. 3.22: RCPT test equipment.

After the RCPT, the specimens were axially split and sprayed with a silver nitrate solution, which forms a white color in approximately 15 minutes, to measure the physical penetration depth. The average depth of the white precipitate was determined at five different locations of

each half specimen. This depth is considered to be an index of the ease of ingress of chloride ions, and thus the connectivity/deterioration of the microstructure (Bassuoni et al. 2006).

3.4.3 Backscattered Scanning Electron Microscopy Test (BSEM)

To supplement the results of UPV and RCPT, the alteration of microstructure of concrete was also assessed by backscattered scanning electron microscopy (BSEM) (Fig. 3.23) on thin sections from cores extracted from G-FT and G-WD in the vicinity and away from the main crack. The polished sections were prepared from fracture surfaces that were dried at 40°C for 24 h, impregnated with low-viscosity epoxy resin under pressure, cut, polished and carbon coated (Fig. 3.24).

Fig. 3.23: Backscattered scanning electron microscopy (BSEM).

Fig. 3.24: Typical prepared sample for the backscattered scanning electron microscopy (BSEM) test.

CHAPTER 4: RESULTS AND DISCUSSION - LABORATORY CONDITIONS

EFFECT OF REINFORCEMENT RATIO

4.1 GENERAL

It is documented that no experimental data is available for the minimum FRP reinforcement ratio to control shrinkage and temperature cracking in FRP design codes and guidelines (CHBDC 2009, CSA/S806 12). Most of these codes and guidelines are based on modifying corresponding formulas originally developed for steel bars and take into account the difference in properties and behaviour between FRP and steel material. The objective of this chapter is to summarize the experimental results for six full-scale of Series (I), which includes 6 full-scale slabs, investigating the effect of changing the longitudinal reinforcement ratio (0.3, 0.5, 0.7 and 1.1%) and bar type (steel) subjected to shrinkage under laboratory conditions. Also, one identical restrained-free plain concrete slab was tested to measure the total free shrinkage strain of the slab during the test period. The performance of the specimens is assessed and discussed in terms of concrete cracking pattern, width, and spacing, and strains in the reinforcement and concrete. The experimental results were compared with provisions of the CHBDC (CSA 2006) and predictions from a published analytical model (Gilbert 1992) for estimating crack width of steel-RC structures.

4.2 SLABS SUBJECTED TO LABORATORY CONDITIONS

4.2.1 General Observation

The width of cracks in the restrained slabs varied according to the environmental exposure and different reinforcement material. While the magnitude of crack width depends on several factors such as degree of restraint, quality of bond between concrete and reinforcement, size and

distribution of bars, concrete quality and ambient conditions, the studied variables in this study were the environmental conditions and reinforcement ratio and material. For each slab, the crack width was considered as the average of the measured value at two locations across the slab width at mid-span. Generally, the first crack in all specimens was observed within the first three days after casting in the transverse direction before exposure. Figure 4.1 shows the cracking pattern for all the slabs at the notched (mid-span) location. The cracks, which usually extended into the full depth of slabs, typically occurred at mid-span (notched location). For the RC slabs, the bar strain was presented as average strain readings of all instrumented bars (top and bottom) in the vicinity of crack at mid-span. Prior to cracking the average strain level remained under 300 $\mu\varepsilon$. The top and bottom reinforcement carried the full restraining force at each crack, while the stress in the concrete was zero (Fig. 4.2). Once the crack formed at the mid-span, the strains increased significantly. The internal concrete strain at cracking location was considered the embedment concrete strain gauge reading before cracking, while due to damage of the internal gauge at cracking time the surface concrete strain was presented using surface strain gauge 270 mm away from the cracking location. Figures 4.2 shows the internal strain of the concrete at cracking, once the early age cracks became visible for specimens SG1, SG2, SG3, SG4, and SS the measured concrete internal tensile strains were 336, 315, 293, 213, and 212 $\mu\varepsilon$, respectively. For all specimens after cracking, the concrete surface strain in the vicinity of the first crack changed to a compressive strain. Once cracking occurred, the stiffness of slab in the vicinity of cracking reduced depending on the reinforcement ratio and modulus of elasticity on either side of the crack shortens elastically.

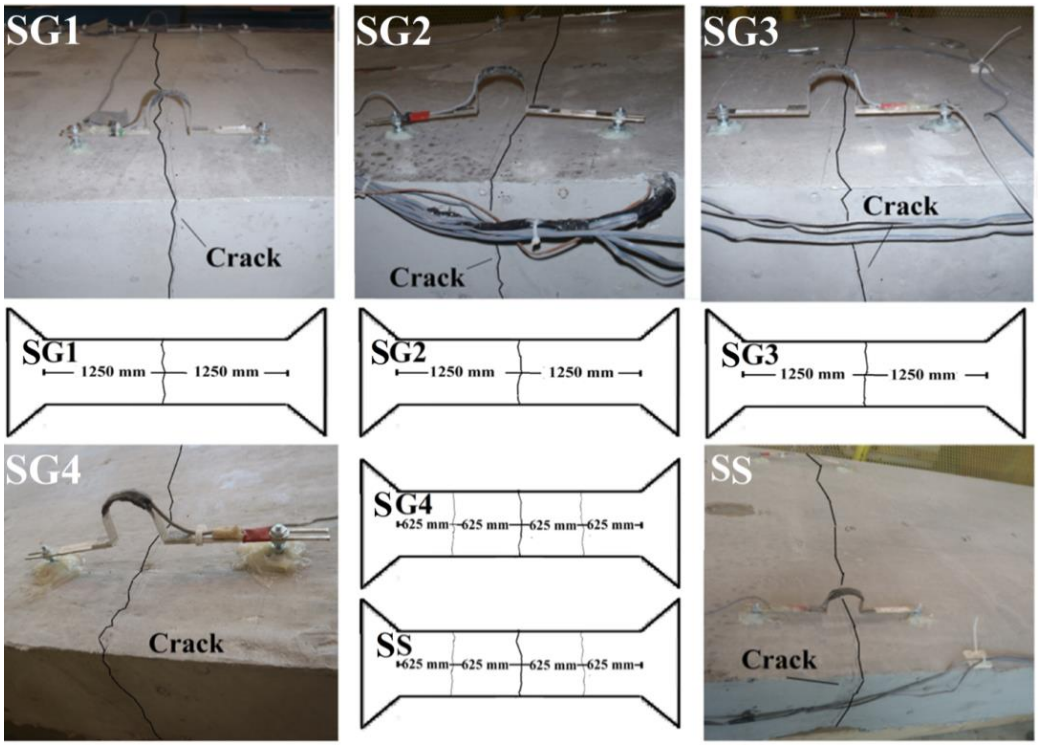

Fig. 4.1: Final crack pattern in the specimens.

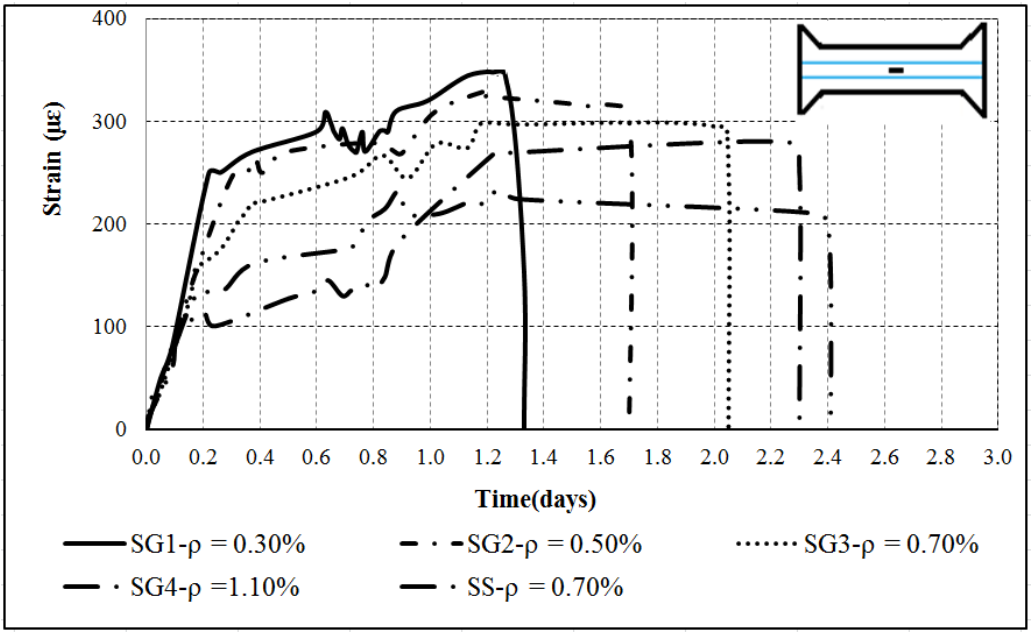

Fig. 4.2: Internal strain of concrete at cracking at cracking time.

If the volumetric change of concrete due to shrinkage and thermal stresses is restrained, tensile stresses will develop in concrete. If the induced tensile stresses are higher than the tensile strength capacity of the concrete, the concrete will crack. Figure 4.3 represents that the total free volumetric instabilities of free restraint slab F due to shrinkage under laboratory conditions was 171 $\mu\varepsilon$ at the end of test period. In this research increasing ambient temperature to 35 °C in the first day after casting without moist curing followed by exposing the slabs to an air flow for 6 days, accelerated the amount of shrinkage to 159 $\mu\varepsilon$ within first week.

4.2.2 Characteristics of cracks

4.2.2.1 Slab SG1

Figure 4.4 shows the change in crack width of the Specimen SG1 over 112 days. The first crack occurred for Slab SG1 within 31 hours. Primarily, the width of a crack in a restrained slab varied depending on the bonded reinforcement ratio and material crossing the crack. In the slab SG1 (ρ = 0.3%) the crack width reached the allowable value of 0.5 mm (ACI 440 2006, CSA 2006) after 40 hours. This crack width grew to 0.73 mm after 112 days test period.

4.2.2.2 Slab SG2

The first crack occurred for SG2 within 37 hours. Fig. 4.5 shows the change in crack width over 112 days. For slab SG2 (ρ = 0.5%) the crack width reached the allowable value of 0.5 mm (ACI 440 2006, CSA 2006) after 42 hours. This crack width grew to 0.64 mm after 112 days.

4.2.2.3 Slab SG3

For Slab SG3 the first crack occurred for slabs SG3 within 48 hours. Figure 4.6 represents the change in crack width over 112 days. The final crack width for slabs SG3 (ρ = 0.7%) was 0.33 mm (lower that 0.5 mm recommended by CHBDC) after 112 days of exposure to laboratory

conditions, in the next phase of the experimental works, to assess the effect of different environmental conditions on early age cracking the slab SG3 (ρ = 0.7%) is selected as slab with optimum reinforcement ratio.

4.2.2.4 Slab SG4

Figure 4.7 shows the change in crack width for specimen SG4 over 112 days. For this slab the first crack occurred within 55 hours. The final crack widths grew to 0.24 mm (lower that 0.5 mm recommended by ACI 440 2006, CSA 2006) after 112 days. Further volumetric instability in the slab SG4 causes second and third cracks occurred at 63 days of casting on both sides of the first crack. While additional shrinkage in slabs SG1 to SG3 increases the crack width. An increase in the GFRP reinforcement ratio leads to less stiffness reduction at first cracking (at mid-span), thus the restraining force after cracking remains high and the stress in bars is low. Therefore with a high restraining force, due to future drying shrinkage or any environmental temperature variation, the concrete in regions away from the first crack tends to experience further cracking.

4.2.2.5 Slab SS

Figure 4.8 illustrates the change in crack width over 112 days. The first crack occurred for slab SS within 58 hours. For this slab (reinforced with steel ρ = 0.7%) the final crack widths grew to 0.18 mm after 112 days. Further shrinkage and higher cross-section stiffness at cracking location due to higher modulus of elasticity of steel-reinforcement (E_s = 200 GPa) compared with the same GFRP-reinforcement ratio (E_{GFRP} = 62 GPa) causes second and third cracks occurred at 19 days of casting on both sides of the first crack. While additional shrinkage in slab SG3 increases the crack width. An increase in the reinforcement modulus of elasticity leads to less stiffness reduction at first cracking (at mid-span), thus the restraining force after cracking remains high and the stress in bars is low. Therefore with a high restraining force, due to future drying

shrinkage or any environmental temperature variation, the concrete in regions away from the first crack tends to experience further cracking.

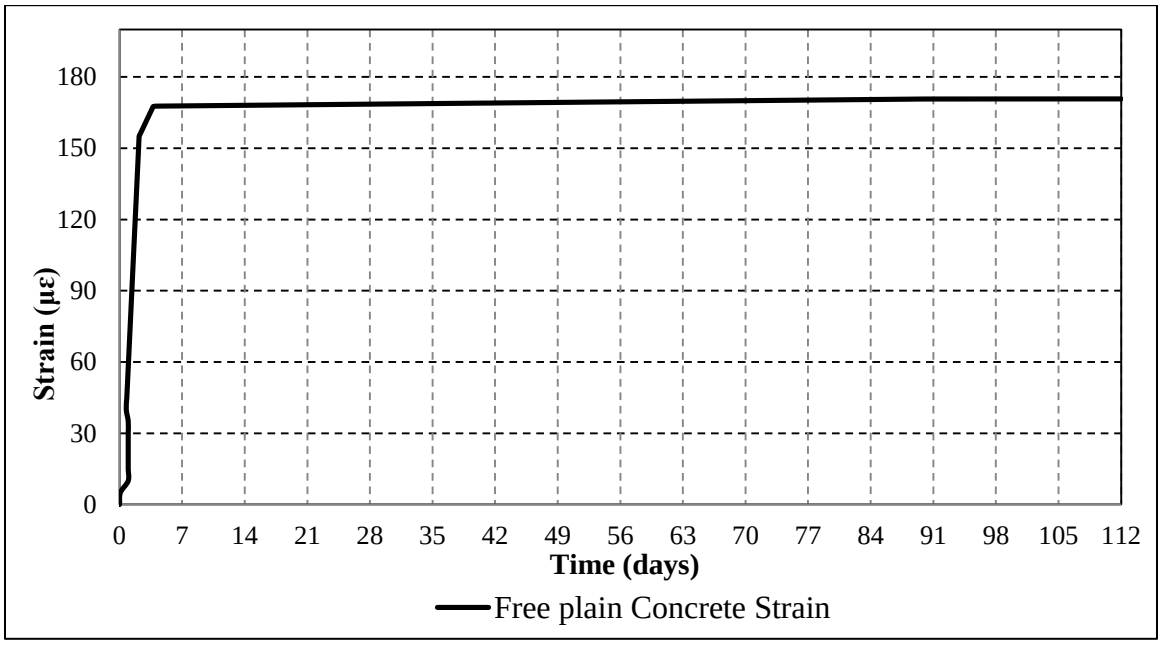

Fig. 4.3: Total free shrinkage of the plain concrete slab F.

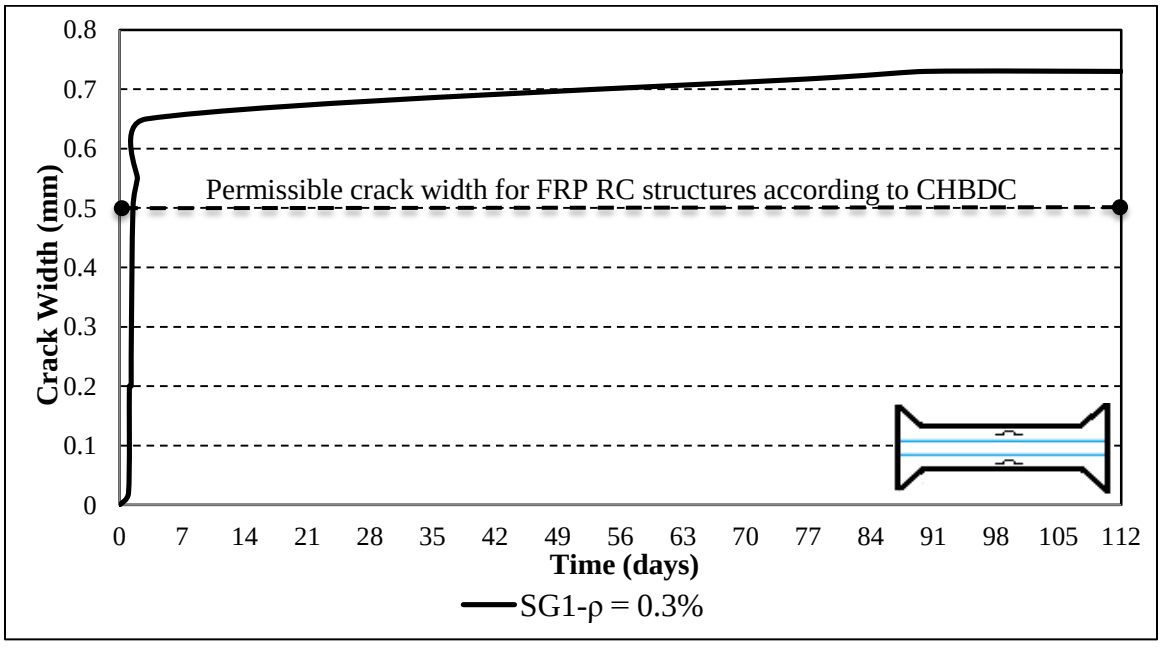

Fig. 4.4: Development of crack width with time (slab SG1).

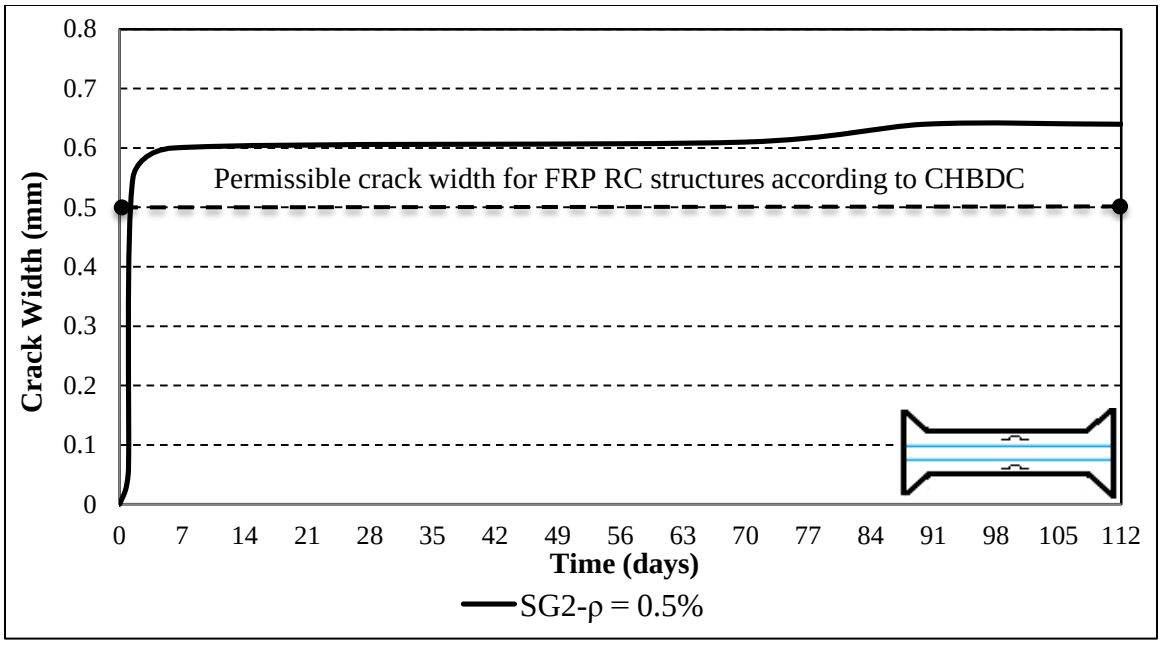

Fig. 4.5: Development of crack width with time (slab SG2).

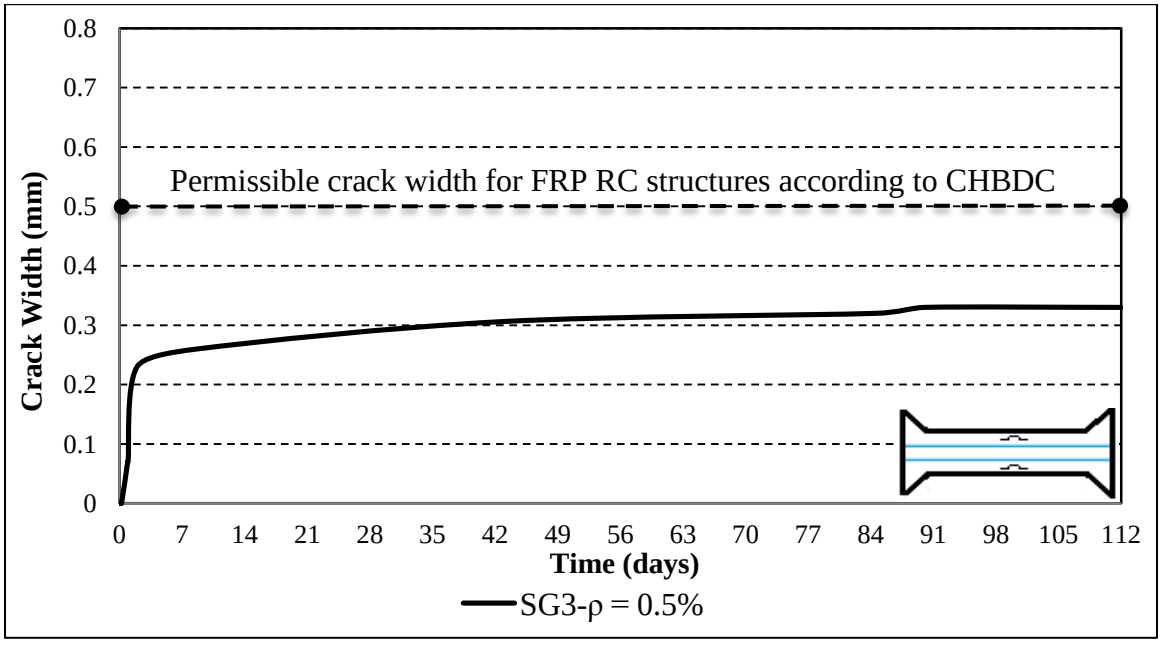

Fig. 4.6: Development of crack width with time (slab SG3).

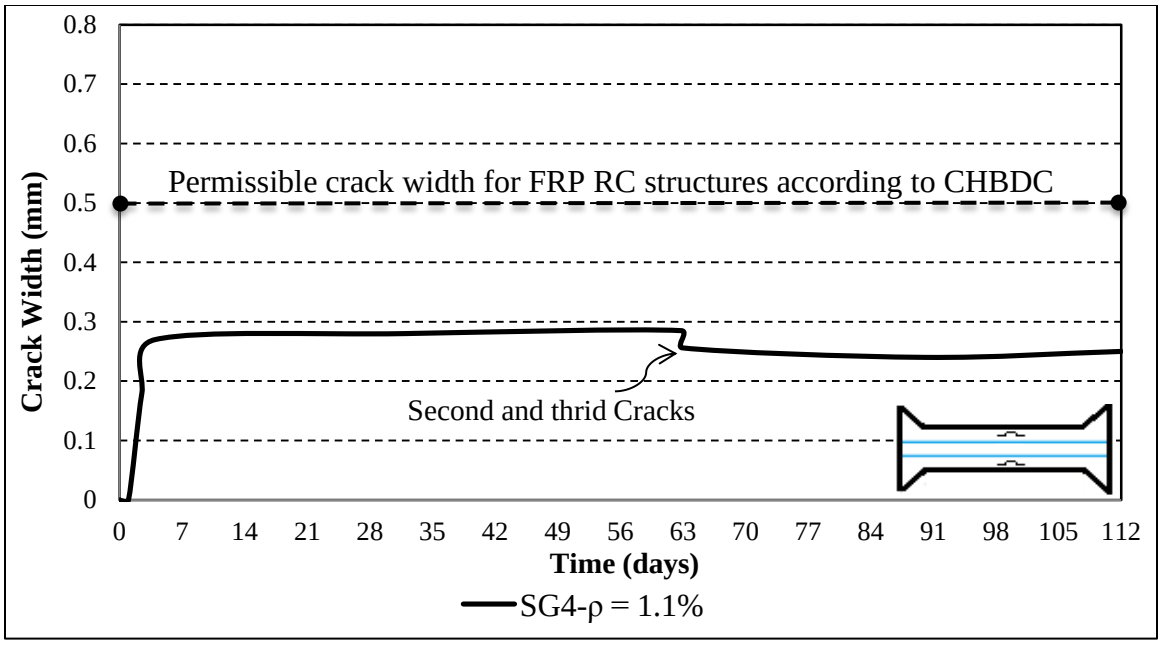

Fig. 4.7: Development of crack width with time (slab SG4).

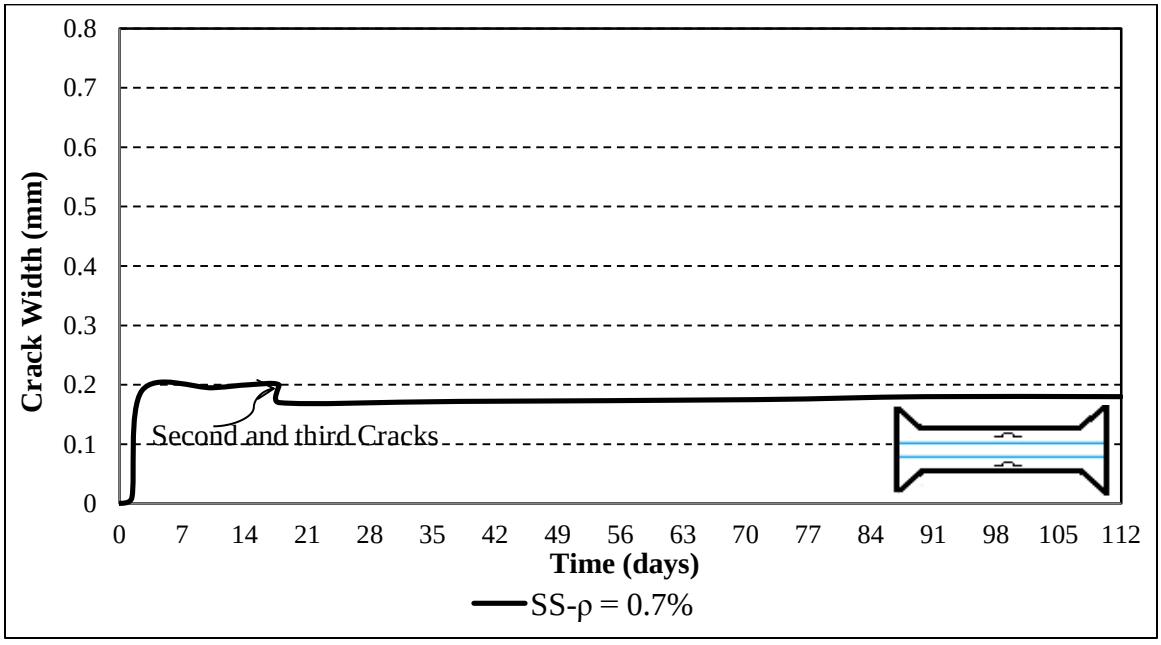

Fig. 4.8: Development of crack width with time (slab SS).

4.2.3 Tensile Strains in Reinforcement

4.2.3.1 Slab SG1

Prior to cracking the average strain level remained under 100 με, but once crack formed at the mid-span, for specimen SG1 the average strain in reinforcement increased promptly to 3000 με, while the strain away from the cracking location was still less than 300 με. Figure 4.9 shows the average strain readings of all instrumented bars (top and bottom) in the vicinity of crack at mid-span. For slab SG1, the final average strains reached to 3750 με at the end of test period.

4.2.3.2 Slab SG2

Figure 4.10 illustrates the average strain readings of all instrumented bars (top and bottom) in the vicinity of crack at mid-span. Prior to cracking the average strain level remained under 100 με, but once crack formed at the mid-span, for specimen SG2 the average strain in reinforcement increased promptly to 1900 με, while the strain away from the cracking location was still less than 300 με. In the slab SG2 the final average strains was 2480 με after 112 days.

4.2.3.3 Slab SG3

For specimen SG3 prior to cracking the average reinforcement strain was less than 100 με, once crack formed this value jumped to 1450 με in the notched location. The average strain level location was still less than 300 με away from the cracking location. Figure 4.11 illustrates the average strain readings of all instrumented bars (top and bottom) in the vicinity of crack at mid-span. For slab SG3 the final average strains reached to 1520 με after 112 days.

4.2.3.4 Slab SG4

Prior to cracking the average strain level remained under 100 με, but once crack formed at the mid-span, for specimen SG4 the average strain in reinforcement increased promptly to 1240 με,

while the strain away from the cracking location was still less than 300 με. Figure 4.12 illustrates the average strain readings of all instrumented bars (top and bottom) in the vicinity of crack at mid-span. The final average strains (after 112 days) were 1005 με for slab SG4. Second and third 62 days after casting causes the average reinforcement strain drops to 1000 με (strain changes =186 με). This behaviour can be attributed to higher cross-section stiffness at cracking location in the slab with higher reinforcement ratio (ρ = 1.1%) compared with slabs SG1 (ρ = 0.3 %) to SG3 (ρ = 0.7%). While additional shrinkage in slabs SG1 to SG3 increases the crack width.

4.2.3.5 Slab SS

Prior to cracking the average strain level remained under 100 με, but once crack formed at the mid-span, for specimen SS the average strain in reinforcement increased promptly to 680 με, while the strain away from the cracking location was still less than 300 με. Figure 4.13 illustrates the average strain readings of all instrumented bars (top and bottom) in the vicinity of crack at mid-span. The final average strains (after 112 days) were 410 με for slab SG4. Second and third 19 days after casting causes the average reinforcement strain drops to 580 με (strain changes =107 με). Further shrinkage and higher cross-section stiffness at cracking location due to higher modulus of elasticity of steel-reinforcement (E*s*=200 GPa) compared with the same GFRP-reinforcement ratio (EGFRP=62 GPa) causes second and third cracks occurred at 19 days of casting on both sides of the first crack.

4.2.4 Concrete Surface Strain

4.2.4.1 Slab SG1

Figure 4.14 shows the surface strains of concrete in the vicinity of the first crack. Once cracking occurred, the stiffness of slab in the vicinity of cracking reduced depending on the reinforcement

ratio and the concrete on either side of the crack shortens elastically. After cracking, the concrete surface strain in the vicinity of the first crack changed to a compressive strain (negative values in Fig. 4.14). In the specimen SG1, as the concrete shrunk the measured surface strains increased to 525 με.

4.2.4.2 Slab SG2

Once concrete surface tensile stress exceeds concrete tensile strength cracking occurred (Fig. 4.15), at this point the stiffness of slab in the vicinity of cracking reduced depending on the reinforcement ratio and the concrete on either side of the crack shortens elastically. After cracking, the concrete surface strain in the vicinity of the first crack changed to a compressive strain (negative values in Fig. 4.15). As the concrete shrunk, the measured surface strains decreased to 490 με.

4.2.4.3 Slab SG3

Figure 4.16 shows the surface strains of concrete of the slab SG3 in the vicinity of the first crack. As the concrete shrunk, the measured surface strains reached to 290 με. Once cracking occurred, the stiffness of slab in the vicinity of cracking reduced depending on the reinforcement ratio and the concrete on either side of the crack shortens elastically. For SG3 after cracking, the concrete surface strain in the vicinity of the first crack changed to a compressive strain (negative values in Fig. 4.16).

4.2.4.4 Slab SG4

The surface strains of concrete in the vicinity of the first crack for slab SG4 is shown in Fig. 4.17. In slab SG4, after cracking, the concrete surface strain in the vicinity of the first crack changed to a compressive strain (negative values in Fig. 4.17). Once cracking occurred, the

stiffness of slab in the vicinity of cracking reduced depending on the reinforcement ratio and the concrete on either side of the crack shortens elastically. In this specimen, as the concrete shrunk, the measured surface strains were 216 με after 112 days.

4.2.4.5 Slab SS

Figure 4.18 shows the surface strains of the concrete in the vicinity of the first crack. Once cracking occurred, the stiffness of slab in the vicinity of cracking reduced depending on the reinforcement ratio and the concrete on either side of the crack shortens elastically. In the slab SS after cracking, the concrete surface strain in the vicinity of the first crack changed to a compressive strain (negative values in Fig. 4.18). In the slab SS, as the concrete shrunk, the measured internal tensile strains increased to 215 με.

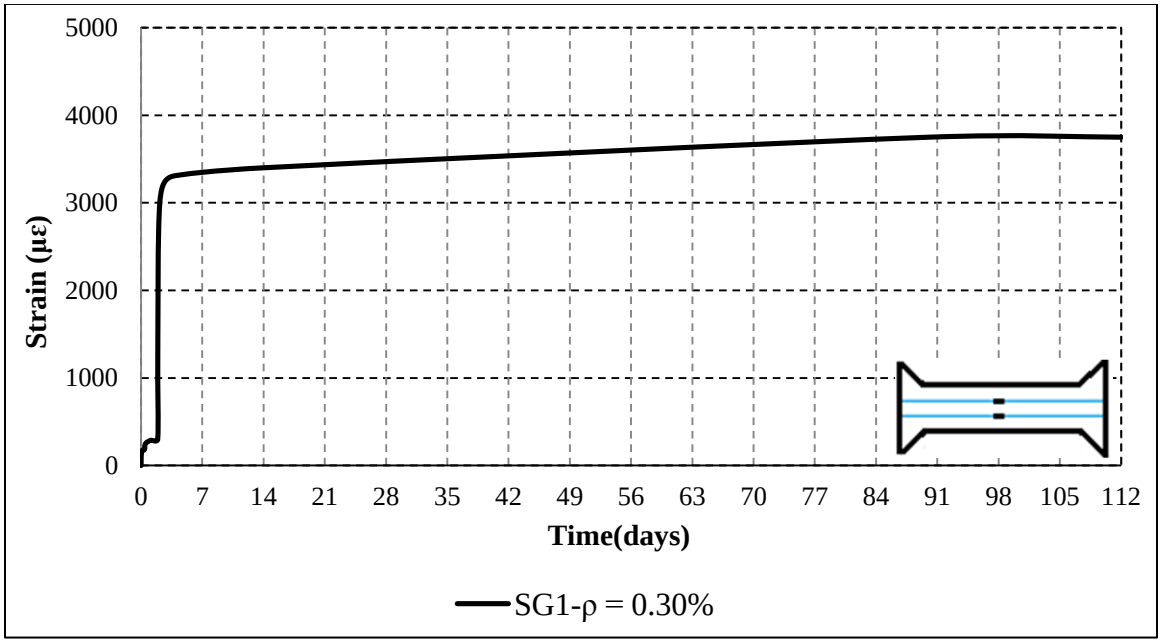

Fig. 4.9: Average reinforcement strain (Top and Bot.) at cracking (slab SG1).

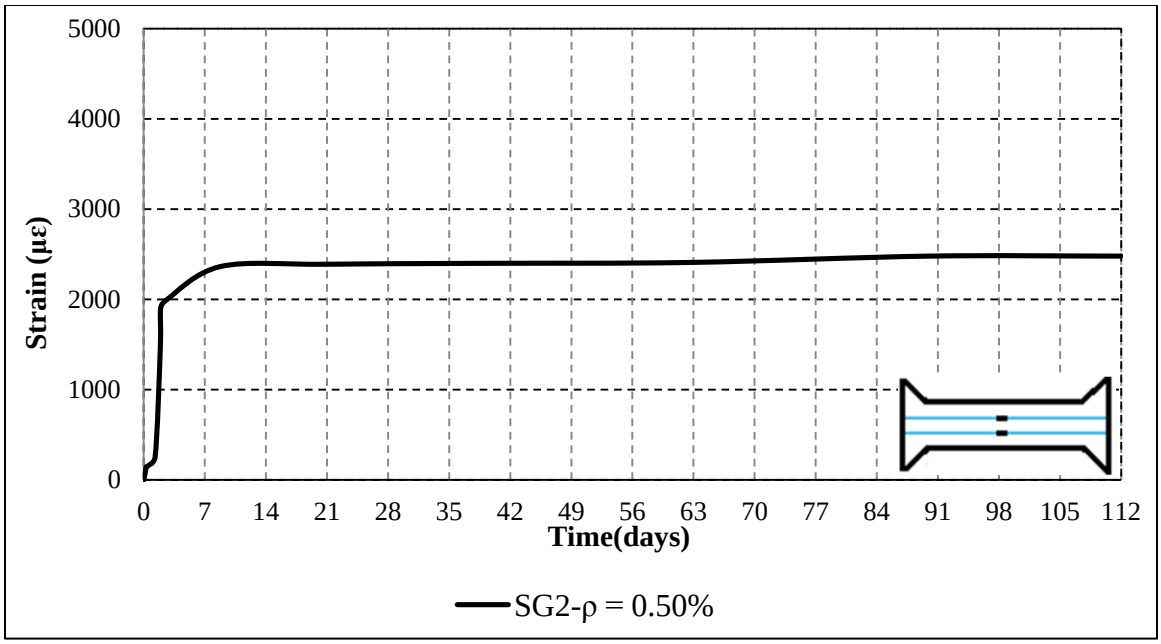

Fig. 4.10: Average reinforcement strain (Top and Bot.) at cracking (slab SG2).

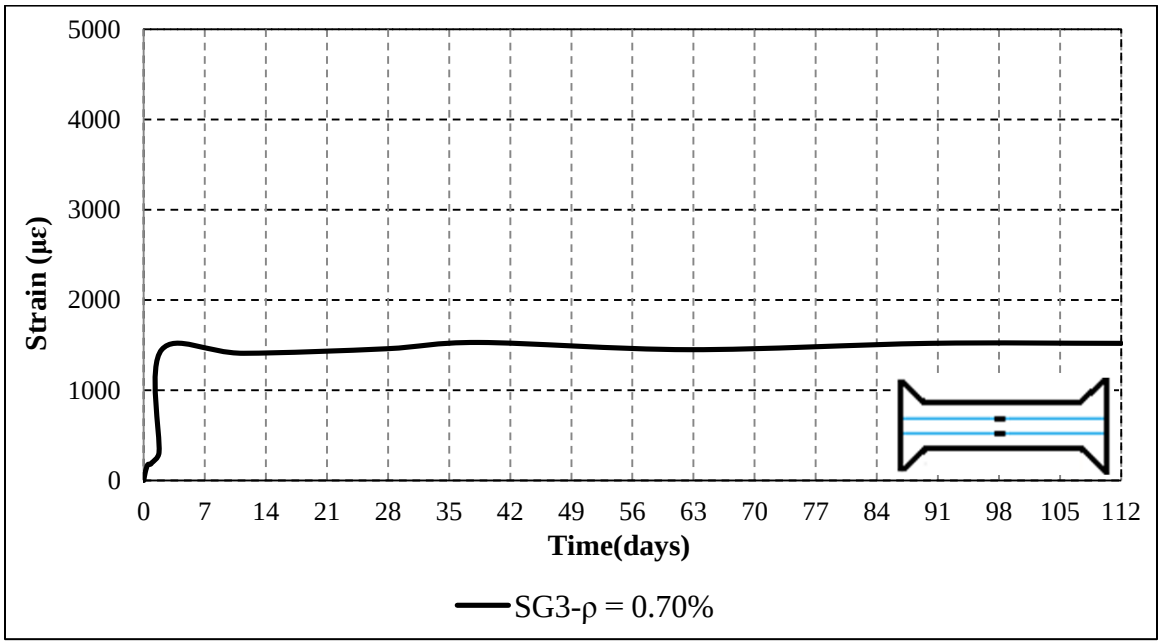

Fig. 4.11: Average reinforcement strain (Top and Bot.) at cracking (slab SG3).

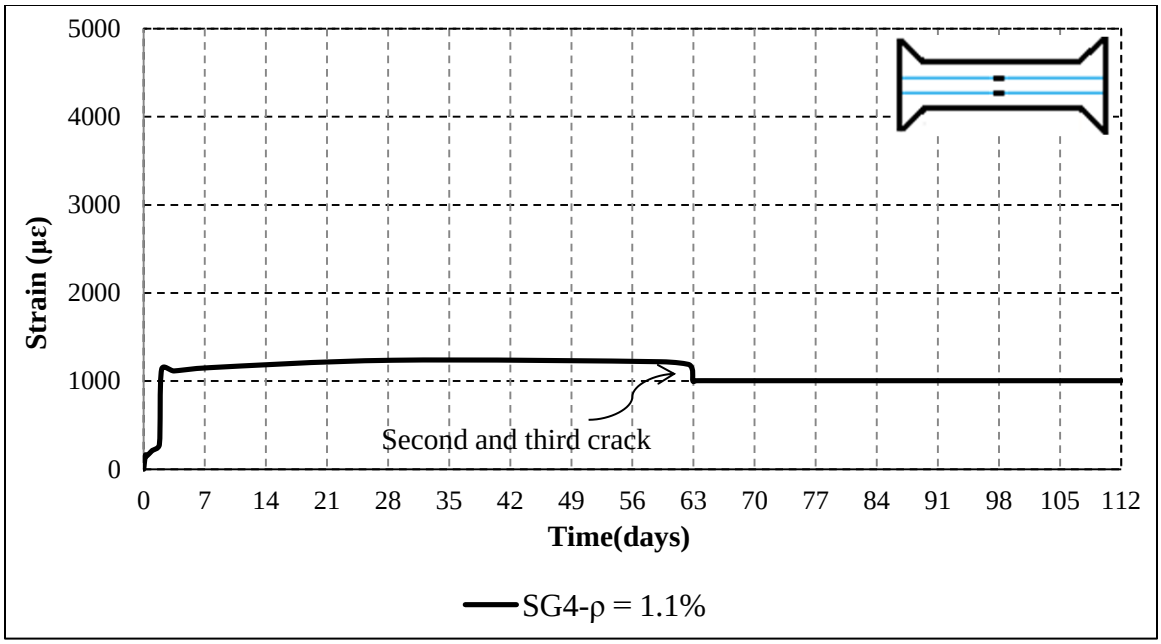

Fig. 4.12: Average reinforcement strain (Top and Bot.) at cracking (slab SG4).

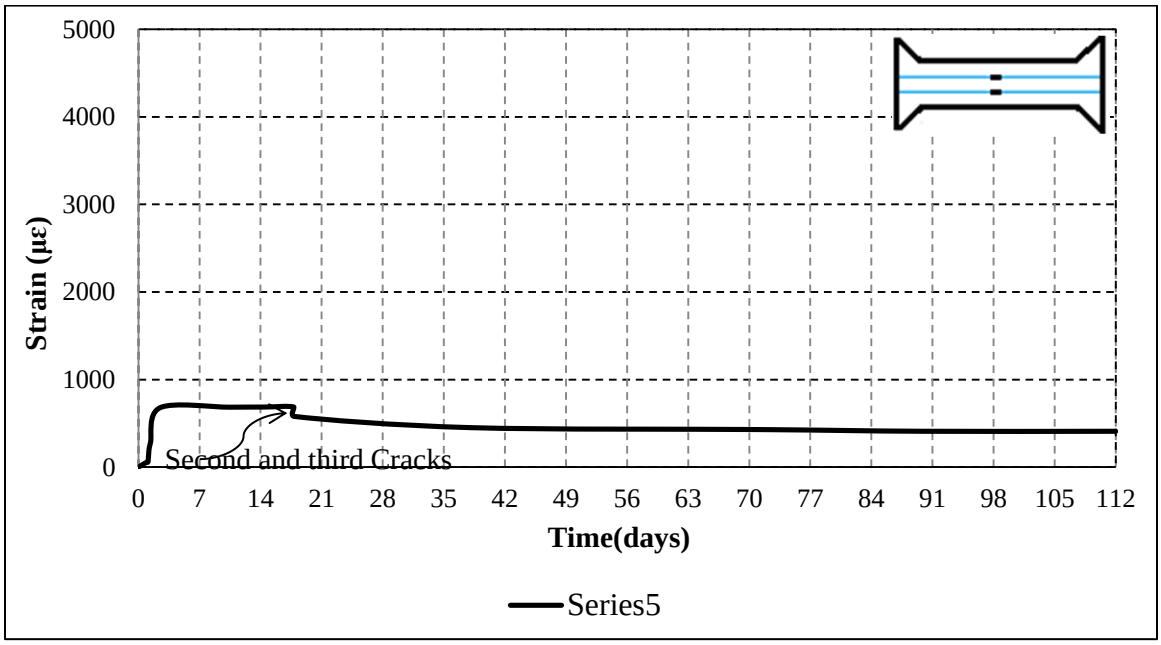

Fig. 4.13: Average reinforcement strain (Top and Bot.) at cracking (slab SS).

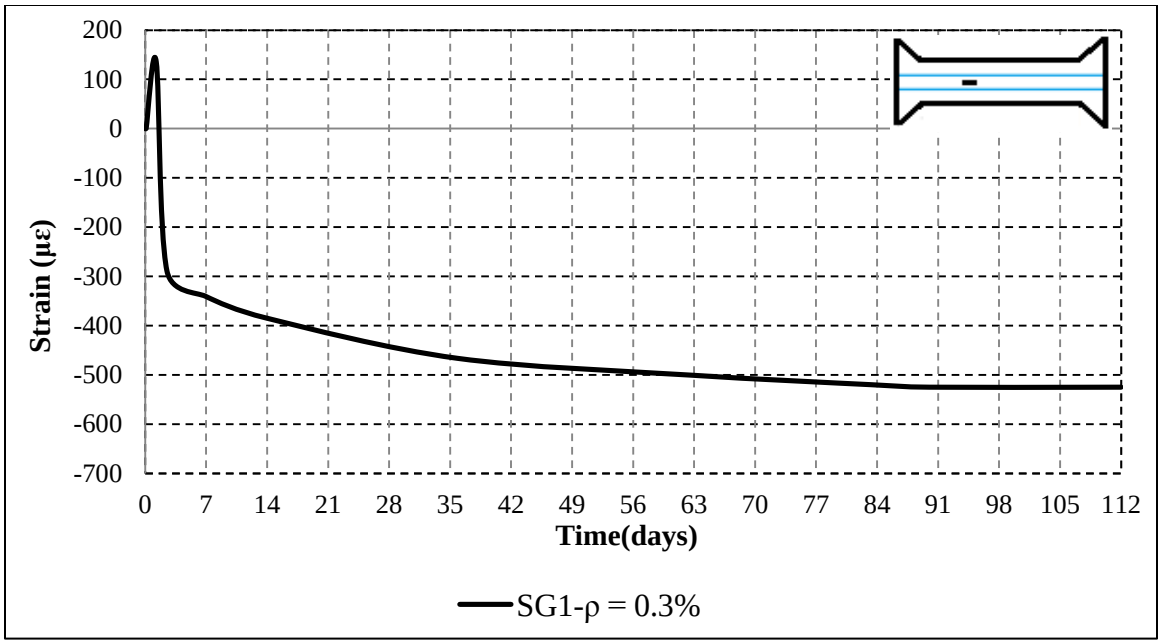

Fig. 4.14: Surface strains of concrete in the vicinity of the first crack (SG1).

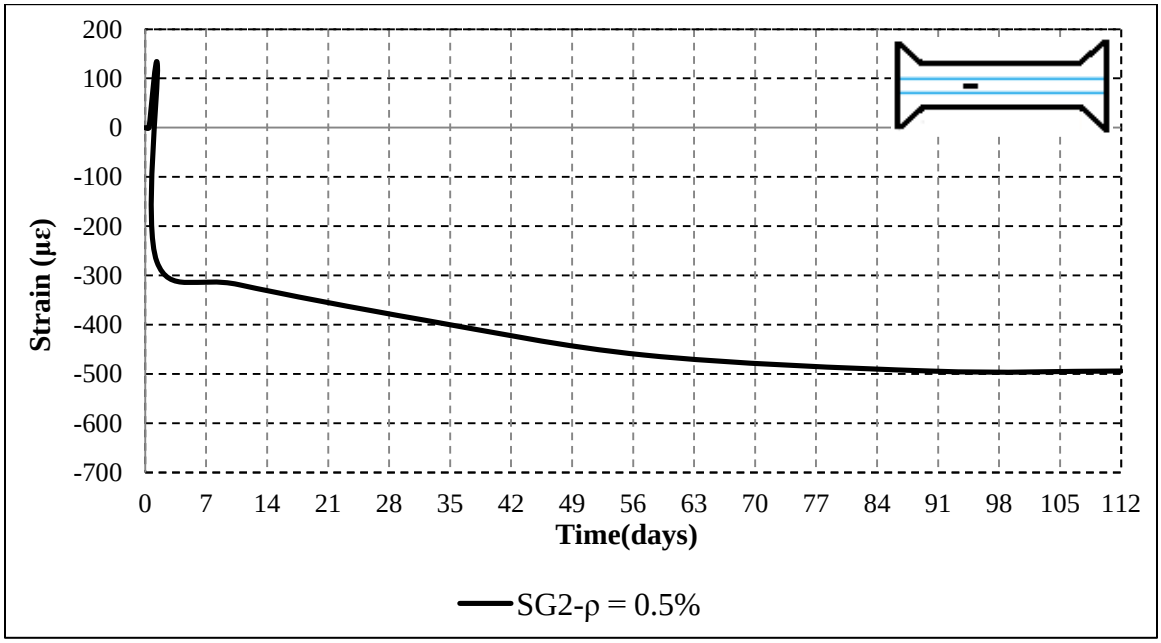

Fig. 4.15: Surface strains of concrete in the vicinity of the first crack (SG2).

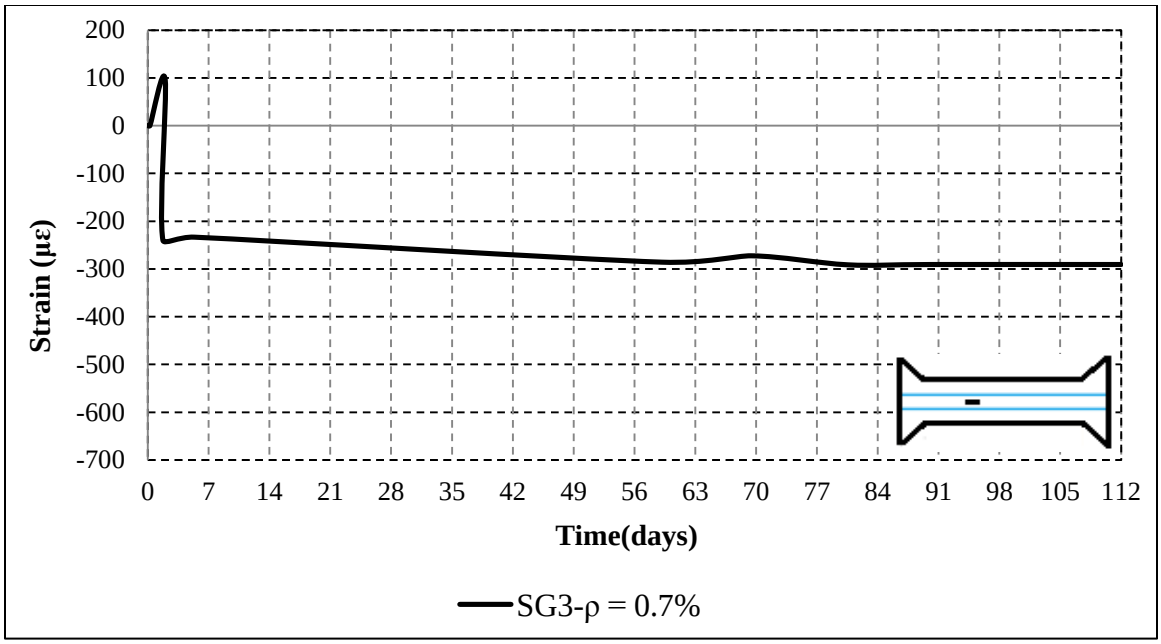

Fig. 4.16: Surface strains of concrete in the vicinity of the first crack (slab SG3).

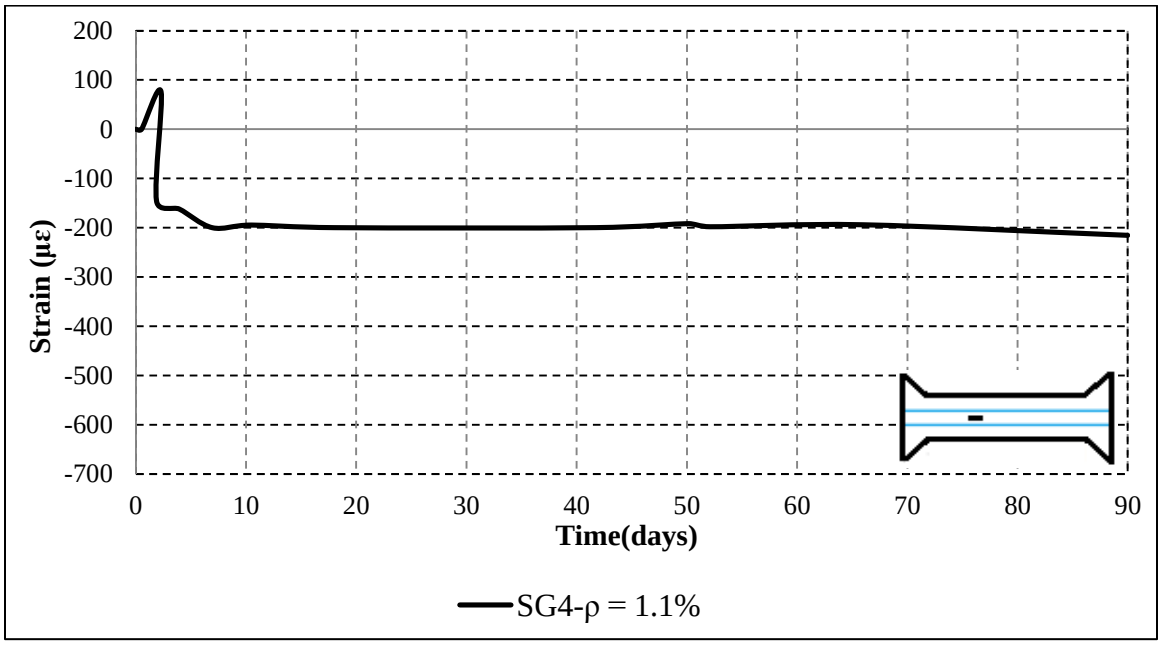

Fig. 4.17: Surface strains of concrete in the vicinity of the first crack (slab SG4).

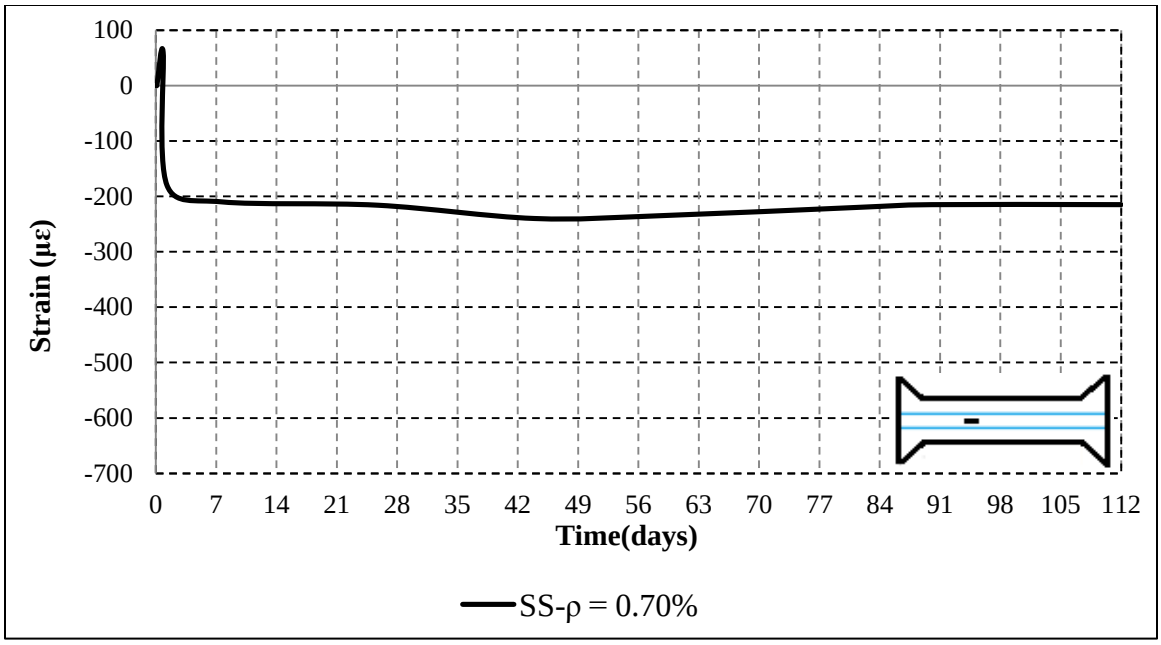

Fig. 4.18: Surface strains of concrete in the vicinity of the first crack (slab SS).

4.3 DISCUSSION OF SLABS UNDER NORMAL LABORATORY CONDITIONS

4.3.1 Crack Characteristics

Primarily, the width of a crack in a restrained slab varied depending on the bonded reinforcement ratio crossing the crack. Although, the magnitude of crack width depends on several factors such as degree of restraint, quality of bond between concrete and reinforcement, size and distribution of bars and the concrete quality; the only variable in this study was the bar size (reinforcement ratio). For slab SG1 ($\rho = 0.3\%$) and SG2 ($\rho = 0.5\%$) the crack width reached the allowable value of 0.5 mm (ACI 440 2006, CSA 2006) after 40 and 42 hours, respectively (Fig. 4.19). These crack widths grew to 0.73 and 0.64 mm after 112 days, respectively. For slabs SG3 ($\rho = 0.7\%$), SG4 ($\rho = 1.1\%$), and S (RC with steel $\rho = 0.7\%$) the final crack width were 0.33, 0.24, and 0.18 mm, respectively, after 112 days of exposure to laboratory conditions. Generally, an increase in the GFRP reinforcement ratio caused reduction of crack width and average crack spacing. Also

the final crack width in the slab SG1 was 0.33 mm, while in the specimen with the similar reinforcement ratio of steel (SS) final crack width reached to 0.18 mm after 112 days of exposure to normal laboratory conditions. It was expected due to lower section stiffness of the GFRP-RC slab compare to the steel-RC slab. As the reinforcement ratio and modulus of elasticity increased from 0.3% to 1.1%, and 62 GPa to 200 GPa respectively, the average crack spacing reduced from 2500 mm to 625 mm. In the specimens SG1, SG2, SG3, reinforced with equals or lower than minimum reinforcement ratio recommended by CHBDC, the crack spacing was 2500 *mm* while in the in Slab SG4, and SS the second and third crack occurred after 63 and 19 days of casting, respectively on both sides of the first crack, resulting in a reduced crack spacing of 625 mm. An increase in the GFRP reinforcement area or reinforcement modulus of elasticity leads to less stiffness reduction at first cracking (at mid-span), thus the restraining force after cracking remains high. With a high restraining force, due to future drying shrinkage or any environmental temperature variation, the concrete in regions away from the first crack tends to experience further cracking.

Prior to cracking the average strain level in the reinforcement in the vicinity of the crack remained under 100 με, but once crack formed at the mid-span, for specimens SG1, SG2, SG3, SG4, and SS the average strain in reinforcement increased promptly to 3000, 1900, 1450, 1130, and 685 με, respectively, while the strain away from the cracking location was still less than 300 με.

The average strain decreased with increasing the reinforcement ratio or modulus of elasticity. The final average strains (after 112 days) were 3750, 2480, 1520, 1005, and 410 με for SG1, SG2, SG3, SG4, and SS, respectively (Fig. 4.19). After the first cracking in specimens with higher reinforcement ratios or higher modulus of elasticity, subsequent shrinkage caused further

gradual increases in the restraining force, and hence in the concrete stress away from the crack. In slab SG4 (reinforced with the highest reinforcement ratio), and SS (reinforced with steel reinforcement) second and third cracks were developed 62, and 19 days respectively, after casting. Comparatively, in the specimens reinforced with the minimum or lower GFRP reinforcement ratios, additional shrinkage only increased the crack width without forming new cracks. This is because the concrete was no longer fully restrained, due to the lower stiffness of the slab at the first crack.

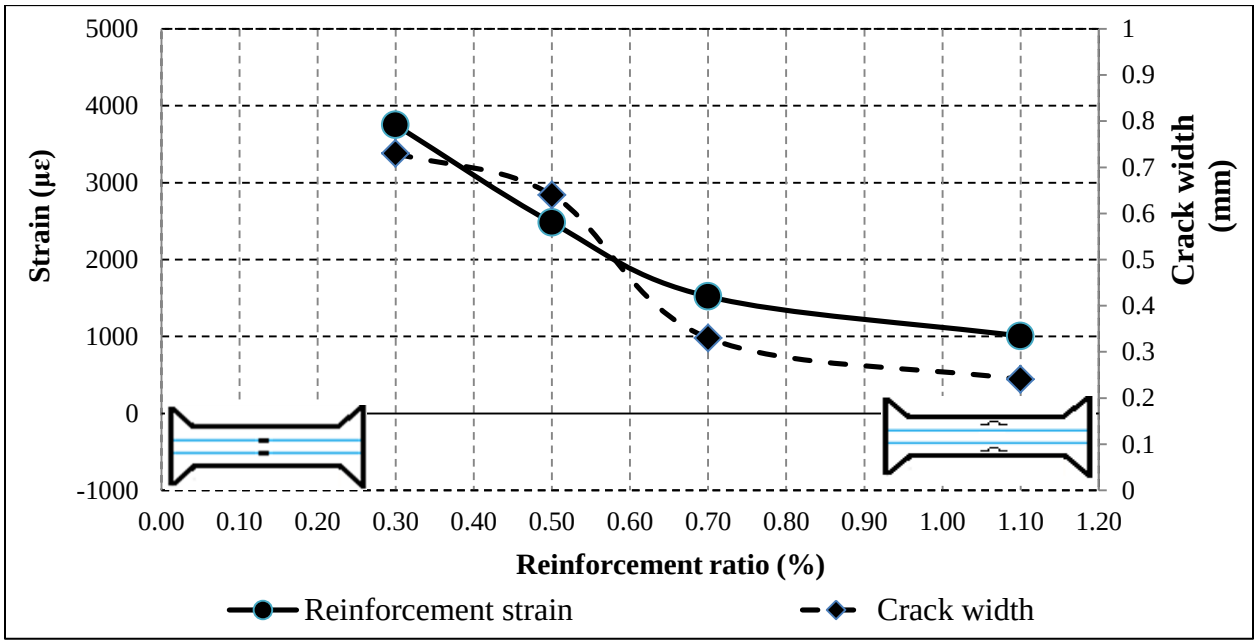

Fig. 4.19: The final crack width and average reinforcement strain (Top and Bot.) at cracking location.

4.3.2 Strains in Concrete

The test results indicate that the deformation of concrete decreased with increasing the reinforcement ratio. In specimens SG1, SG2, SG3, SG4 and SS as the concrete shrunk, the measured internal tensile strains 135, 126, 96, 76 and 60 με, respectively. Internal strains of concrete were higher since the gauges were located at the mid-span (notched section under the

maximum tensile stress); while surface strains showed lower value as the gauges were placed away from the mid-span location, where the tensile stress is reduced. With increasing the reinforcement ratio from 0.3 to 1.1%, the internal and surface strain of concrete reduced by approximately 74 and 53%, respectively. For SG1, SG2, SG3, SG4 and SS after cracking, the concrete surface strain in the vicinity of the first crack changed to a compressive strain (negative values in Fig. 4.14 to 4.18). Once cracking occurred, the stiffness of slab in the vicinity of cracking reduced depending on the reinforcement ratio and the concrete on either side of the crack shortens elastically.

4.4 THEORETICAL VS. EXPERIMENTAL RESULTS

Limited studies provided formulas to predict cracking characteristics of RC deck slabs and stress distribution in bars at cracking locations due to restrained shrinkage. In this section, the experimental results from this study are compared to predictions from a theoretical model for steel-RC restrained members that are not subjected to significant bending (Gilbert 1992). In his theoretical analysis, Gilbert (1992) explained that shrinkage causes an axial force built-up (Eq. 1) in restrained members, which leads to direct tension cracks. He proposed Eqs. 4.2 and 4.3 to calculate the stress in the bars, in the vicinity of the crack, and the crack width, respectively. In this model, the restraint is provided to the longitudinal movement caused by shrinkage and temperature changes. The results indicate that as these equations were developed for steel-reinforced members, modification factors would be needed for the equations to be applicable to FRP-reinforced slabs. Table 4.1 illustrates input values for parameters using in equations 4.1 to 4.3.

$$N(\infty) = \frac{-3A_s n^* E_s \Delta u}{2s_0 m} - \frac{(3L-2s_0 m)n^* A_s}{2s_0 m}(\sigma_{av} + \varepsilon^*{}_{sh} E^*{}_e) \quad \textbf{[Eq. 4.1]}$$

$$\sigma^*{}_{s2} = \frac{N(\infty)}{A_s} \quad \textbf{[Eq. 4.2]}$$

$$w = -[\frac{\sigma^*{}_{c1}}{E^*{}_e}\left(s - \frac{2}{3}S_0\right) + \varepsilon^*{}_{sh} S] \quad \textbf{[Eq. 4.3]}$$

where $N(\infty)$, A_s, E_S, Δu, S_0, m, σ_{av}, $\varepsilon^*{}_{sh}$ and $E^*{}_e$ are final restraining tensile force, reinforcement bar area (mm^2), modulus of elasticity of re-bars (MPa), support displacement (mm), correction factor, concrete average stress (MPa), final shrinkage and effective concrete modulus of elasticity (MPa), respectively. Also, $\sigma^*{}_{s2}$, w, $\sigma^*{}_{c1}$ and S are final reinforcement stress (MPa), crack width (mm), concrete final stress (MPa) and crack spacing (mm), respectively.

Table 4.1: Input data for parameters used in equations 4.1 to 4.3

Slab	$\mathbf{A_{GFRP}}$ **(mm^2)**	$\mathbf{d_b}$ **(mm)**	$\boldsymbol{\varepsilon^*_{sh}}$	$\mathbf{E_{GFRP}}$ **(MPa)**	$\mathbf{F_{t\,(GFRP)}}$ **(MPa)**	$\boldsymbol{\Delta_u}$ **(mm)**
SG1	284	9.5	-3.09e-4	65351	1572	0.031
SG2	508	12.7	-3.09e-4	65607	1759	0.035
SG3	764	15.9	-3.09e-4	62297	1725	0.037
SG4	1140	19.1	-3.09e-4	63374	1484	0.04

l = 2500 mm, t = 180 mm, ϕ^* = 0.6, $f_{t\,(7)}$ = 3.4 MPa, $f_{c(3)}$ = 25, $f_{c(28)}$ = 38 MPa, $E_{c(3)}$ = 20200 MPa, $E_{c(28)}$ = 21800 MPa

Considering the fully restrained member in direct tension as the concrete shrinks, the restraining force gradually increases until the first crack occurs, which is usually within two days from the commencement of drying. Immediately after the first cracking, the restraining force reduces and the concrete stress away from the crack is less than the tensile strength of the concrete. The

concrete on either side of the crack shortens elastically and the crack opens to a width w. At the crack location, the reinforcement carries the entire force. In the region immediately adjacent to the crack the concrete and the reinforcement stresses vary considerably, and a region of partial bond breakdown exists. At a distance S_o from the crack, which was earlier proposed by Favre et al. (1983) for a member containing deformed bars or welded wire mesh (Eq. 4.1), the concrete and the reinforcement stresses are no longer influenced directly by the presence of the crack. It was suggested that the value of s_o to be multiplied by 1.33 to achieve better predictions for RC member with steel bars (Gilbert 1992). In this study, a coefficient of 1.33 for s_o led to significant discrepancy between the model's predictions and experimental data. Hence, the coefficient value was varied from 0.1 to 1.6 in 0.1 increments until a reasonable agreement (relatively smaller error) was observed between the two data sets; this was obtained at a coefficient of 0.7. The equation used to calculate the error is given by:

$$e = \frac{experimental\ value - theoretical\ value}{experimental\ value} \qquad \textbf{[Eq. 4.4]}$$

Figure 4.20 shows a comparison between the maximum calculated final crack width (obtained using the analytical model developed by Gilbert 1992) and the maximum average of those observed in the laboratory. The measured width of shrinkage cracks, agrees with the results of the analytical model with an error of approximately 6.8%.

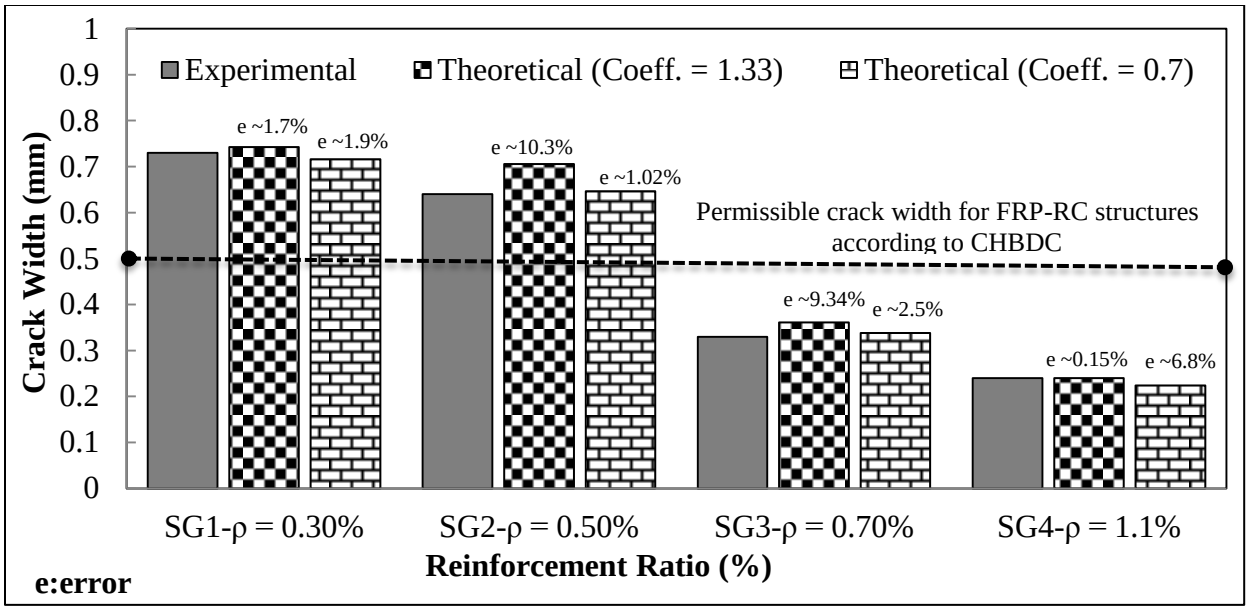

Fig. 4.20: Experimental and theoretical results for the final crack width**.**

Comparisons between the theoretical and experimental results for the final stress in the GFRP bars in the vicinity of cracking are presented in Fig. 4.21. Except for slab SG1, the measured stress, agree with the results of the analytical model with a 10% error. The discrepancy between theoretical and experimental results of SG1 for stress value on the GFRP bars was due to the effect of small GFRP bar diameter on the bond-slip relationship between reinforcement and the surrounding concrete at cracking location.

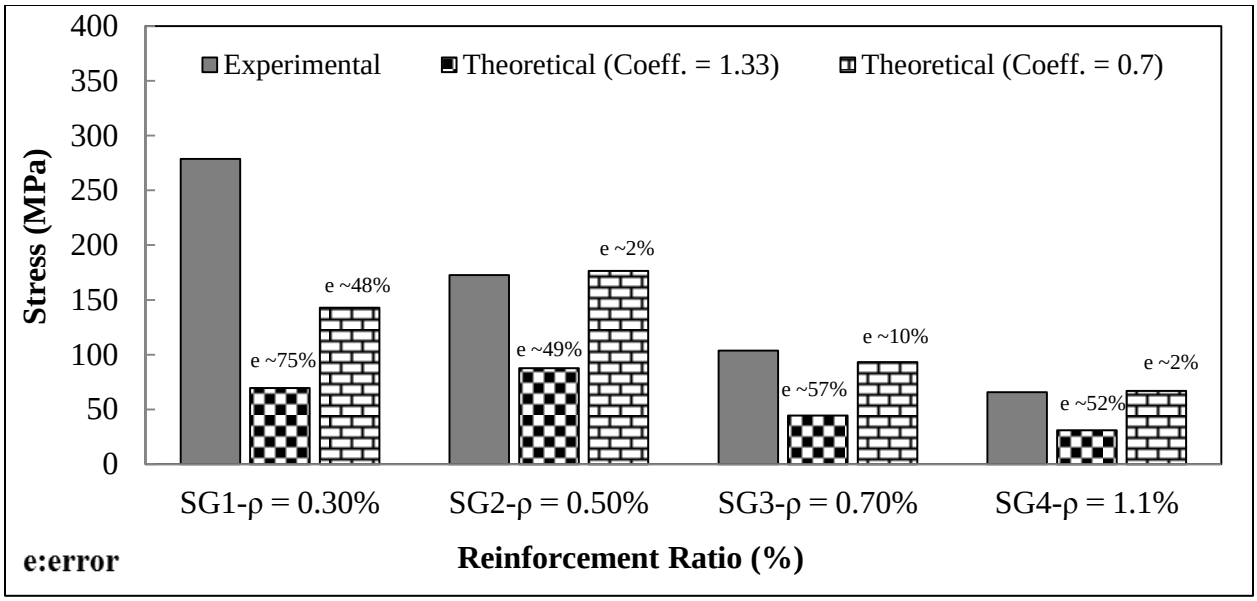

Fig. 4.21: Final experimental and theoretical results for the final stresses in GFRP bars at cracking.

CHAPTER 5: RESULTS AND DISCUSSIO - EFFECT OF ENVIRONMENTAL CONDITIONS

5.1 GENERAL

The current chapter reports the test results and the observations of Series (II) including two specimens subjected to harsh environmental conditions. The objective of the second series was to evaluate the effect of freeze-thaw and wet-dry cycling on the development of early-age cracking on the G-FT and G-WD bridge deck slabs reinforced with GFRP reinforcement. The two specimens of this series are reinforced with the minimum-acceptable reinforcement ratio as obtained by first series. All specimens are properly instrumented to monitor strains, humidity, and temperature history. The performance of the specimens is assessed and discussed in terms of concrete weight loss, cracking pattern, width, and spacing, and strains in the reinforcement and concrete. The experimental results were compared with provisions of the CHBDC (CSA 2006).

5.2 GENERAL OBSERVATIONS

The width of cracks in the restrained slabs varied according to the environmental exposure and different reinforcement material. While the magnitude of crack width depends on several factors such as degree of restraint, quality of bond between concrete and reinforcement, size and distribution of bars, concrete quality and ambient conditions, the studied variables in this study were the effect of different environmental conditions on the slabs reinforced with minimum-acceptable reinforcement ratio subjected to shrinkage (as obtained by series (I)). For each slab, the crack width was considered as the average of the measured value at two locations across the slab width at mid-span. Generally, the first crack in all specimens was observed within the first

three days after casting in the transverse direction before exposure. Figure 5.1 shows the cracking pattern for all the slabs at the notched (mid-span) location. The cracks, which usually extended into the full depth of slabs, typically occurred at mid-span (notched location). For the RC slabs, the bar strain was presented as average strain readings of all instrumented bars (top and bottom) in the vicinity of crack at mid-span. Prior to cracking the average strain level remained under 300 με. The top and bottom GFRP reinforcement carried the full restraining force at each crack, while the stress in the concrete was zero (Fig. 5.2). Once the crack formed at the mid-span, the strains increased significantly. The internal concrete strain at cracking location was considered the embedment concrete strain gauge reading before cracking, while due to damage of the internal gauge at cracking time the surface concrete strain was presented using surface strain gauge 270 mm away from the cracking location. Figures 5.2 shows the internal strain of the concrete at cracking, once the early age cracks became visible for specimens G-FT and GWD the measured concrete internal tensile strains were 276 and 310 με, respectively. For all specimens after cracking, the concrete surface strain in the vicinity of the first crack changed to a compressive strain. Once cracking occurred, the stiffness of slab in the vicinity of cracking reduced depending on the reinforcement ratio and modulus of elasticity on either side of the crack shortens elastically.

5.3 FREEZE-THAW EXPOSURE

The behavior of restrained concrete elements under freezing-thawing conditions is affected by multiple variables (e.g. internal water expansion, and material contraction due to low temperature). It is well documented that if concrete elements are critically saturated (internal RH > 90%), the water volume expansion phenomenon in larger capillary pores induces considerable volume changes of concrete during freezing. At the onset of ice crystallization, the frictional

resistance to ice growth creates internal pressure in the pores leading to concrete expansion (Scherer et al. 2002). In addition, ice formation in the void space imbibes water from the smaller (gel) pores, creating negative (suction) pressure in the matrix and thus contraction (Towers and Helmuth 2008). Hence, the total volume change of concrete is a combination of expansion and contraction from hydraulic and osmotic pressures (Fig. 5.3).

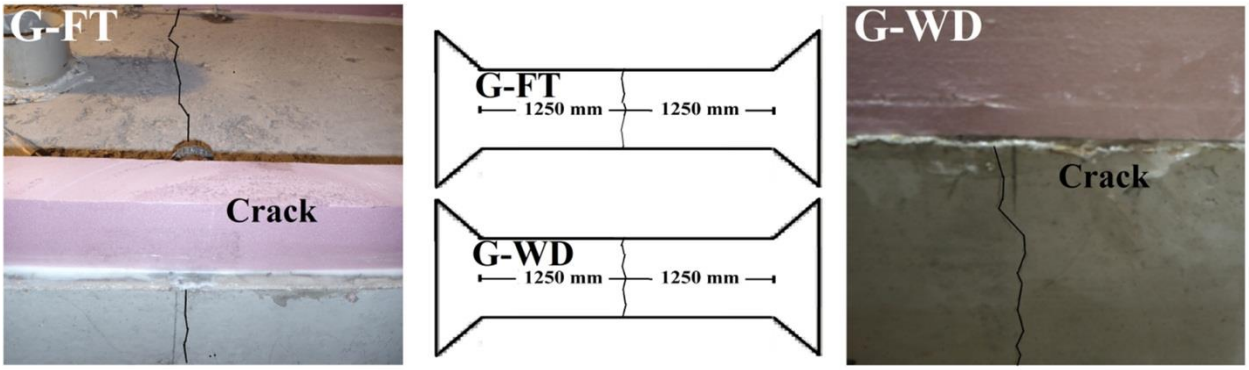

Fig. 5.1: Final crack pattern in slabs G-FT and G-WD.

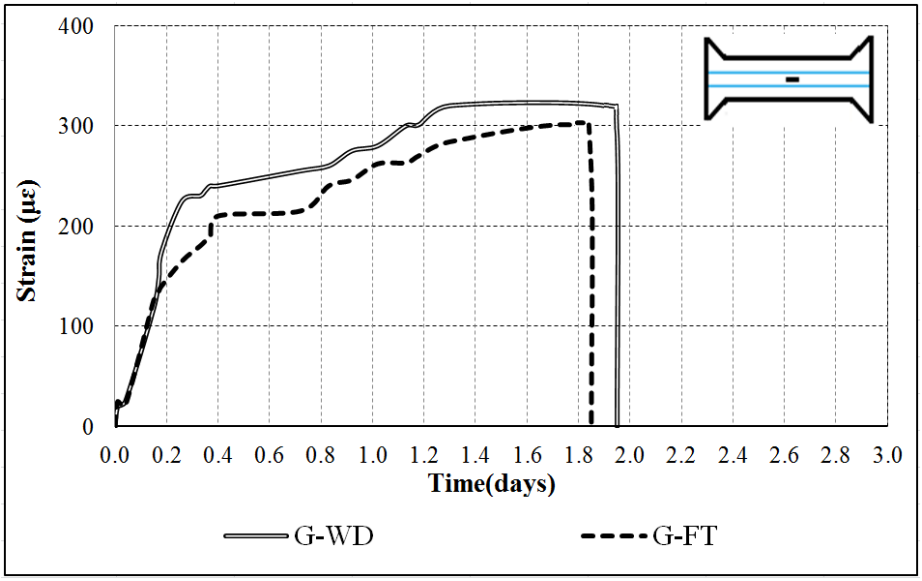

Fig. 5.2: Internal strain of concrete at cracking at cracking time.

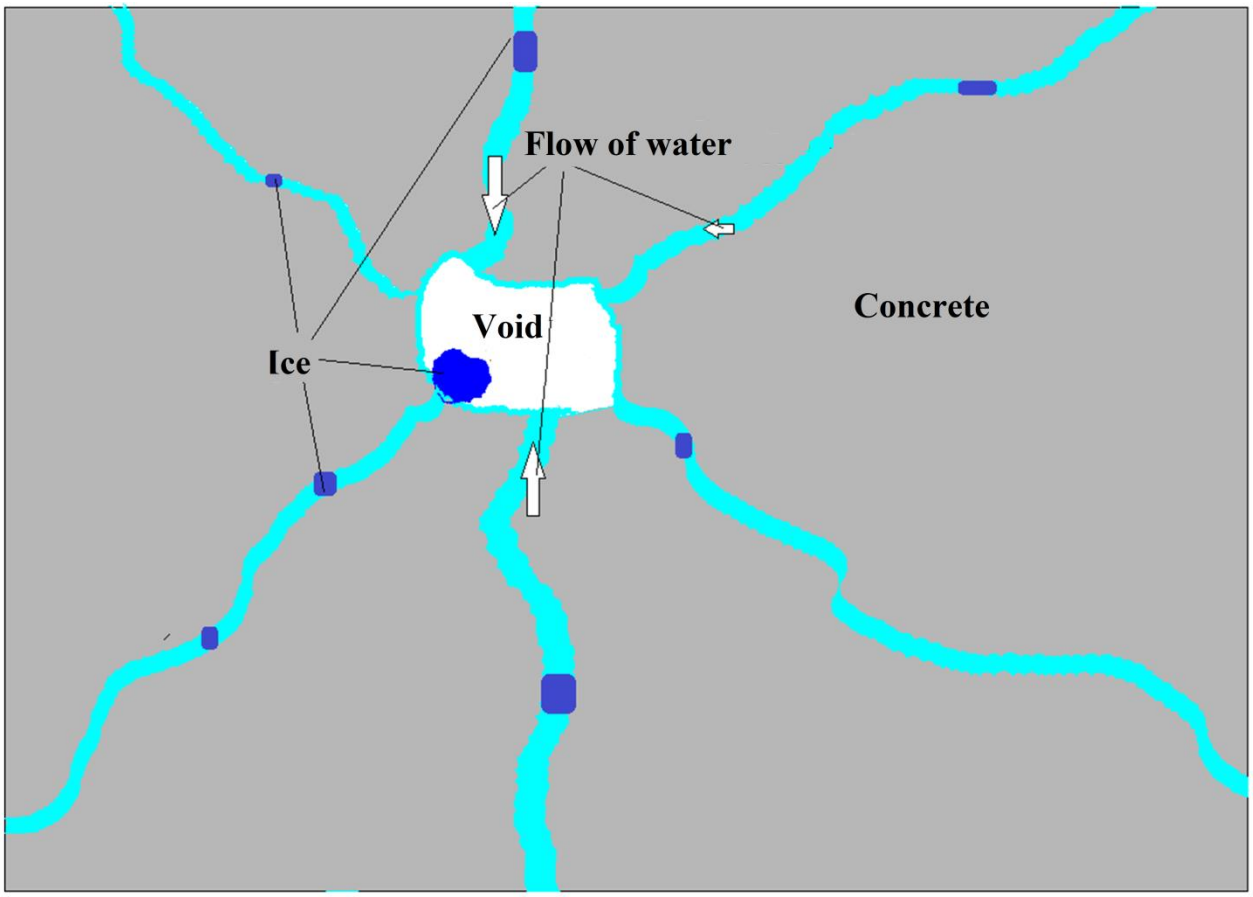

Fig. 5.3: Schematic of approximations of pore geometry in concrete.

The transverse full-depth crack occurred for slab G-FT within 47 hours (before exposure) at the mid-length (notched section). Figure 5.4 shows the change in crack width in this slab over 163 freezing-thawing cycles (112 days).

Crack width reached to its maximum and minimum point at +4 °C (thawing) and -18 °C (freezing), respectively, in each cycle. At the last cycle (163), the crack width varied between 0.29 and 0.42 mm corresponding to the freezing-thawing stages, respectively (Fig. 5.5). The lower crack width recorded during freezing periods can be attributed to the volumetric expansion of the critically saturated slab, which led to partial closure of the crack opening. Upon relieving the expansion pressure during thawing periods, the crack width increased up to 0.42 mm (in the

last cycle), which is 40 and 27% higher than the crack width measured before the freezing-thawing exposure and in the normal exposure (slab SG3), respectively.

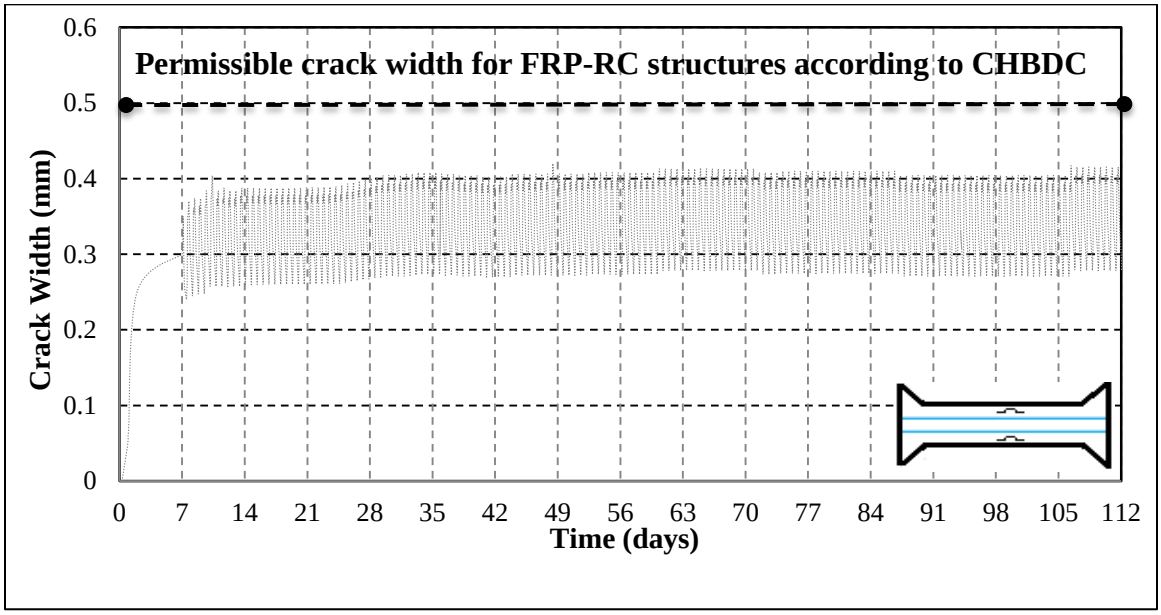

Fig. 5.4: Crack width development in the specimen under freeze-thaw conditions.

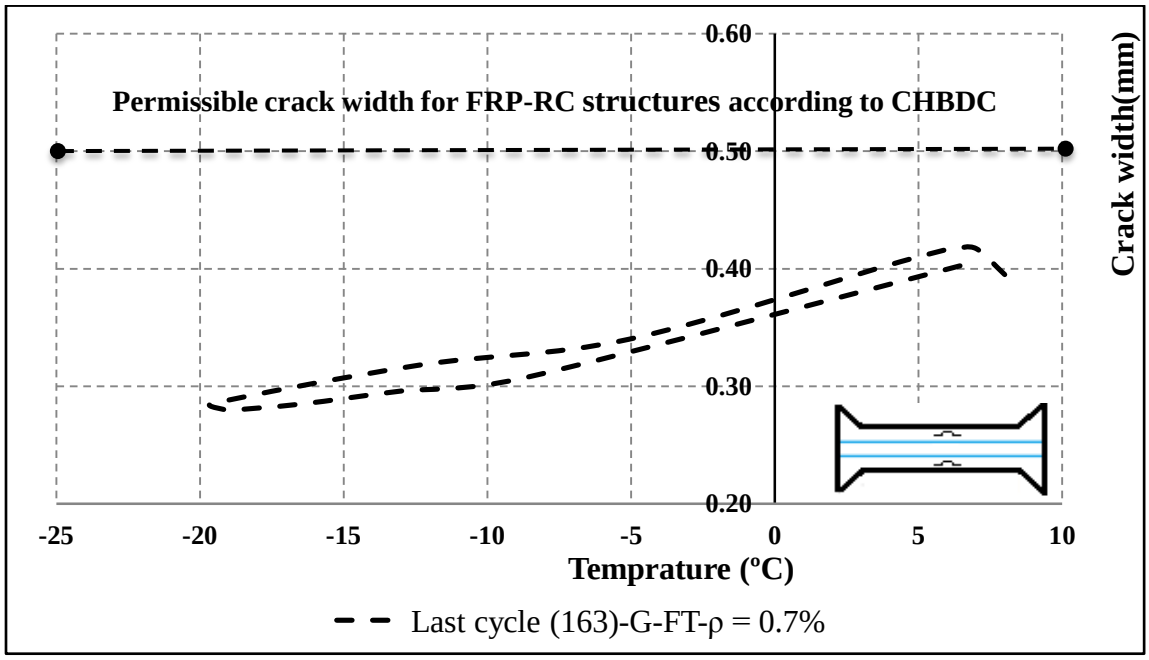

Fig. 5.5: Crack width development in the slab G-FT under freeze-thaw conditions during the last cycle.

For slab G-FT, Fig. 5.6 shows the average fluctuation of the strains in the reinforcement at cracking after 163 freezing-thawing cycles. In the last cycle, the strains of the reinforcement at the cracking location were 1020 and 1690 με during the freezing-thawing stages, respectively (Fig. 5.7). Complying with the crack width results, this trend is attributed to the repetitive volumetric change associated with frost action as discussed earlier.

Also, it was observed that slab G-FT suffered from moderate surface scaling (Fig.5.8). Figure 5.9 indicates surface scaling less than 0.5 kg/m^2 at the end of exposure (BNQ 2002), which is a typical damage manifestation of concrete exposed to freezing-thawing cycles. This trend might be ascribed to over finishing the surface of slab G-FT, which led to reducing the volume of air entrainment in the surface as shown by the Scanning Electron Microscopy (SEM) analysis.

5.4 WETTING AND DRYING EXPOSURE

Wetting-drying conditions may significantly affect RC elements due to the variation of moisture distribution with depth and accelerated shrinkage during drying periods. For slab G-WD, the relative humidity of the concrete surface markedly changed during wetting-drying cycles relative to the inner core, which led to further deformations. Figure 5.10 shows the change in crack width for slab G-WD which was subjected to 5 wetting-drying cycles over 112 days. In the last cycle (22 °C with 100% RH and 35 °C with 30% RH) the crack width varied between 0.23 and 0.46 mm. The lower crack width recorded during the wetting periods can be attributed to swelling of the slab due to the increase in relative humidity, which led to partial closure of the crack opening. Subsequently, excessive drying of the slab increased the crack width up to 0.46 mm (in the last cycle), which is 0.92% and 0.39% higher than that crack width measured before the wetting and drying exposure and in the normal exposure (slab SG3 after exposure for 112 days), respectively.

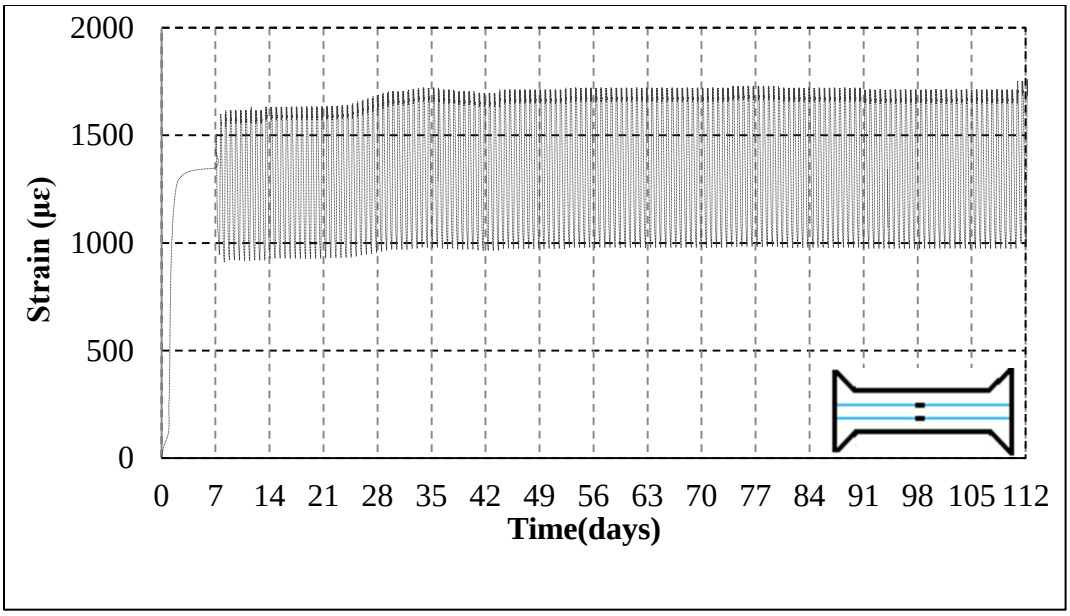

Fig. 5.6: Development of the bar strains in the slab G-FT under freeze-thaw conditions.

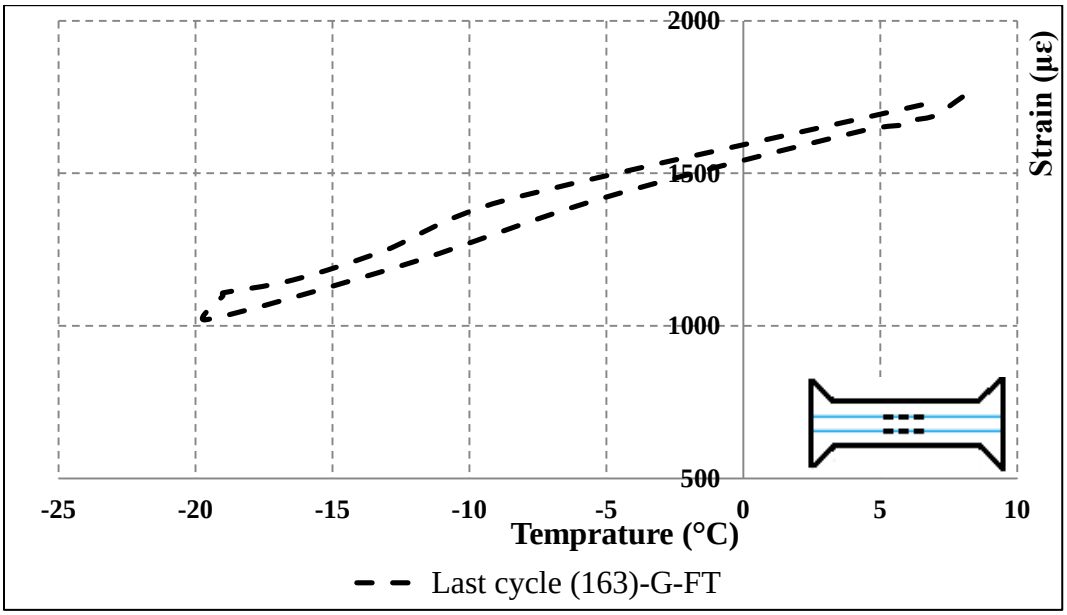

Fig. 5.7: Development of the bar strains in the slab G-FT under freeze-thaw conditions during the last cycles.

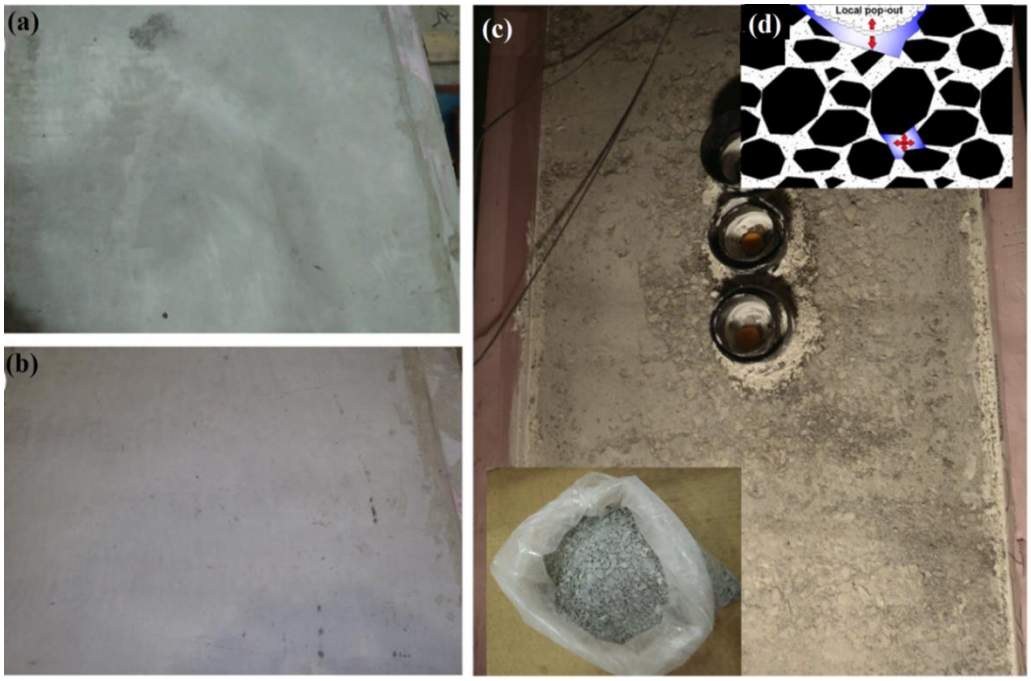

Fig. 5.8: Concrete surface appearance in different environmental conditions: (a) wet-dry, (b) normal, and (c) freeze-thaw, and (d) Surface scaling mechanism.

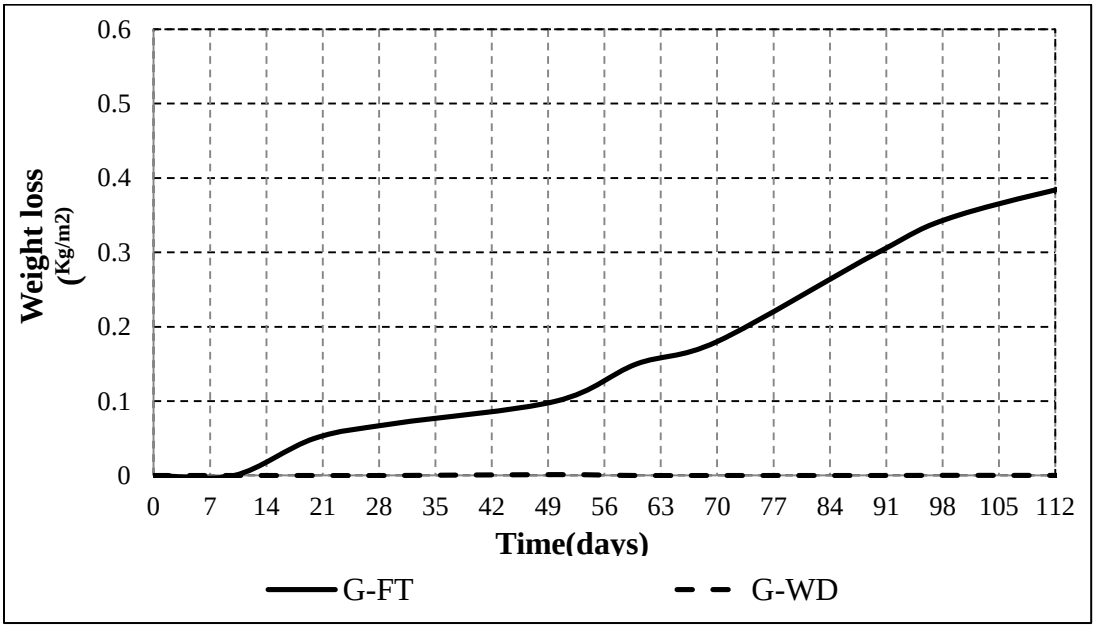

Fig. 5.9: Surface scaling.

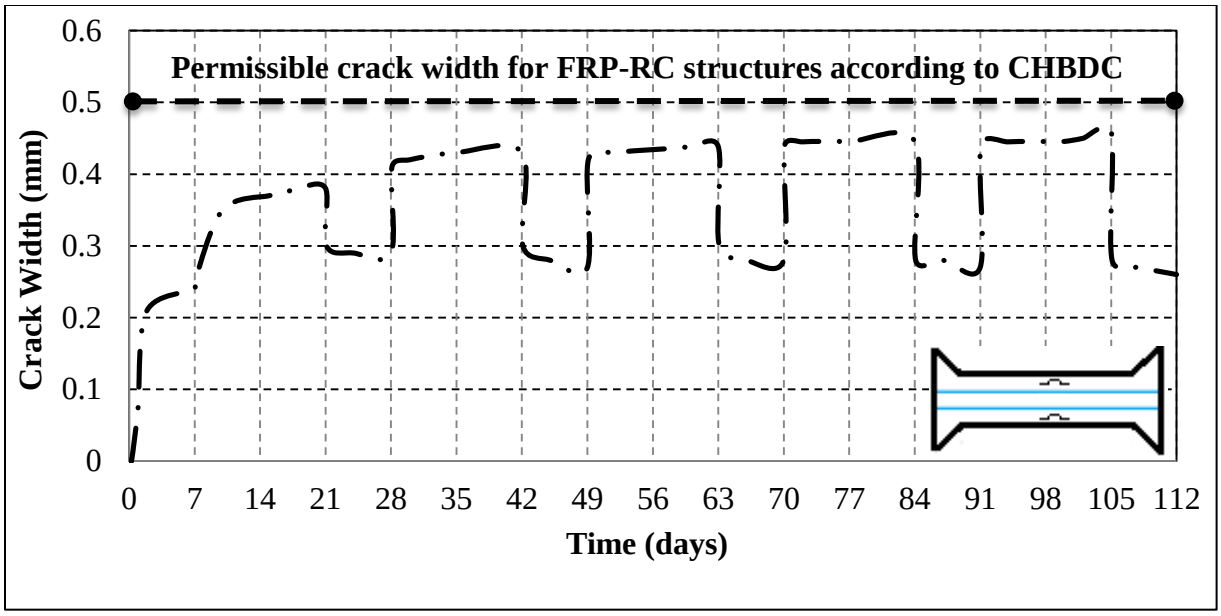

Fig. 5.10: Crack width development in the slab G-WD under wet-dry conditions.

Corresponding to the crack width trend, the strain in the GFRP bars increased from 1400 με (wetting portion) to 2250 με (drying portion) in the last cycle (Fig. 5.11), due to the additional drying shrinkage deformation under hot-arid conditions, which was restrained by the GFRP reinforcement. It should be noted that this value is significantly higher than the maximum strains recorded in the normal (1520 με) and freezing-thawing (1690 με) exposures. This behavior was confirmatory to the measurements of concrete surface strain that increased up to 480 με due to the additional shrinkage during the drying portion (Fig. 5.12).

5.5 MATERIALS TESTS

In additional to the early-age cracking of restrained concrete slabs exposed to harsh conditions, they were vulnerable to material degradation especially at the mid-length (in the vicinity of the crack) due to temperature and humidity variations. To capture this trend, three materials tests Dynamic Modulus of Elasticity (DME), Rapid Chloride Permeability Test (RCPT), and

Scanning Electron Microscopy (SEM) were conducted on eight cores (close and away from left and right sides of the crack) extracted from slabs G-WD and G-FT; four cores each.

5.5.1 UPV Test (Ultrasonic Pulse Velocity Test)

Table 5.1 shows the dynamic modulus of elasticity results for the concrete used before (unexposed specimens) and after (cores) being subjected to freezing-thawing and wetting-drying conditions. While the test results were in the narrow range of 45-50 GPa, they showed a general reduction (maximum of 10%) of DME for the concrete exposed to cyclic conditions, which indicates the existence of fissures and micro-cracks in the cementitious matrix.

5.5.2 RCPT Test (Rapid Chloride Permeability Test)

After and before being subjected to different environmental conditions, top 50-mm think slices were cut from all 100 mm diameter cylindrical cores. After operating the RCPT for 6 hours according to ASTM C1202 (Standard Test Method for Electrical Indication of Concrete's Ability to Resist Chloride Ion Penetration), the penetration depth was measured on concrete specimens extracted from different locations in the slabs subjected to freezing-thawing and wetting-drying conditions. The whitish color of the penetration depth was clearly visible as depicted in Fig. 5.13, and the results are listed in Table 5.1. In contrast to the freezing-thawing exposure, Table 5.1 shows that the specimens extracted from the slab subjected to wetting-drying cycles yielded relatively higher penetration depths in the vicinity of the crack location, which signifies that the pore structure was highly interconnected in these specimens. This can be attributed to a higher intensity of micro-cracks due to the matrix fatigue resulting from high strain fluctuations of repetitive swelling and shrinkage in the wetting-drying exposure. These results are consistent with the higher concrete and reinforcement strain values for the spacemen G-WD exposure to drying conditions.

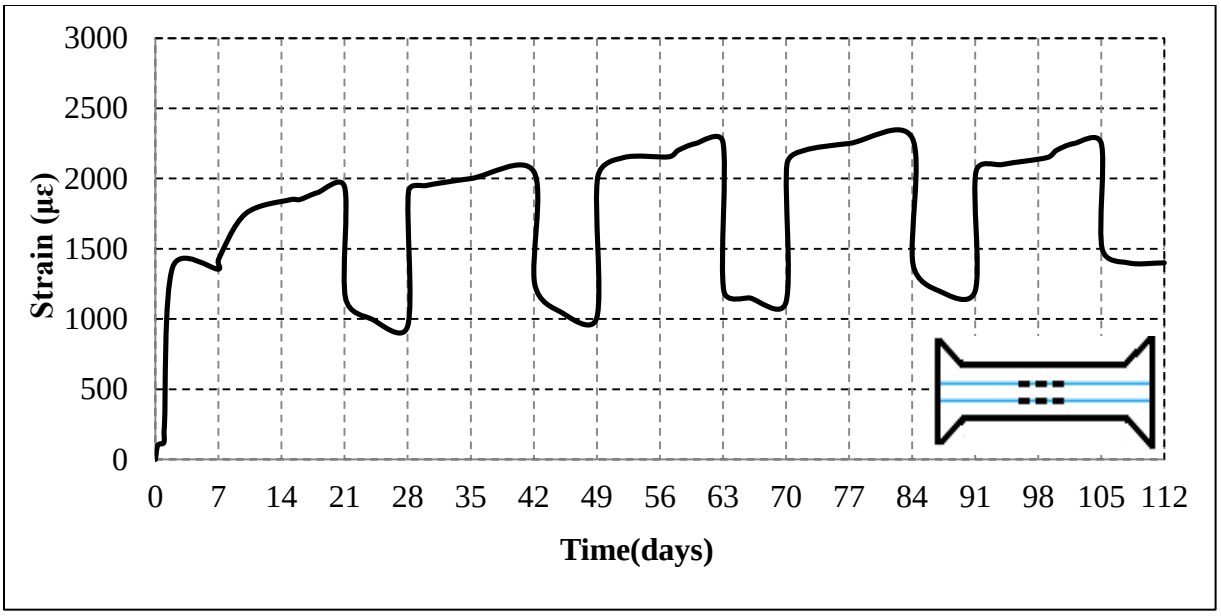

Fig. 5.11: Development of the bar strains in the slab G-WD under wet-dry conditions.

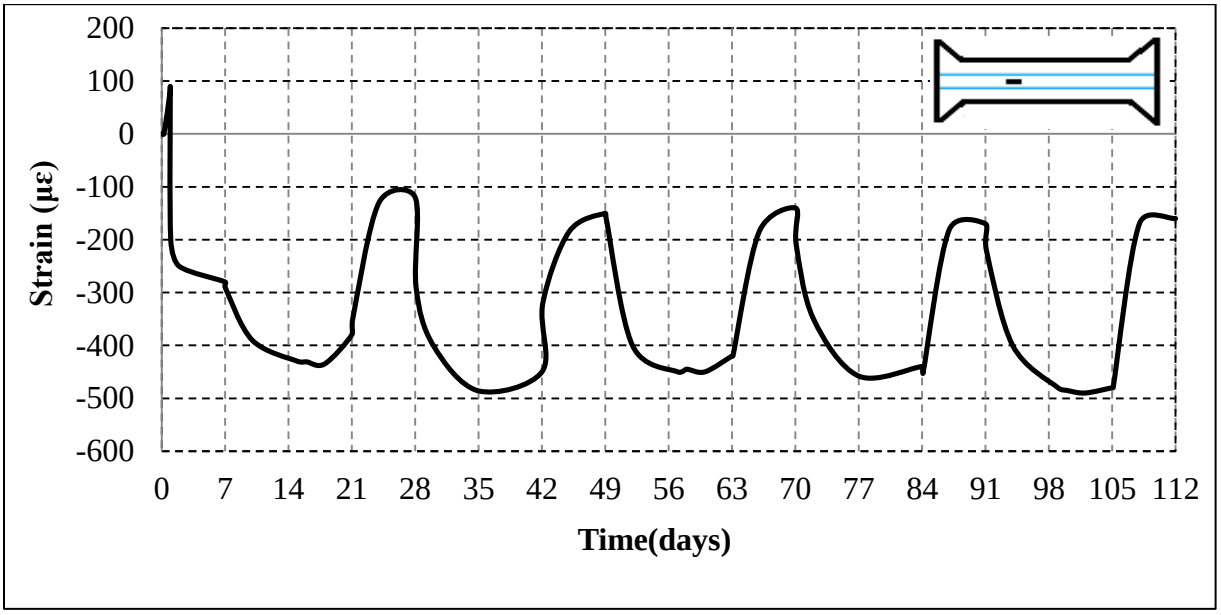

Fig. 5.12: Surface strain of the concrete in the vicinity of the first crack.

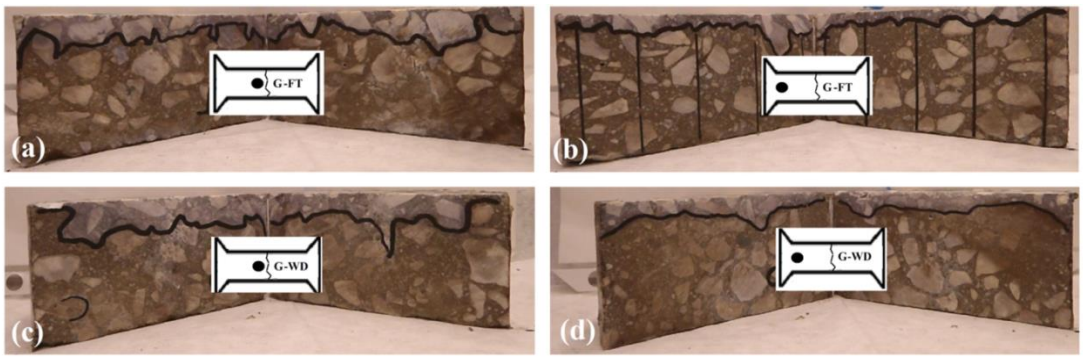

Fig. 5.13: Chloride penetration depth in cores extracted from: (a) slab G-FT close to the crack area, (b) slab G-FT out of the crack area, (c) slab G-WD close to the crack area (d) slab G-WD out of the crack area.

Table 5.1: DME and RCPT results

Exposure	**Cores**	**Dynamic Modulus of Elasticity** (GPa)	**Average Penetration Depth** (mm)
Normal (un-exposed)	C-R	50	7
	C-L	49	6
	A-R	52	5
	A-L	51	6
Freezing and Thawing	C-R	48	8
	C-L	49	8
	A-R	46	7
	A-L	48	8
Wetting and Drying	C-R	48	9
	C-L	48	12
	A-R	47	8
	A-L	45	8

C: Center, A: Away from center, L: Left, R: Right

5.5.3 Microstructural Analysis

To supplement the results of UPV and RCPT, the alteration of microstructure of concrete was also assessed by backscattered scanning electron microscopy (BSEM) on thin sections from cores extracted from G-FT and G-WD in the vicinity and away from the main crack. The polished sections were prepared from fracture surfaces that were dried at 40 °C for 24 h, impregnated with low-viscosity epoxy resin under pressure, cut, polished and carbon coated.

The SEM micrographs show that the specimen subjected to wetting-drying conditions particularly in the vicinity of the main crack (Fig. 5.14 (a)) had higher intensity of micro-cracks and internal damage than that of the concrete exposed to freezing-thawing cycles (Fig. 5.14 (b)). This trend is consistent with the RCPT test, the higher recorded concrete and reinforcement strain values in the vicinity of the crack, and the crack width for the specimen under wetting-drying conditions.

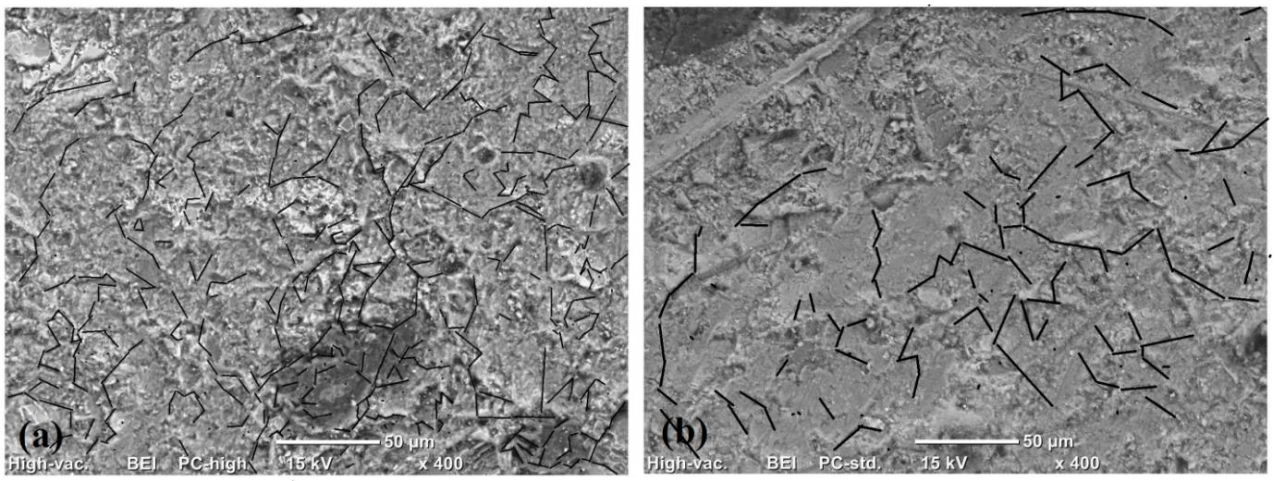

Fig. 5.14: Typical SEM micrographs from: (a) specimen G-WD (slab under wetting and drying conditions), and (b) specimen G-FT (slab under freezing and thawing conditions) at vicinity of the main crack.

CHAPTER 6: NUMERICAL ANALYSIS

6.1 GENERAL

Generally, the verification and revision of any design provisions or guidelines require a reasonable population of data with a wide range of variables. However, the research in the area of FRP-RC structures is still very limited possibly due to the inherent difficulties in simulating restrained shrinkage in full-scale specimens in the laboratory. Therefore, the early-age behavior of GFRP-RC bridge deck slabs subjected to shrinkage is still largely unexplored. The Finite Element Modeling (FEM) provides an effective tool to simulate laboratory conditions with a high degree of accuracy for any complex structural experiment without the constraints of time and cost. This numerical study aims to investigate the effect of key design parameters, namely, concrete strength and cover as well as reinforcement type and spacing, on early-age cracking of FRP-RC bridge deck slabs.

In this chapter a finite element model (FEM) for predicting early-age behavior of reinforced concrete (RC) bridge deck slabs with fiber-reinforced polymer (FRP) bars is presented. The FEM was constructed using specialized software for the analysis of RC structures: ATENA (Version 5). The results of the model were verified against the phase I experimental test results of four full-scale end-restrained slabs (2500 mm long × 765 mm wide × 180 mm thick). The model was verified for cracking pattern, crack width and spacing, and reinforcement strains in the vicinity of the crack using different types and ratios of longitudinal reinforcement. The FEM was able to predict the experimental results within 6 to 10% error. The verified FEM was utilized to conduct a parametric study investigating the effect of five key parameters including reinforcement surface texture, bar spacing, concrete cover, FRP bar type, and concrete compressive strength on the behavior of FRP-RC bridge deck slabs subjected to restrained shrinkage at early-age.

6.2 NUMERICAL STUDIES

A limited number of parametric studies using FEM have been carried out on steel-RC bridge deck slabs subjected to shrinkage. According to a FEM study conducted by Hadidi and Saadeghvaziri (2005), it was concluded that slab sectional stiffness and girder spacing have a significant impact on early-age cracking patterns and stress histories in steel-RC bridge deck slabs. Also, Munnetyan et al. (2011) performed a non-linear FEM (using ABAQUS software) to examine the effect of temperature variation in the external steel girders on early-age cracking in RC bridge deck slabs. They found that cooling the lower flange of the girder, at negative moment regions, during concrete hydration would increase the compressive stresses at the surface of the deck after dissipation of the hydration heat and mitigate tensile stresses due to drying shrinkage.

6.3 FINITE ELEMENT MODEL (FEM)

This section introduces the fundamental steps to construct the FEM including element types, material models and boundary conditions. A total of four element types were defined in this program to model concrete, steel support plates, end steel bars and main FRP reinforcement.

In the experimental study all slabs were effectively anchored at its ends by 1473×1000×1200 mm concrete blocks. However, in the FEM, those blocks were replaced with 50-mm thick stiff steel end plates to reduce number of elements and solution time. The model generated is shown in Fig. 6.1 (a and b). One-dimensional (1-D) reinforcement bars were added to the model by first creating two joints to define the start and end points of the reinforcement. The reinforcement layout of the model is shown in Fig. 6.1(c).

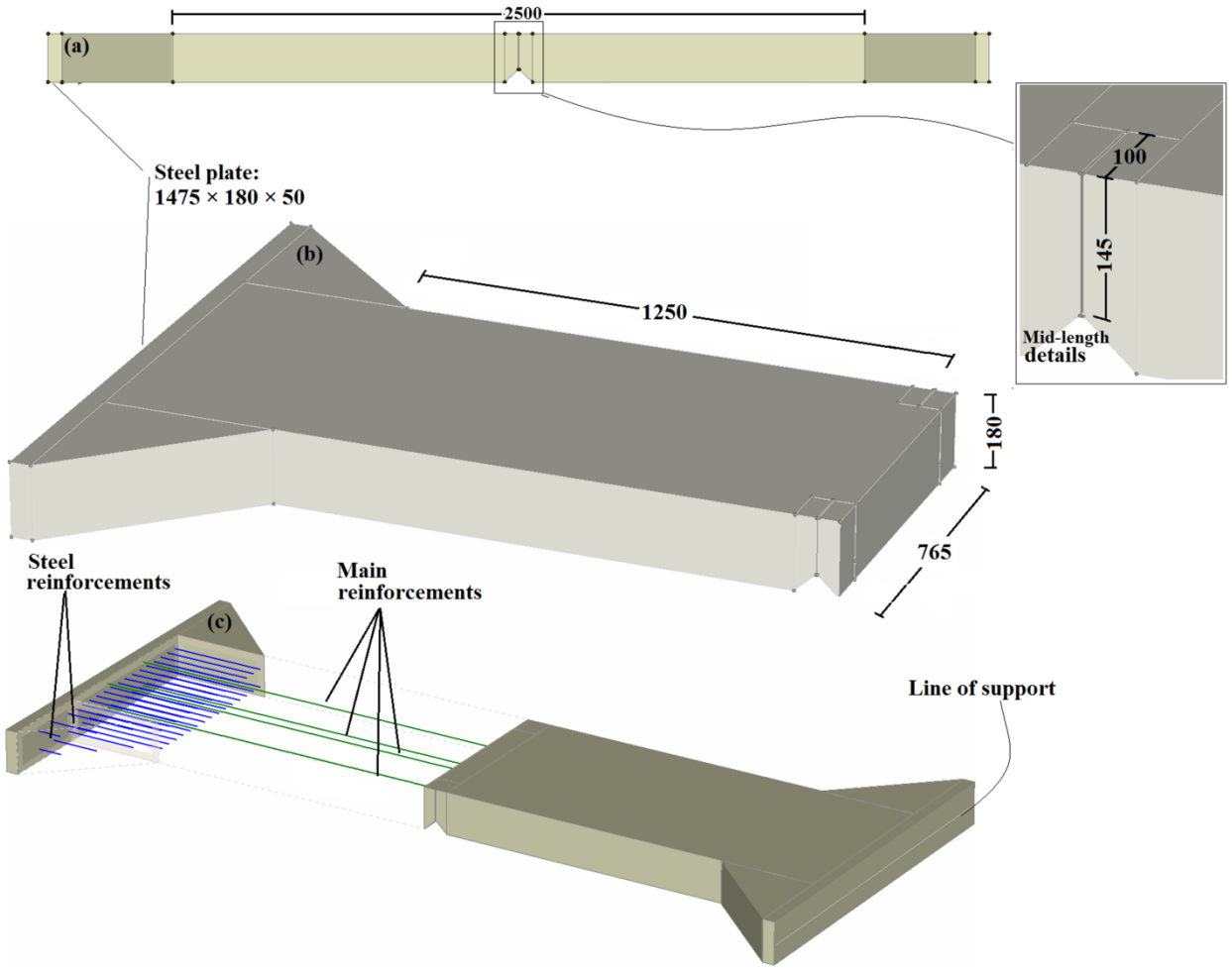

Fig. 6.1: Model geometry: (a) side view (b) 3D view of the analytical model based on the experimental test specimens, and (c) locations of the reinforcing bars (all dimensions are in *mm*).

6.3.1 Concrete

The 3-D eight-node solid brick element (Fig. 6.2) was used to model the geometry of the slabs (except the corner parts). A brick element is only available to be used for hexahedron-shaped elements. This element is defined by 8 corner nodes with five degrees of freedom (DOFs) at each node (Cervenka et al. 2012), as well as 12 additional integration points as shown in Fig. 6.2 (b). The brick element is ideal to use whenever it can be since it is generally accurate and can significantly reduce analysis time required by the computer compared to the other element types

(Cervenka et al. 2005). The geometry of the corner parts were modeled using 3-D four-node tetrahedron solid elements. This element is defined by 4 corner nodes with five DOFs at each node (Cervenka et al. 2012), as well as with 6 additional integration points as shown in Fig 6.2(c). Tetrahedron element should be used whenever there is some sort of irregularity in an element, such as an opening on its surface or triangle-shaped elements. The tetrahedron element is more flexible than a brick element but can also result in increased processing time (Cervenka et al. 2005).

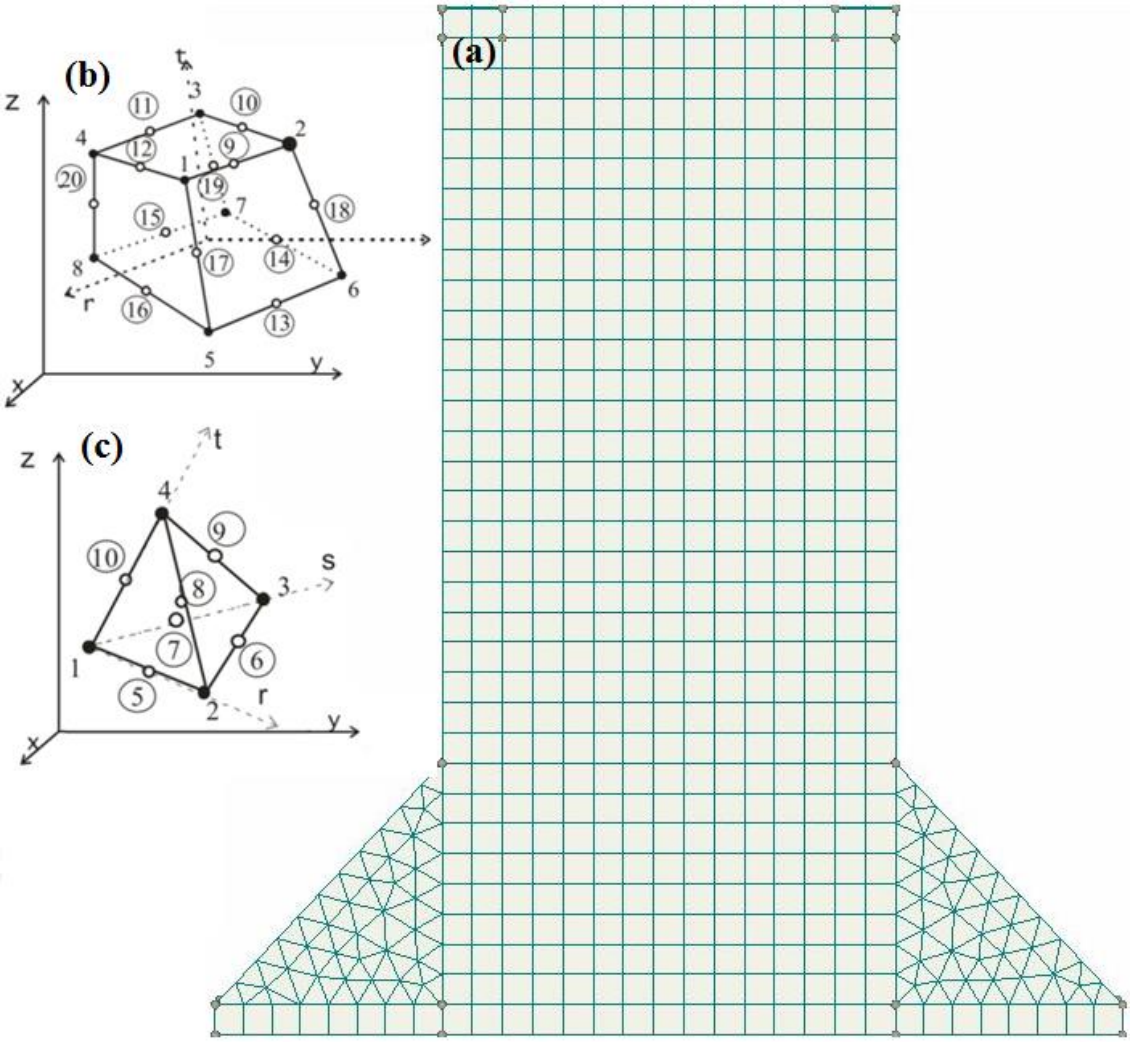

Fig. 6.2 Different finite element types used: (a) top view of the finite element mesh of the analytical model (b) brick element, and (c) tetrahedron element.

In this study, the material model "CC3DNonLinCementitious2Variable" was assigned for both concrete brick and tetrahedron elements. Since the concrete properties changes versus time, this material model allows to define time-dependent properties for concrete. Therefore, the equation recommended by ACI 209.2R-08 (ACI 2008), Eq. 6.1, was adopted to estimate the strength development of concrete as a function of time, using concrete compressive strength at age 28 days (t (day) and $f'_{c,t}, f'_{c28}$ (MPa)).

$$f'_{c,t} = \left[\frac{t}{4+0.85t}\right] f'_{c28} \quad \textbf{[Eq. 6.1]}$$

The "CC3DNonLinCementitious2Variable" material model is able to account for the nonlinearity of concrete and provides smeared cracking information in the three main perpendicular directions. The concrete fracture is modelled by a smeared crack model based on Rankine tensile criterion (Cervenka et al. 2012). The concrete plasticity model is based on the Menetrey-William failure surface equation (Cervenka et al. 2012). The Menetrey-Willam failure surface adopts the uniaxial compressive test of concrete based on the experimental work of Van Mier (Cervenka et al. 2012), where in the concrete stress-strain relationship, the softening curve is linear (Fig. 6.3). The elliptical ascending part is given by the following equations:

$$\sigma = f'_{co} + \left(f'_c - f'_{co}\right)\sqrt{1 - \left(\frac{\varepsilon_c - (f'_c/E_c)}{\varepsilon_c}\right)^2} \quad \textbf{[Eq. 6.2]}$$

Where $f'_{co} = 2f'_t$ **[Eq. 6.3]**

$$W_d = (f'_c/E_c - \varepsilon_c^p)L_c \quad \textbf{[Eq. 6.4]}$$

where σ is the concrete compressive stress (MPa), E_c is the concrete modulus of elasticity (GPa), f'_c and f'_t are the concrete compressive and tensile strength (MPa), respectively, W_d is the end point of the softening curve (W_d = - 0.0005 *mm* for normal strength concrete as recommended by

the software guidelines), f_{co} is the starting point of the non-linear curve (MPa), ε_c^p is the value of plastic strain at the max compressive strength, on the descending curve, and L_c is the element length scale parameter.

The cracking behavior of concrete was modeled according to the equation developed by Hillerborg et al. (1976) (Eq. 6.5) as represented in Fig. 6.3 (c). The width of crack in this equation is calculated based on three factors: the shape of the softening curve, tensile strength and fracture energy. The effect of tension stiffening where cracks cannot fully develop along the section is also considered. Tension stiffening is simulated by specifying a factor that represents the relative limiting value of tensile contribution as a fraction of the tensile capacity of the concrete.

$$\frac{\sigma}{f_t'} = \left(1 + 3067 \frac{w}{5.14 G_f / f_t'}\right)^3 exp\left(-6.93 \frac{w}{5.14 G_f / f_t'}\right) - \frac{w}{5.14 G_f / f_t'}(1 + 3067^3) \qquad \textbf{[Eq. 6.5]}$$

where w is the crack width (mm), G_f is the concrete fracture energy (MN/m), σ is concrete actual tensile stress (MPa), and f'_t is the concrete tensile strength (MP*a*). The software generates the concrete properties using the concrete cube strength, f'_{cu} (MPa). Equation 6.5 was used to define concrete cube strength from standard cylinders tests. Poisson's ratio was assumed to be 0.2, and the concrete tensile strength, f'_t (MPa), initial modulus of elasticity (E_c) (MPa), and fracture energy (G_f) (MN/m) were calculated based on the following equations used in this software (Cervenka et al. 2012):

$$f'_{cu} = 1.15\, f'_c \qquad \textbf{[Eq. 6.6]}$$

$$f'_t = 0.24\, (f'_{cu})^{2/3} \qquad \textbf{[Eq. 6.7]}$$

$E_c = (6000 - 15.5\, f'_c)\, \sqrt{f'_{cu}}$ **[Eq. 6.8]**

$G_f = 0.000025\, f'_t$ **[Eq. 6.9]**

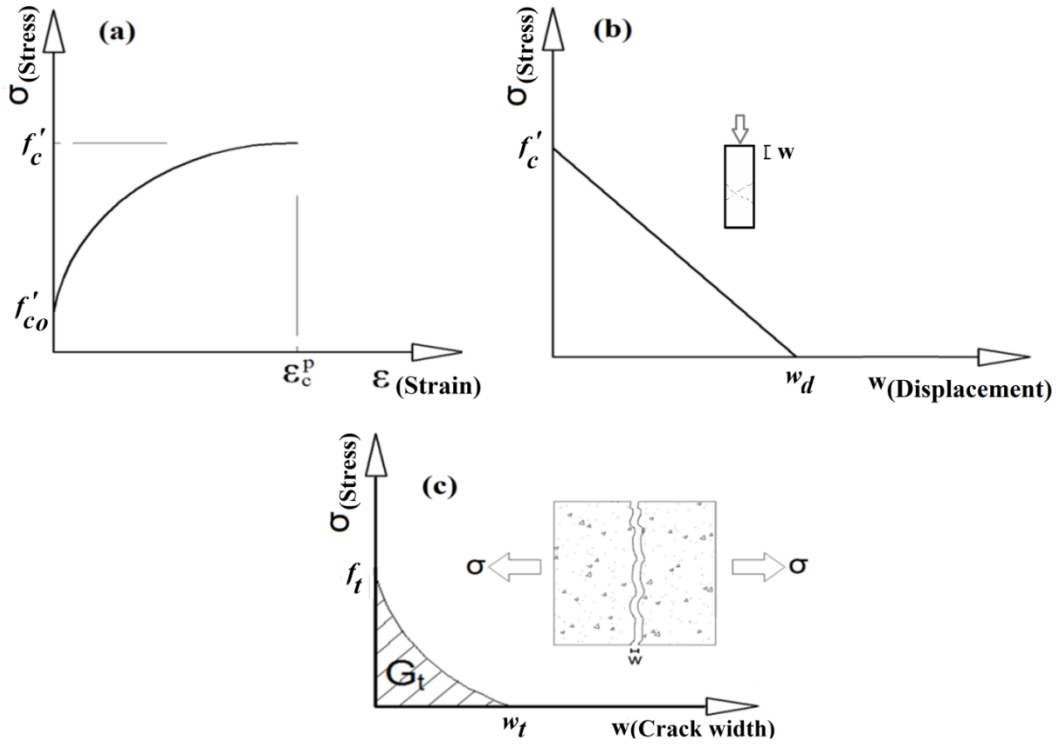

Fig. 6.3: Van Mier compressive stress-strain relationship of the concrete: (a) non-linear ascending part (b) linear descending (softening) part, and (c) stress-crack opening according to Hodjik law (reproduced from Cervenka et al. 2012).

6.3.2 Steel Support Plates

Lines along the surfaces of the outside edges of the end steel plates were fixed in all directions to simulate fixed end conditions. These plates were modeled using the same brick element but with the 3-D Elastic Isotropic material. The yield strength, modulus of elasticity, and Poisson's ratio were assumed to be 420 MPa, 200 GPa and 0.3, respectively.

6.3.3 Reinforcing Bars

Since the bar spacing is an important factor affecting the cracking behavior, the discrete method was selected for modeling reinforcement in the concrete. In this regard, the 1-D "Reinforcement"

truss element was used for both FRP and steel reinforcing bars. The basic characteristics of the steel reinforcement were determined using a bi-linear form with yield strength and elastic modulus of 420 MPa and 200 GPa, respectively. The GFRP reinforcement has a linear elastic behavior up to failure. Table 6.1 provides the material properties of the reinforcement used in the FEM.

Table 6.1: Mechanical properties of GFRP, CFRP and steel bars

Bar type	**Bar diameter (mm)**	**Bar area (mm^2)**	**Modulus of elasticity (GPa)**	**Tensile strength (MPa)**	**Tensile strain (%)**
GFRP #4	12.7	127	65	1453	2.23
GFRP #5	15.9	198	62	1450	2.23
GFRP #6	19.1	285	63	1484	2.35
CFRP #4	12.7	127	144	1899	1.32
CFRP #5	15.9	198	140	1648	1.18
Steel 15M	16	200	200	$^{*}f_y$ = 420	$^{*}\varepsilon_y$ = 0.21
Steel 25 M	25	500	200	f_y = 420	ε_y = 0.21

$^{*}f_y$: Steel yield strength, ε_y: Steel yield strain.

The bond stress-slippage relationship between concrete and reinforcement has a significant effect on the performance of RC structures. For this model, the stress-slippage relationship was defined using the "Bond for Reinforcement" option. Different bond stress-slippage relationships were used to define the response of bond elements for the steel, GFRP and CFRP bars. The stress-slippage model recommended by CEB-FIP Model Code (CEB-FIP 1990) was used for steel bars (Fig. 6.4). The interface between reinforcement and surrounding concrete used for different surface pattern of CFRP bars were based on the study by Mavar et al. 2003 (Fig. 6.4). For sand-

coated and ribbed-deformed GFRP bars, the interfaces were defined based on the study by Alves et al. 2011 and manufacture specifications, respectively (Fig. 6.4).

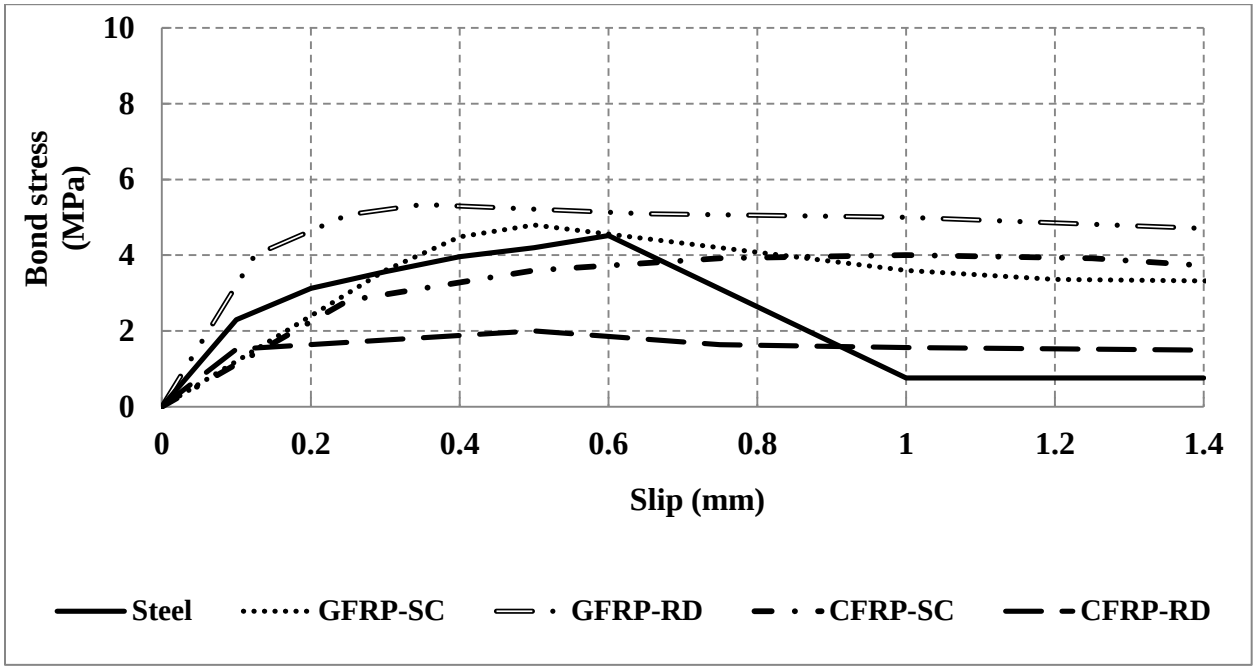

Fig. 6.4: Bond-slip relationship for different types of reinforcement in concrete at 3 days.

6.3.4 Meshing of the Model

In this study, each specimen was meshed into 8545 finite elements with a side length of 50 *mm* each. Also, each steel end-plate was meshed into 124 elements. Since the program automatically generates embedded finite elements for the reinforcement bars, 1-D entities such as bar does not need to be meshed by the user before the model analysis is started.

6.3.5 Shrinkage Profile

To estimate the shrinkage profile of concrete, ACI 209.2R-08 (ACI 2008) recommends different models such as ACI 209 (Eq. 6.10), Bažant-Baweja B3 (Eq. 6.11), GL2000 (Eq. 6.12) and CEB-FIP/90 (Eq. 6.13) to predict time-dependent shrinkage of concrete.

$$\varepsilon_{sh(t)(ACI\ 209)} = \frac{(t-t_c)}{26e^{\{v/s 1.42\times10^{-2}\}}+(t-t_c)}\gamma_{sh}(-780)\times10^{-6} \quad \textbf{[Eq. 6.10]}$$

$$\varepsilon_{sh(t)(B3)} = tanh\sqrt{\frac{(t-t_c)}{0.85{t_c}^{-0.08}{f_{cm28}}^{-0.25}[2(v/s)]^2}}\ k_{(h)} \times -\varepsilon_{sh\infty} \quad \textbf{[Eq. 6.11]}$$

$$\varepsilon_{sh(t)(GL2000)} = [(t-t_c)/\{t-t_c+0.12(v/s)^2\}]^{0.5}\beta_{(h)} \times -\varepsilon_{shu} \quad \textbf{[Eq. 6.12]}$$

$$\varepsilon_{sh(t)(CEB-MC90)} = [\frac{(t-t_c)}{350\left[(v/s)/50\right]^2+(t-t_c)}]^{0.5}\ \beta_{RH(h)} \times \varepsilon_{cso} \quad \textbf{[Eq. 6.13]}$$

Where γ_{sh} represents the cumulative product of the applicable correction factors for fresh concrete properties and ambient humidity conditions in the ACI 209 model, $\varepsilon_{sh\infty}$, ε_{shu} and ε_{cso} are the notional ultimate shrinkage (mm/mm) based on RILEM data bank (RILEM 1998) for Bazant, GL 2000 and CEB-MC90 equations, respectively. Also, $K_{(h)}$, $\beta_{(h)}$, and $\beta_{RH(h)}$ are the ambient relative humidity factor for Bazant, GL2000 and CEB-MC90 models. Moreover, t and t_c are the concrete age and curing time (*day*), respectively, and *v/s* is member's volume-to-surface ratio (mm). In these models the concrete was assumed to be moist cured at least for 1-14 days.

It is well-documented in the literature (Mehta and Monteiro 2014; Sakata and Ayano 2001) that ambient environmental conditions in terms of combined temperature and humidity changes affect the amount of concrete shrinkage. However, the effect of temperature on concrete shrinkage is explicit in most of the prediction equations mentioned above. Nevertheless, the CEB-MC90 model incorporates the effect of temperature as well as humidity to predict the shrinkage of concrete versus time. When a constant temperature above 30 *ºC* is applied while the concrete is drying, CEB MC90 recommends Eq. 6.14 to predict concrete shrinkage.

$$\varepsilon_{sh(t,T)(CEB-MC90)} = \left[\frac{t-t_c}{350\left[\frac{v/s}{50}\right]^2 \exp[-0.06(T-20)]+(t-t_c)}\right]^{0.5} \times \beta_{RH(h)}\left[1+\left(\frac{0.08}{1.03-h}\right)\left(\frac{T-20}{40}\right)\right] \times \varepsilon_{cso} \quad \textbf{[Eq. 6.14]}$$

where *h* and *T* are the ambient relative humidity (%) and temperature (ºC), respectively.

In the experimental study, all prototypes were kept inside a plastic tent for 1 day after casting. The profile of shrinkage was accelerated at early-age by increasing the temperature in the tent to 35 °*C* in the first day followed by exposing the slabs to air flow of 50 km/h for 6 days. Table 6.2 provides the environmental conditions applied to all specimens. The CEB-MC90 model was modified to account for the temperature and humidity changes shown in Table 6.2.

Table 6.2: Environmental conditions applied to the slabs versus the time of exposure

Time (day)	**Temperature (ºC)**	**Humidity (%)**	**Ambient conditions**
1	35	85	Slabs subjected to a hot temperature inside a tent
2-7	22	40	Slabs subjected to air flow by fans
8-112	22	65	Slabs subjected to laboratory conditions

The shrinkage strain of concrete ε_{Total} subjected to different environmental conditions was calculated using Eq. 6.15:

$$\varepsilon_{Total} = \varepsilon_{sh(t)(CEB-MC90)} + \alpha_3 \Delta T + AF \quad \textbf{[Eq. 6.15]}$$

where: α_3 is the concrete coefficient of thermal expansion at age of 3 days (~2.55×10^{-6} per ºC, obtained by ASTM-E831 2013), ΔT is temperature change (ºC) between incremental time steps and AF is the effect of air flow on concrete shrinkage (με).

Table 6.3 shows the concrete free shrinkage versus that predicted by the modified CEB-MC90 model (Eq.15). Test results indicate that the advent of air flow at 2 to 7 days led to steady-state

shrinkage. Therefore, the rate of shrinkage in this time interval can be calculated by linear interpolation at a rate of 18.2 με/day. The main part of drying shrinkage caused by air flow (*AF*) occurred within 2-7 days, therefore the remaining shrinkage predicted by CEB-MC90 was distributed within 8-112 days using the model's time function (Eq. 6.16).

Figure 6.5 indicates that the modified CEB-MC90 model could reasonably predict the concrete total shrinkage based on the applied environmental conditions.

$$\text{CEB-MC90 time function} = \left[\frac{(t-t_c)}{350\left[{}^{(v}/_{s)}/_{50}\right]^2+(t-t_c)}\right]^{0.5} \quad \textbf{[Eq. 6.16]}$$

In addition, for high-strength concrete, CEB MC90 model has been developed (CEB 1999) to take into account the particular characteristics of concrete strength. The modified CEB-MC90/99 model subdivides the total shrinkage into the components of drying and autogenous shrinkage (Eq. 6.17). Therefore, in the parametric study, this model was used to predict concrete shrinkage for different concrete strength.

$$\varepsilon_{sh(t,tc)} = \varepsilon_{caso(fcm28)}\beta_{as(t)} + \varepsilon_{cdso(fcm28)}\beta_{RH(h)}\beta_{ds(t)} \quad \textbf{[Eq. 6.17]}$$

where: f_{cm28} represents concrete mean compressive strength ($f_{cm28(ACI\ 318\text{-}11a)}$=1.1$f'_c$+5) (*MPa*), f'_c is the concrete compressive strength (MPa), $\varepsilon_{caso(fcm28)}$ is the nominal autogenous shrinkage coefficient, and $\beta_{as(t)}$ is the function describing the time development of autogenous shrinkage, $\varepsilon_{cdso(\ fcm28)}$ is the nominal drying shrinkage coefficient, $\beta_{RH(h)}$ is the ambient relative humidity for drying shrinkage, and $\beta_{ds(t)}$ is the function describing the time development of drying shrinkage.

Table 6.3: The predicted and experimental values of free shrinkage

Time (day)	Predicted shrinkage per each day by CEB-MC90 (με)	$\alpha_3\Delta T$ (με)	Total Shrinkage rate due to air flow (με)	Shrinkage due to AF (με)	Predicted shrinkage per each day by modified CEB-MC90 (με)	Cumulative predicted shrinkage by modified CEB-MC90 (με)	Cumulative predicted shrinkage by CEB-MC90 (με)	Cumulative experimental shrinkage value (με)
1	-18.000	-33.000	0.000	0.000	-51.000	-51.000	-18.000	-60.000
2	-11.615	0	-18.160	-6.545	-18.160	-69.160	-29.615	-95.000
3	-6.629		-18.160	-11.531	-18.160	-87.320	-36.244	-113.000
4	-5.576		-18.160	-12.584	-18.160	-105.480	-41.819	-132.000
5	-4.901		-18.160	-13.259	-18.160	-123.640	-46.720	-155.000
6	-4.421		-18.160	-13.739	-18.160	-141.800	-51.141	-167.000
7	-4.056		-18.160	-14.104	-18.160	-159.960	-55.198	-169.000
28	-0.130		0	0	-0.130	-167.451	-74.992	-169.447
42	-0.103				-0.103	-169.045	-90.931	-169.745
56	-0.086				-0.086	-170.349	-103.971	-170.043
70	-0.075				-0.075	-171.465	-115.128	-170.340
90	-0.063				-0.063	-172.832	-128.799	-170.766
112	-0.054				-0.054	-174.115	-141.629	-171.000

6.3.6 Analysis

The geometric and material non-linear solution was taken into account by the program using the concept of incremental step-by-step analysis. The shrinkage was applied in 112 load increments; each represents one day of the shrinkage load. At each increment, load iterations were performed until the convergence criteria were satisfied. Four solution errors serve to check convergence criteria: displacement increment normalized residual force, absolute residual force, and energy dissipated (Cervenka et al. 2012). After reaching the equilibrium and completion of each loading

step, the stiffness matrix was adjusted to reflect the non-linear changes before proceeding to the next load step. In this regard, the program adopts full Newton-Raphson method to modify the solution parameter. It should be noted that the solving time for running each model was approximately 50 hours.

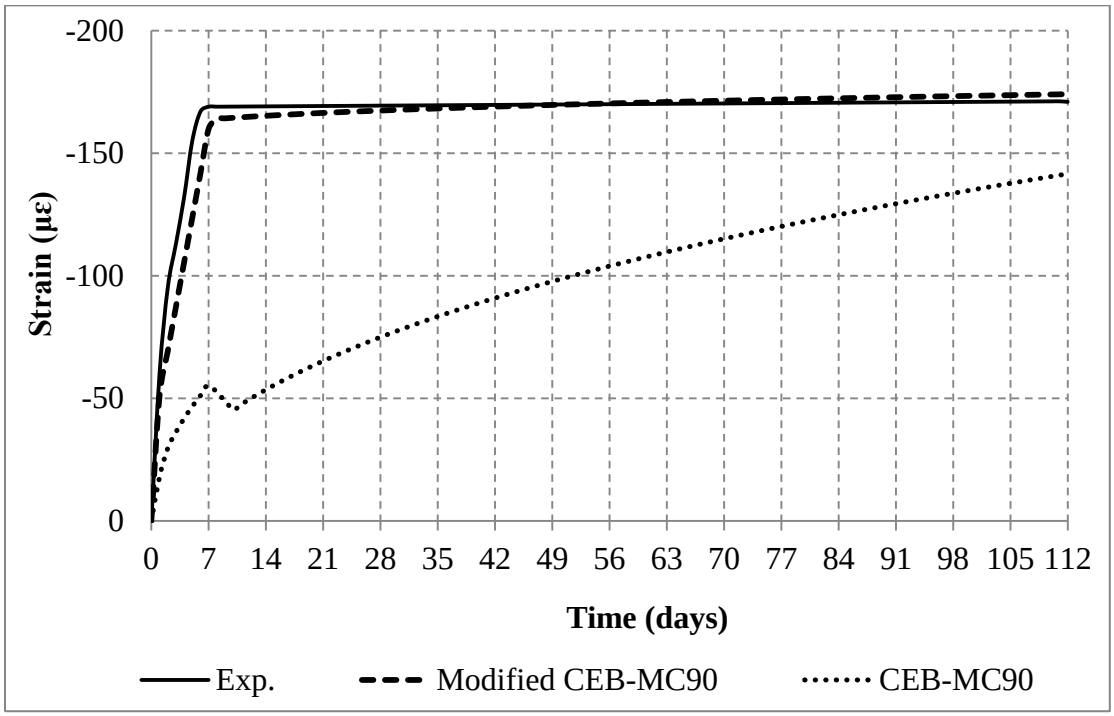

Fig. 6.5: Experimental and predicted shrinkage values.

6.3.7 Model Verification

For the verification process, the experimental results of the four bridge deck slabs were used. The constructed model was calibrated against specimen SG2 and then tested on the remaining specimens to ensure that the results remained within a reasonable error. The model was verified in terms of crack width, crack pattern and average tensile strains in the reinforcement at the crack location. For generalization of the FEM, the predicted shrinkage by modified CEB-MC90 method, assuming wet curing conditions, was also applied to the model. The FEM results for

crack width and reinforcement strain remained within a reasonable error of 6% and 10%, respectively. Also, the main crack pattern in the FEM was recorded at a similar location to the experimental program; however, the secondary cracks did not occur in the FEM which were contradicted with the experimental study for specimens SG4 and SS.

6.3.7.1 Cracking pattern

Figure 6.6 shows the cracking pattern for the FEM models and experimental tested slabs. In the experimental study, there was one main crack located at the middle reduced cross section of the slab. The main cracking pattern for the FEM models accurately predicted the crack pattern observed in the experimental program at the middle section. The experimental results indicate that an increase in the reinforcement area or modulus of elasticity (SG4 and SS compared to SG2 and SG3) leads to less stiffness reduction at first cracking (mid-span), thus the restraining force after cracking remains high. With such high restraining force, the development of additional drying shrinkage or temperature variation causes the concrete in regions away from the first crack to experience further cracking. However, the FE results did not record secondary crack pattern on the models for SG4 and SS.

6.3.7.2 Crack width

In the FEM, the crack width was considered as the average of the displacements measured by monitoring points at two locations across the slab width at mid-span (replicating the same approach as that of the PI gauges used in the experimental study). Figure 6.7 represents the crack width development curves for the experimental and the numerical study. The crack width-time diagrams show several important relationships for the models. In the finite element model for SG2 (ρ = 0.5%), the crack width reached the allowable value of 0.5 mm (ACI 440 2006, CSA 2006) after 5 days. After 112 days, this crack width reached 0.67 *mm*. The FEM results reveal

that for SG3 (ρ = 0.7%), SG4 (ρ = 1.1%) and SS (ρ = 0.7%), the crack width were 0.34, 0.26 and 0.20 mm after 112 days. The predicted crack widths in the FEM lie within an average error of 6%. The comparison between the results shows that the FEM was able to accurately predict the final crack width for the GFRP and steel RC slabs (Fig. 6.7).

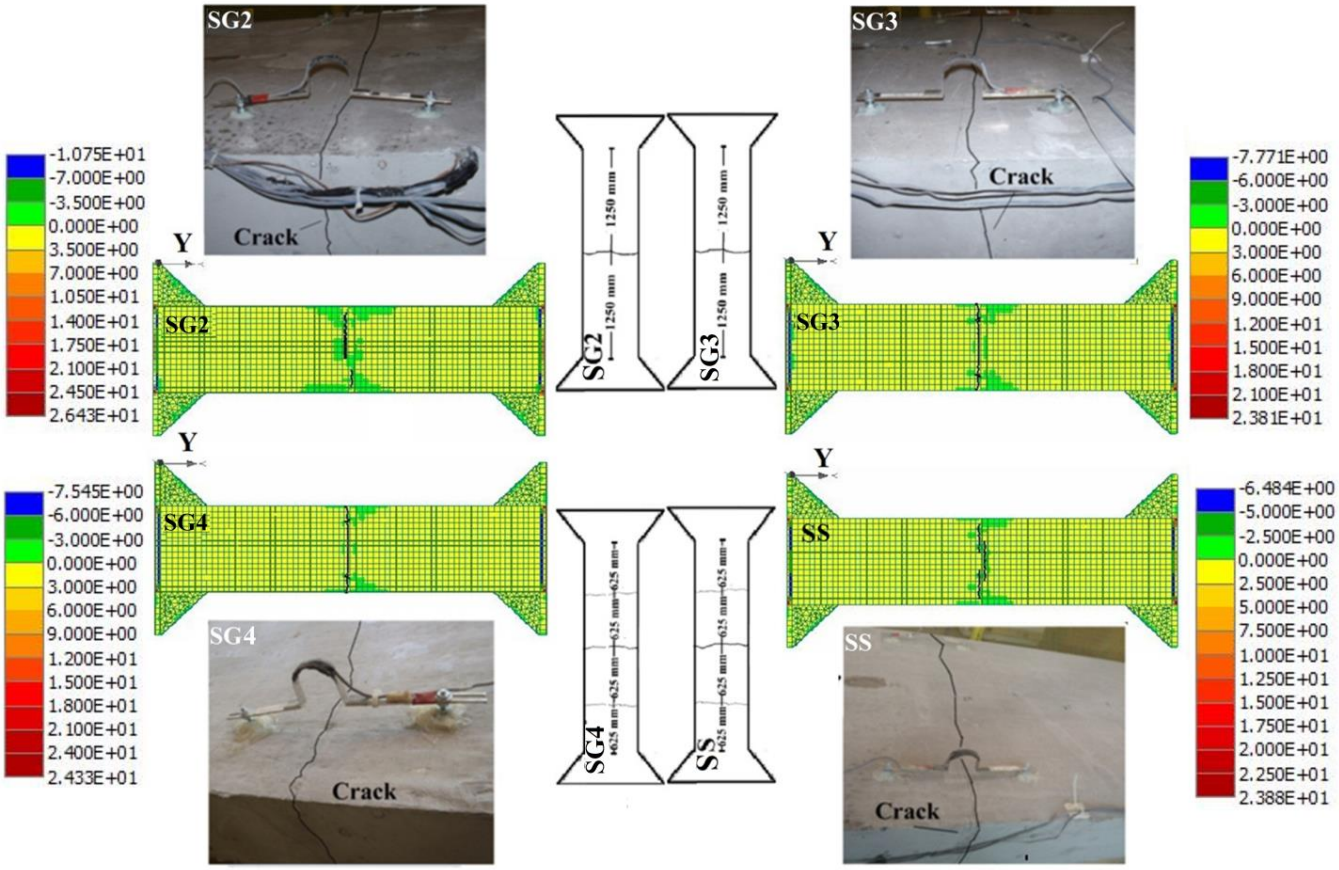

Fig. 6.6: Concrete stresses in the Y direction (*MPa*) and cracking pattern.

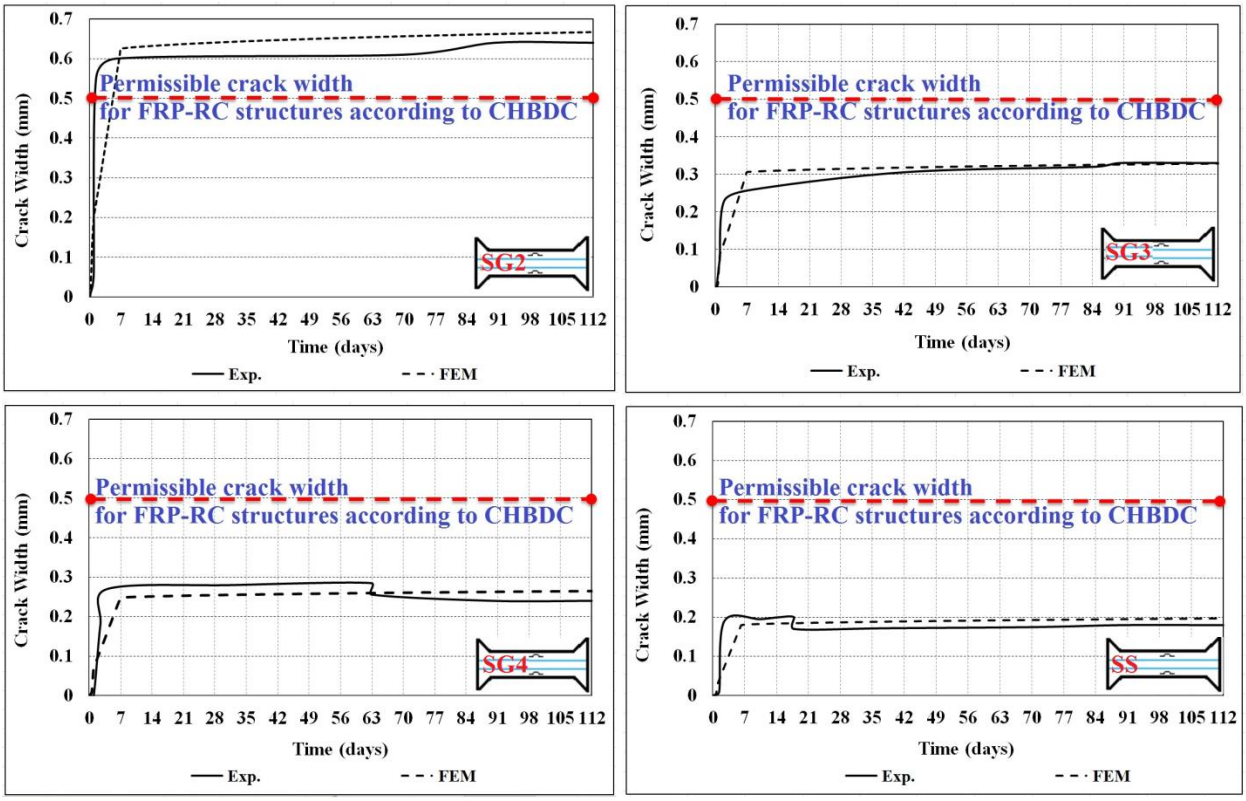

Fig. 6.7: Experimental and FEM results for the development of crack width with time for slabs SG2, SG3, SG4 and SS.

6.3.7.3 Reinforcement strain

In the experimental study, the strains in main reinforcement were measured by strain gauges attached to each rebar at mid-span. A similar approach was followed in the FEM by defining four monitoring points at the same locations. Figure 6.8 shows the predicted and experimental tensile strains in reinforcement at the cracking location. The results show that, once a crack developed at mid-span, the average strain in reinforcement increased rapidly. This value decreased with increasing the reinforcement ratio or modulus of elasticity. In FEM for SG2, SG3, SG4 and SS, the average strains in the bars at crack location were 2590, 1400, 1130 and 480 με after 112 days. However, the strain away from cracking location was still less than 200 με. The strain in the reinforcement at the crack location was also efficiently predicted by FEM subjected to shrinkage within an average error of 10% (Fig. 6.8).

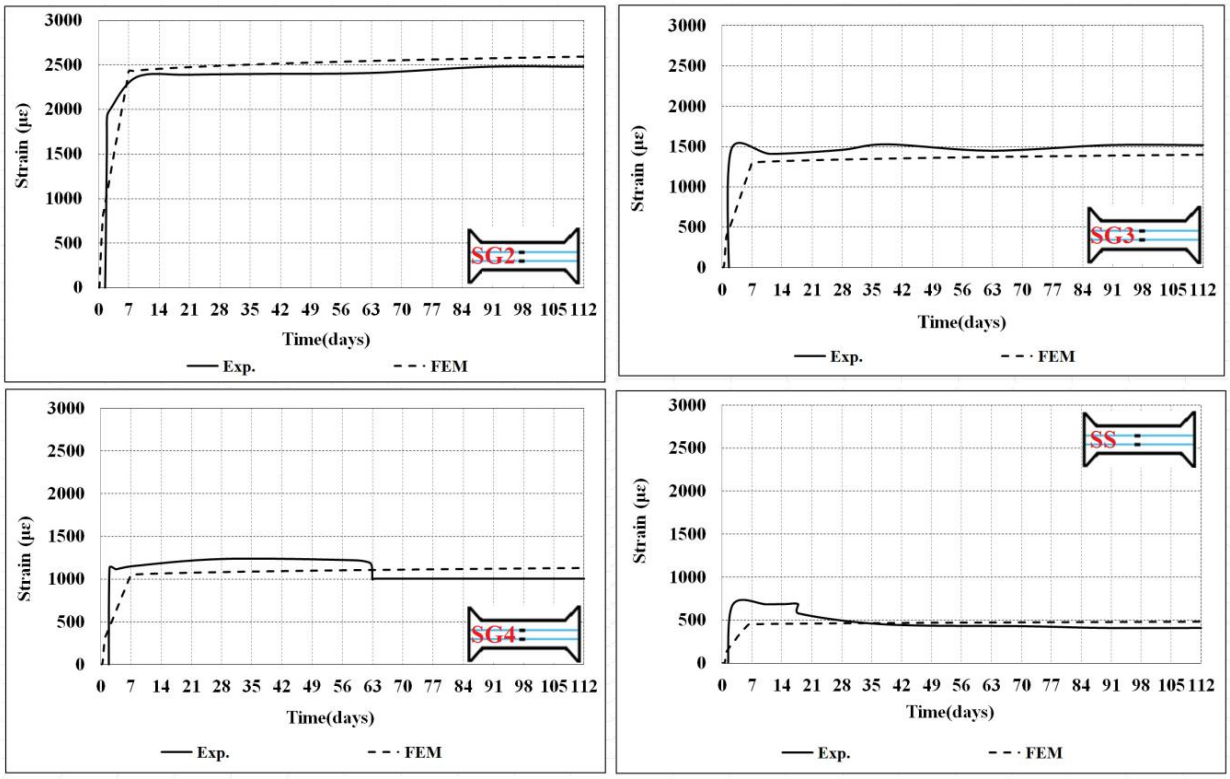

Fig. 6.8: Experimental and FEM results for the development of bar strains at crack location for slabs SG1, SG2, SG3 and SS.

6.3.7.4 Model verification for slabs subjected to freeze-thaw and wet-dry cycles

The cyclic wet-dry and freeze-thaw are described as the main ambient conditions which may lead to volume instability in the restrained concrete deck slabs. Volume changes due to repetitive shrinkage/swelling may lead to material fatigue and de-bonding of reinforcement (Zhang et al. 2012; Ayano et al. 2002). Therefore, these conditions can be considered critical in the durability-based design of concrete structures.

It is well-known that the most of the materials except water experience expansion and contraction when they are exposed to hot and cold environments, respectively. Water molecule is composed of two hydrogen atoms connected with an oxygen atom. Their connection angel in the liquid state is 105° 06', when water changes into the ice state, the connection angel increases to

109° 28’ (Krylov 1997). This phenomenon increases the volume of the water by about 9%. Therefore in the concrete with high internal relative humidity (RH>90%) water plays an important role on the concrete volumetric instability when it is subjected to freeze/thaw conditions.

According to the experimental results for the specimen subjected to freeze-thaw conditions, crack width and bar strain at the vicinity of the main crack reached to their maximum and minimum point at +4 °C (thawing) and -18 °C (freezing), respectively, in each cycle. This behaviour is attributed to the frost action in the saturated concrete. The effect of frost action on the concrete was studied by many researchers (Towers and Helmuth 2008; Scherer et al. 2002; Krylov 1997). It is found that, at the onset of ice crystallization in the saturated concrete, the frictional resistance to ice growth creates internal pressure in the pores leading to concrete expansion. However, the crack width and bar strain in the vicinity of crack location in the FEM for G-FT were 0.38 and 0.31 mm, and 1460 and 1440 με corresponding to the freezing and thawing stages, respectively (Figs. 6.9 and 6.10).

Experimental results for the specimen subjected to wet-dry conditions indicate that the higher crack width and bars strain in the vicinity of the main crack were recorded during the drying periods, this behaviour can be attributed to the accelerated drying shrinkage due to high ambient temperature (35 ºC), which led to partial opening of the crack. While the FEM for the G-WD shows expansion in the model due to increasing ambient temperature to 35 ºC (Figs. 6.11 and 6.12).

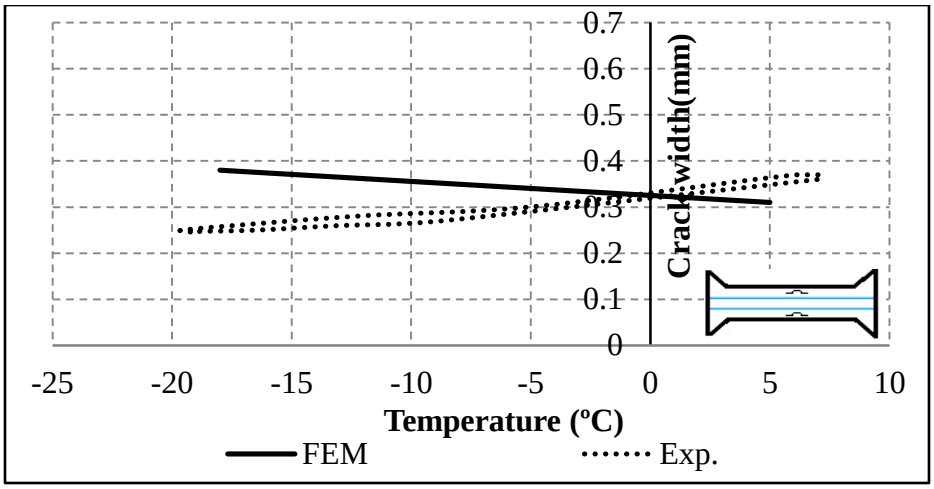

Fig. 6.9: Crack width development in the slab G-FT under freeze-thaw conditions during first cycle.

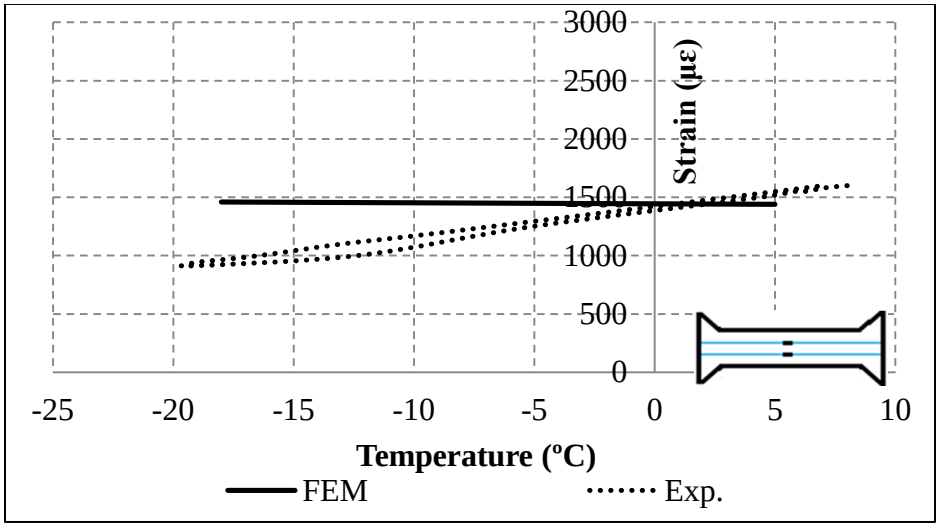

Fig. 6.10: Development of the bar strains in the slab G-FT under freeze-thaw conditions during first.

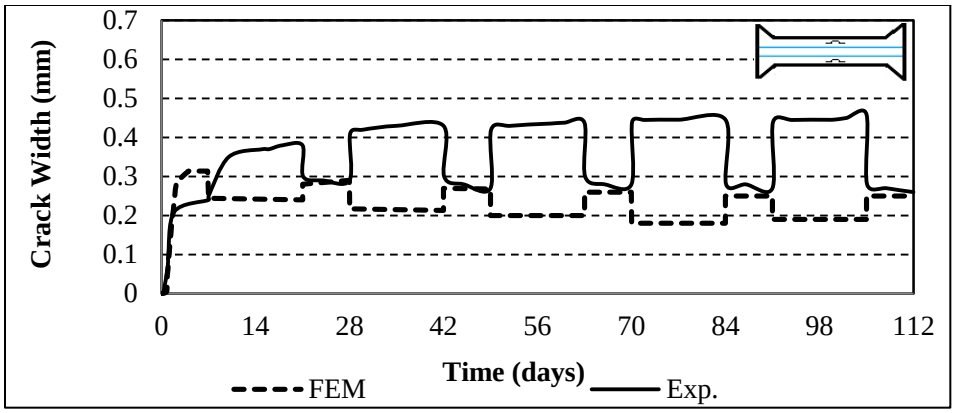

Fig. 6.11: Crack width development in the slab G-WD under wet-dry conditions.

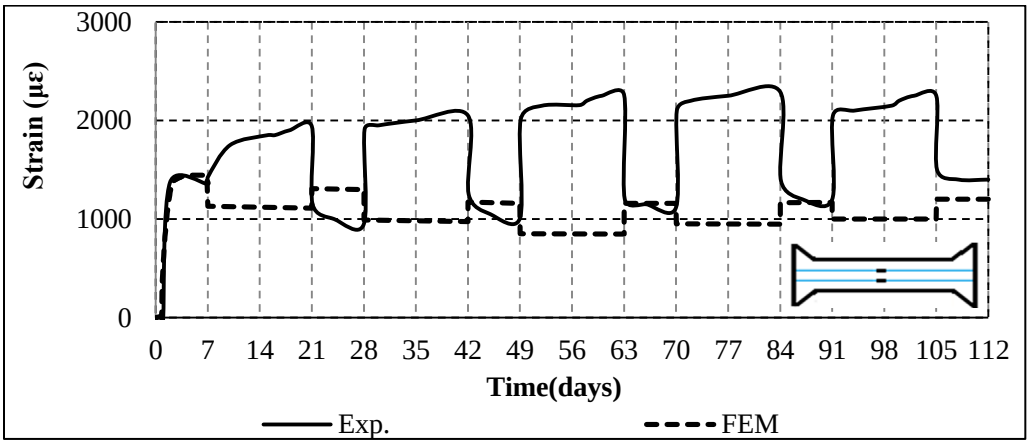

Fig. 6.12: Development of the bar strains in the slab G-WD under wet-dry conditions.

Finite element analytical results appear to contradict those results were obtained in experimental study for the specimens subjected to freeze-thaw and wet-dry conditions. This can be explained by the fact that software is not capable to consider the effect of internal water when the concrete is exposed to freezing or drying conditions.

6.3.8 Parametric Study

This study examined the effect of concrete compressive strength, concrete cover, reinforcement type, and bar spacing on the early-age behavior of FRP-RC bridge deck slabs subjected to shrinkage. Since the FEM results for SG3 were the closest to those of the experimental results, the

parametric study models were developed based on the same assumptions and geometry that were used for modeling slab SG3 in the verification stage. Moreover, the reinforcement ratio for this slab (0.7%) is recommended as the minimum reinforcement ratio for GFRP-RC bridge deck slabs by CHBDC (2006). Table 6.4 provides details of the parametric FEM. The results are presented in terms of cracking pattern and crack width development and reinforcement strain.

6.3.8.1 Concrete compressive strength

In this study, six concrete compressive strengths 30, 40, 50, 60, 70 and 80 MPa were used in the FEM. The applied concrete shrinkage load scheme was obtained according to the CEB MC90-99 method, meeting the requirements of a 3-day moist curing conditions (ACI 209 2008). The predicted shrinkage values indicate that increasing the strength from 30 to 80 MPa intensifies the autogenous shrinkage and consequently increases the concrete total shrinkage value from 170 to 230 με (Table 6.5).

Figure 6.13 (a) shows the typical cracking pattern for different concrete strengths at the notched mid-span location, while Figure 6.13 (b) illustrates the change in crack width and reinforcement strain over 112 days. As concrete strength was increased from 30 to 80 MPa, the crack width and associated reinforcement strain at crack location grew from 0.33 to 0.48 mm and from 1400 to 2020 με, respectively. It is well-documented (Mehta and Montherio 2014) that, in high-strength concrete (with low water-to-binder ratio), consuming water content during the hydration process intensifies autogenous shrinkage in comparison to normal strength concrete. This self-desiccation effect was considered in the predicted load scheme by CEB-MC 90/99, as shown in Table 6.5. Furthermore, bridge deck slabs with high strength concrete offer greater sectional stiffness, which increased the internal restraint, and thus led to an increase in restrained force.

6.3.8.2 Reinforcing bar spacing

In this study, the effect of reinforcement bar spacing on crack control was investigated. A constant reinforcement ratio of $\rho = 0.70\%$ was distributed to 2, 3, 4, 5, 6 and 7 bars (top and bottom) which dictates the spacing ranged between 96 and 255 mm. Figure 6.14 (a) shows the typical cracking pattern for the FEM with different bar spacing at the notched mid-span location. In these models, the cracks typically occurred at mid-span. Results show that reducing the bar spacing from 255 to 96 mm decreases the early-age crack width from 0.34 to 0.29 mm and increases the average value of reinforcement strain from 1400 to 1880 με, respectively (Fig. 6.14 (b)). These results are in good agreement with previous findings (Frosch et al. 2006) which indicate reducing the bar spacing increases the contribution of the reinforcement on early-age crack-width control in bridge deck slabs subjected to shrinkage.

6.3.8.3 Concrete cover

The effect of increasing the concrete cover from 5 to 85 *mm* on crack control was investigated. Figure 6.15 (a) shows the typical crack pattern occurred at mid-span for all models with different thickness of concrete cover. The results in Fig. 6.15 (b) indicate that, for the GFRP-RC members subjected to axial tension (shrinkage) with different concrete covers, the crack width and the average strain on the bar at crack location remain constant within 0.34~0.35 mm and 1320~1330 με, respectively. The full-depth cracks develop under axial tension (shrinkage) are parallel-sided, which is different from flexural cracks. Therefore, the crack width and strain on the bar at crack location are less dependent on the amount of concrete cover.

6.3.8.4 Reinforcement type

Different types of GFRP and Carbon FRP (CFRP) (sand-coated and ribbed-deformed) can be used as internal reinforcement in bridge deck slabs. The magnitude of crack width depends on

several factors related to reinforcement type such as quality of bond between concrete and reinforcing bars and modulus of elasticity of reinforcement material. In this study, the effect of reinforcing bar type on crack control was investigated using the constructed FEM with a constant reinforcement ratio of $\rho = 0.70\%$. These models had two different FRP types (CFRP and GFRP) with two different bar surface textures (sand-coated and ribbed-deformed). In addition, since the modulus of elasticity of CFRP bars is higher than that of GFRP, four sand-coated CFRP-RC slabs were simulated with reinforcement ratio of 0.35, 0.40, 0.45 and 0.7%, to obtain the minimum ratio to satisfy code requirements.

Figure 6.16 (a and b) shows typical cracking pattern for FEM at the notched mid-span location. Using a reinforcement ratio of 0.70% sand-coated CFRP bars resulted in a final crack width and average bar strain of 0.21 mm and 660 με, respectively (Fig. 6.16 (c and d)). These values were 0.33 mm and 1400 με, respectively, for the counterpart slab with GFRP bars. This was s expected due to lower modulus of elasticity GFRP bars compared to that of CFRP. Nevertheless, the results for crack width and average strain on the bars at crack location (Fig. 6.16 (c and d)) show that the change in bar surface texture (sand-coated to ribbed-deformed bar) has insignificant effect on the results. This may be attributed to the similar bond stress-slippage behavior for sand-coated and ribbed bars (GFRP and CFRP) at low induced stress surrounding the reinforcement in the vicinity of the crack (Malvar et al. 2003 and Alves et al. 2011). The stress surrounding the reinforcement at crack location calculated by Gilbert's model (Gilbert 1992) for sand-coated and ribbed-deformed CFRP bars were 0.73 and 0.74 MPa, respectively. However, this value for sand-coated and ribbed-deformed GFRP bars was 0.62 and 0.63 MPa, respectively.

Test results indicate that primarily width of the crack in the models reinforced with CFRP bars varied depending on the reinforcement ratio crossing the crack. Figure 6.17 shows that increasing the reinforcement ratio from 0.35 to 0.7%, decreased crack width and reinforcement strain at crack location from 0.66 to 0.21 mm and from 2350 to 660 με, respectively. Also, test results indicate that a ratio of 0.45% can control the early-age crack width and reinforcement strain in CFRP-RC bridge deck slabs subjected to shrinkage. In the model reinforced with 0.45% CFRP bars, the maximum crack width and CFRP strain were 0.42 mm and 1890 με, respectively. These values are below the allowable code limit of 0.5 mm and 7650 με (65% of CFRP ultimate strain), respectively (CHBDC 2006).

Table 6.4: Test matrix for the FEM

Name	**Concrete cover (B.&T.)(mm)**	**Concrete strength (28days) (MPa)**	**Reinforcement ratio (%)**	**Bar spacing (mm)**	**Bar type**	**Stage**
SG2	35&25	38	0.5	255	GFR/Sand coated	Verification
SG3			0.7		GFR/Sand coated	
SG4			1.1		GFR/Sand coated	
SS			0.7		Steel/Ribbed	
G.CS.30	35&25	30	0.7	255	GFR/Sand coated	Parametric study Concrete strength
G.CS.40		40				
G.CS.50		50				
G.CS.60		60				
G.CS.70		70				
G.CS.80		80				
G.CC.5	5&5	38	0.7	255	GFR/Sand coated	Parametric study: Concrete cover
G.CC.15	15&15					
G.CC.25	25&25					
G.CC.35	35&35					
G.CC.45	45&45					
G.CC.55	55&55					
G.CC.56	65&65					
G.CC.75	75&75					
G.CC.85	85&85					
G.BS.96	35&25	38	0.7	96	GFR/Sand coated	Parametric study: Bar spacing
G.BS.128				128		
G.BS.153				153		
G.BS.191				191		
C.SC.0.70	35&25	38	0.70	255	CFR/Sand coated	Parametric study: bond type
C.RB.0.70			0.70		CFR/Ribbed bar	
C.SC.0.70			0.70		GFR/Ribbed bar	
G.RB.0.35	35&25	38	0.35	255	CFR/Sand coated	Parametric study: CFRP bar
G.RB.0.40			0.40		CFR/Sand coated	
G.RB.0.45			0.45		CFR/Sand coated	

* Total longitodinal reinforcement ratio, equally, in two layers (top and bottom)

Table 6.5: The predicted shrinkage value for different concrete strength according to the CEB-MC-90/99 model

Concrete strength (MPa)	**Autogenous Shrinkage (με)**	**Drying Shrinkage (με)**	**Total Shrinkage (με)**
30	58	112	170
40	81	100	181
50	104	88	192
60	127	79	206
70	148	70	218
80	168	62	230

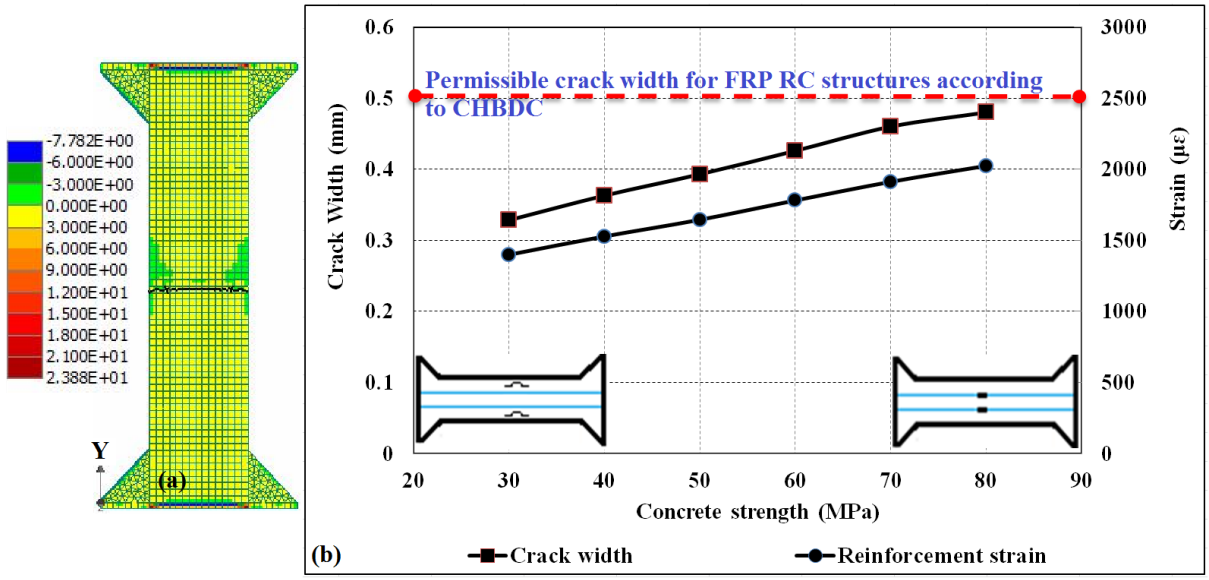

Fig. 6.13: Results of FEM for slabs with different concrete strength, (a) typical concrete stresses in the Y direction (MPa) and cracking pattern ($f_c^{'}$ = 30 MPa), and (b) development of crack width and average reinforcement strain at cracking with time.

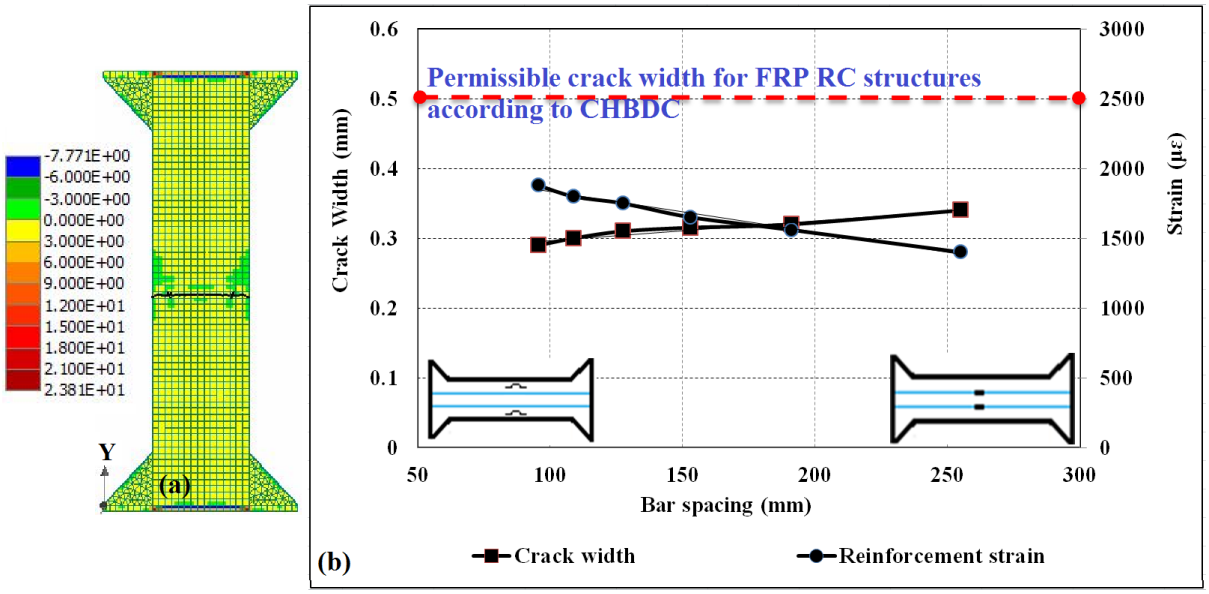

Fig. 6.14: Results of FEM for slabs with different bar spacing: (a) typical concrete stresses in the Y direction (MPa) and cracking pattern (for spacing: 255 mm), and (b) development of crack width and average reinforcement strain at cracking with time.

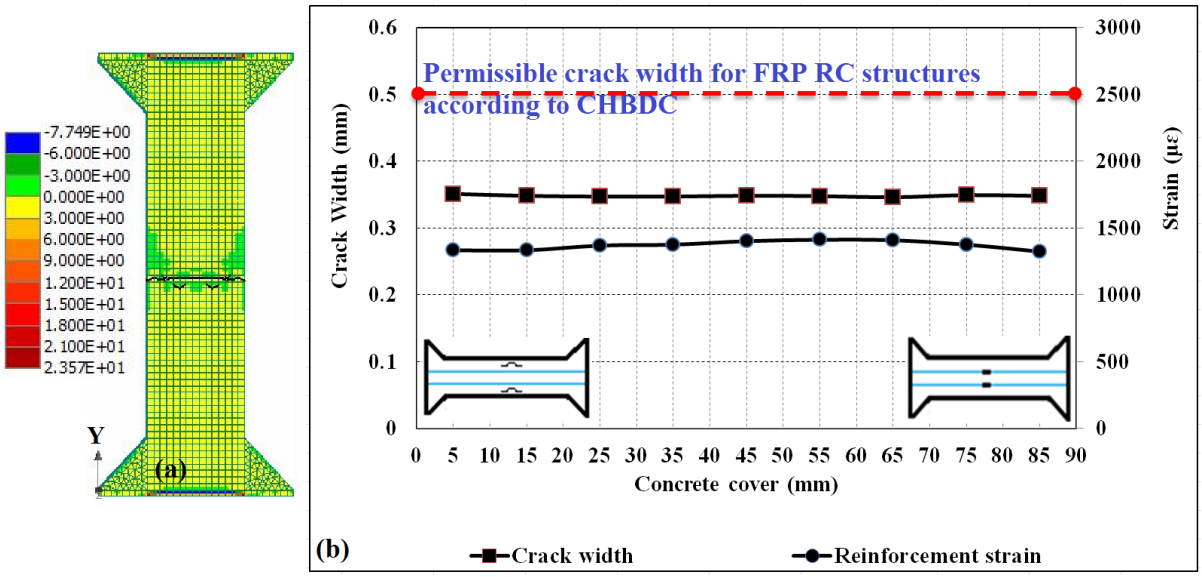

Fig. 6.15: Results of FEM for slabs with different concrete cover: (a) typical concrete stresses in the Y direction (MPa) and cracking pattern (for cover: 5 mm), and (b) development of crack width and average reinforcement strain at cracking with time.

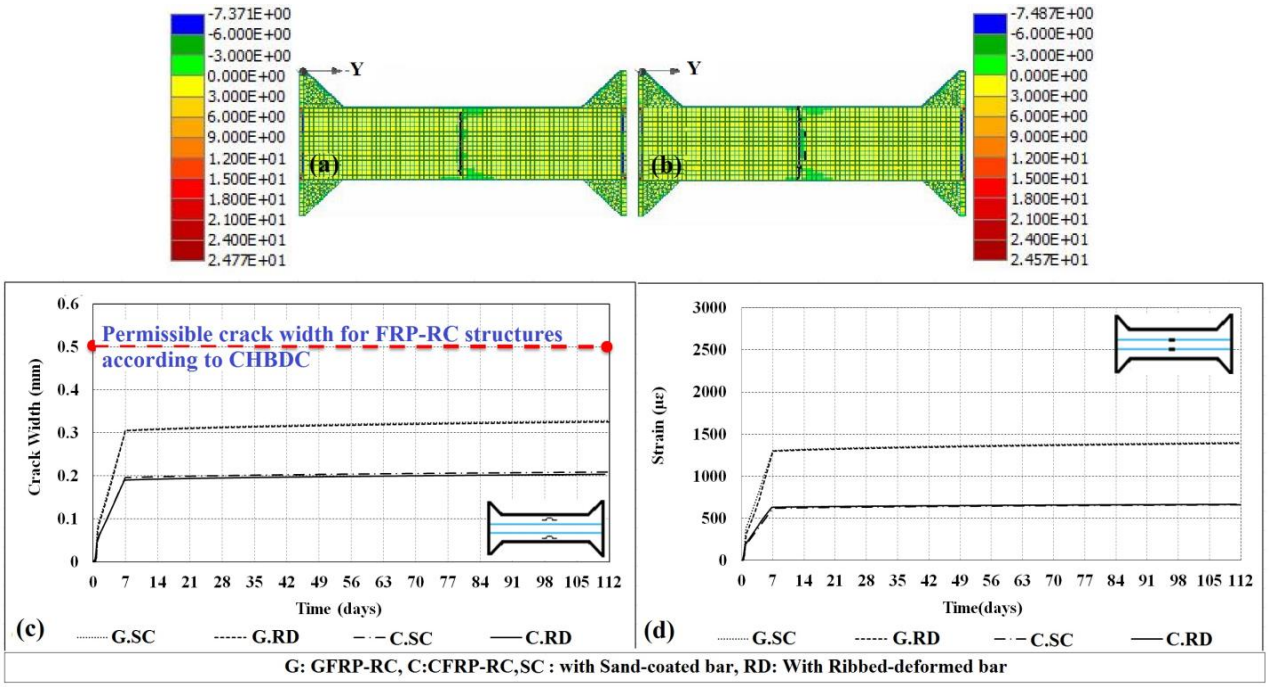

Fig. 6.16: Results of FEM for slabs with different bar type: (a) typical concrete stresses in the Y direction (MPa) and cracking pattern for GFRP, (b) typical concrete stresses in the Y direction (MPa) and cracking pattern for CFRP (c) development of crack width with time, and (d) development of the bar strains at crack location for the FEM.

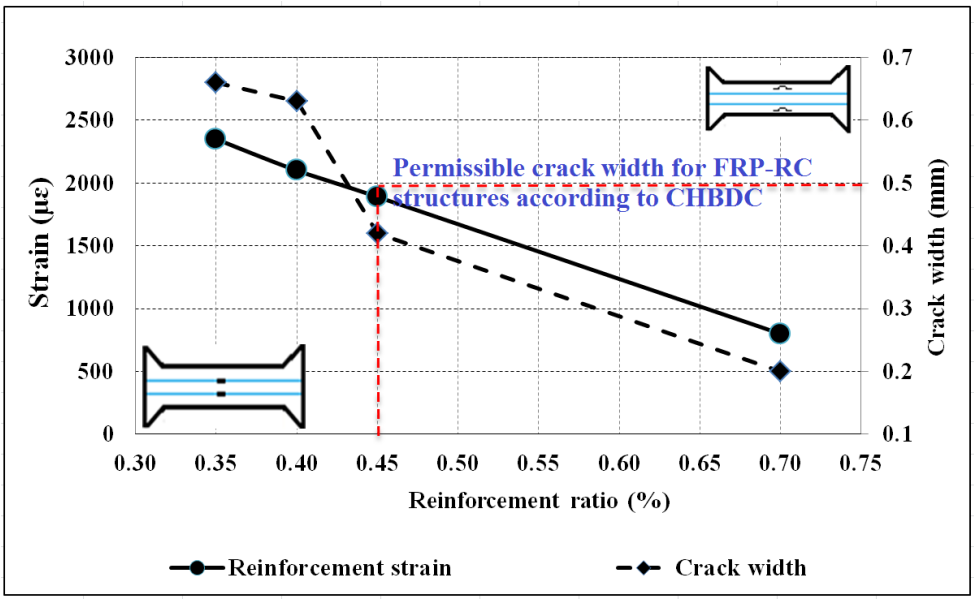

Fig. 6.17: The crack width and average reinforcement strain (Top and Bot.) at cracking location for the FE models reinforced with CFRP bars at 112 days.

CHAPTER7: SUMMARY, CONCLUSIONS AND FUTURE WORK

7.1 SUMMARY

The current thesis investigated the effect of early-age cracking in bridge deck slabs reinforced with GFRP bars subjected to different environmental conditions. The study consisted of two phases: experimental and finite element analysis investigations. The experimental phase study included eight full-size, cast-in-place deck slab prototypes, measuring 2500 mm long × 765 mm wide × 180 mm thick, which were designed to investigate the influence of reinforcement ratio and bar type (GFRP and steel) on transverse early-age cracking in bridge deck slabs under different environmental conditions for a period of 112 days. The tested slabs were divided into two series. Series (I), which included six specimens, was related to slabs investigating the effect of changing the longitudinal reinforcement ratio and bar type subjected to shrinkage under laboratory conditions. Series (II), which included two specimens, investigated the effect of freezing-thawing and wetting-drying cycles on early-age cracking of GFRP-RC bridge deck slabs. Series (I) consisted of five end-restrained RC slabs (SG1, SG2, SG3, SG4 and SS) and one unrestrained/unreinforced; slab F. The five slabs included four GFRP-RC slabs, SG1, SG2, SG3 and SG4, with four different GFRP reinforcement ratios of 0.3, 0.5, 0.7 and 1.1%, respectively, in addition to one steel-RC slab (SS) with a reinforcement ratio of 0.7%. Series (II) included two slabs, G-FT and G-WD, reinforced with the minimum-acceptable reinforcement ratio of 0.7% as obtained from Series (I). Series (II) was tested under freezing-thawing and wetting-drying cycling conditions. All specimens (except slab F) were effectively anchored at their ends by 1473 × 1000 × 1200 mm concrete blocks, which were clamped (pre-stressed) to the laboratory

strong floor. Also, the experimental results were compared to the predictions of a published model (Gilbert 1992) that was originally developed for steel-RC members.

The analytical phase aimed at investigating the effect of different key variables including concrete cover and concrete strength and bar type and spacing on the early-age behavior of FRP-RC bridge deck slabs subjected to shrinkage using a finite element analysis. This phase included constructing a finite element model (FEM) for the bridge deck slabs subjected to shrinkage using ATENA software. The constructed FEM was verified against the experimental results and used to conduct the parametric study.

7.2 CONCLUSIONS

7.2.1 Conclusions from the Experimental Testing of Series (I) Specimens

Based on the experimental variables and laboratory conditions implemented for specimens in Series (I), the following conclusions can be drawn:

1. The longitudinal minimum reinforcement ratio of 0.7%, recommended by CHBDC, can conservatively control the early-age crack width and reinforcement strain for GFRP-RC bridge deck slabs under normal laboratory conditions.
    - In Slab S3 (with 0.7%), the maximum measured crack width and GFRP strain were 0.33 mm and 1520 με, respectively. These values are well below the allowable code limit of 0.5 mm and 5250 με (25% of GFRP ultimate strain), respectively (CHBDC 2006).
    - As the GFRP reinforcement ratio increased, the average crack width at mid-span and strain in GFRP bars decreased. Also, the average strain readings of the instrumented bars (top and bottom) in the vicinity of the crack decreased from 3750 to 1005 με as

the reinforcement ratio increased from 0.3 to 1.1%. These were expected due to the increased concrete section stiffness with the higher reinforcement ratio.

- The concrete internal strain at cracking decreased from 336 to 233 με as the reinforcement ratio increased from 0.3 to 1.1% due to increasing the level of internal restraint.

2. The modulus of elasticity of reinforcement has a significant effect on early-age crack width in RC bridge deck slabs subjected to restrained shrinkage.
    - In specimens SG3 and SS reinforced with GFRP and steel reinforcement ratio of 0.7% under laboratory conditions, the early-age crack width and reinforcement strain at vicinity of the first crack reached to 0.33 and 0.18 mm, and 1520 and 440 με, respectively, after 112 days. Due to lower modulus of elasticity of GFRP bars, the crack width and average reinforcement strain in GFRP-RC bridge deck slabs were two and three times, respectively, larger than the slab reinforced with steel bars.

7.2.2 Conclusions from the Experimental Testing of Series (II) Specimens

Based on the test procedures and environmental conditions adopted in Series (II), the following conclusions can be drawn:

1. The minimum longitudinal reinforcement ratio of 0.7%, recommended by CHBDC, for GFRP-RC bridge deck slabs satisfied the serviceability requirements of CHBDC after being subjected to the simulated exposures of freezing-thawing and wetting-drying cycles.
    - The maximum measured crack width and GFRP strains did not exceed 0.46 mm and 2250 με, respectively. These values are, respectively, less than the allowable code limits of 0.5 mm and 5250 με, which represents 25% of GFRP ultimate strain (CHBDC 2006).

- Under freezing-thawing conditions, the crack width reached its maximum and minimum values at +4 °C (thawing) and -18 °C (freezing), respectively, in each cycle. This behavior is attributed to the volumetric expansion of the critically saturated slab during freezing, which led to partial closure of the crack opening. Upon relieving the expansion pressure during thawing periods, the crack width increased up to 0.42 mm (in the last cycle), which is 40 and 27% higher than the crack width measured before the freezing-thawing exposure and in the specimen subjected to laboratory exposure (slab SG3), respectively.
- In the specimen under wetting-drying conditions, the lower crack width and reinforcement strain recorded during the wetting periods can be attributed to swelling of the slab due to the increase in relative humidity, which led to partial closure of the crack opening. Subsequently, excessive drying shrinkage of the slab increased the crack width and reinforcement strain in the drying period.
- The Ultrasonic Pulse Velocity (UPV) test results show a general reduction of Dynamic Modulus of Elasticity (DME) for the concrete exposed to cyclic conditions, which indicates the existence of fissures and micro-cracks in the cementitious matrix. The Rapid Chloride Penetrability Test (RCPT) and microstructural analysis indicated that the specimens extracted from the slab subjected to wetting-drying cycles yielded relatively higher penetration depths and more internal micro-cracks in the vicinity of the crack location, which signifies that the pore structure was highly interconnected in these specimens. This can be attributed to a higher intensity of micro-cracks due to the matrix fatigue resulting from high strain fluctuations of repetitive swelling and drying shrinkage in the wetting-drying exposure. These results are consistent with the

higher concrete and reinforcement strain values for specimen G-WD exposed to drying conditions.

7.2.3 Conclusions from Numerical Modeling (ATENA and Gilbert's Model)

1. Gilbert's model (Gilbert 1992), to predict width of shrinkage cracks and stresses in reinforcement, can be applied to GFRP-RC deck slabs by modifying the coefficient s_o to 0.8 instead of 1.33, which was originally proposed for steel-RC members.
   - Under laboratory conditions, the measured width of shrinkage cracks and stresses in GFRP agreed with most results from the modified Gilbert's model (Gilbert 1992) within 16% error. The results indicate that more refinement to Gilbert's model is still needed to be fully applicable to FRP-RC slabs (especially for structures reinforced with small bar diameter), which is recommended for future research.
2. Neither the reinforcement surface texture nor the concrete cover had a significant effect on the early-age cracking behavior of FRP-RC bridge deck slabs subjected to shrinkage. However, reducing bar spacing and concrete strength resulted in a decrease in crack width.
   - The constructed FEM was able to analyze FRP-RC bridge deck slabs subjected to restrained shrinkage. The FEM could predict the maximum crack width and the main cracking pattern as well as the strains developed in the reinforcement at the vicinity of the crack to a reasonable degree of accuracy (within 6 to 10% for crack width and reinforcement strain at the crack location, respectively).
   - The results of finite element analysis and experimental study were not consistent in terms of freezing-thawing and wetting-drying cycles, which can be attributed to the effect of internal water expansion and evaporation mechanism due to sub-zero and

elevated (35 °C) temperatures, respectively, which are not considered in the FE concrete material model.

- The results indicate that, in RC bridge deck slabs, increasing concrete strength aggravates early-age cracking. This serviceability issue is attributed to the increased aoutogenous shrinkage and higher induced tensile stresses in the slabs with a higher concrete strength. At 112 days, as concrete strength increased from 30 to 80 MPa, the crack width and reinforcement strain at crack location grew from 0.33 to 0.48 mm and from 1400 to 2020 με, respectively.
- In RC bridge deck slabs subjected to restrained shrinkage, reducing the bar spacing results in simultaneous decrease in crack width and increase in reinforcement strain at crack location. In the FEM with constant reinforcement ratio of 0.7%, decreasing bar spacing from 255 to 96 mm increased the average value of reinforcement strain from 1400 to 1880 με and reduced crack width from 0.34 to 0.29 mm.
- Test results indicate that for the FRP-RC members subjected to axial tension (shrinkage), the crack-width and strain in the bars at crack location are less dependent on the thickness of concrete cover. This is due to the fact that shrinkage cracks are full-depth and parallel-sided.
- Due to the relatively lower modulus of elasticity of GFRP bars, the crack width and average reinforcement strain in GFRP-RC slab were 1.6 and 1.1 times, respectively larger than those of the corresponding slab reinforced with similar CFRP reinforcement ratio of 0.7%. Nevertheless, the results for crack width and average strain in the bars at crack location show that the change in bar surface texture (sand-coated to ribbed-deformed bar) has insignificant effect on the results.

3. The reinforcement ratio of 0.45% CFRP can keep the early age crack width within the allowable limits of the CHBDC (2006).
   - FEM results indicate that a CFRP reinforcement ratio of 0.45% can keep the early-age crack width and reinforcement strain within allowable code limits (CHBDC 2006) of 0.5 mm and 7650 με (65% of CFRP ultimate strain), respectively. This is attributed to the high stiffness of slab section in the CFRP-RC bridge deck slabs.

7.3 Engineering Significance

The reinforcement ratio of 0.7% GFRP can be used as minimum reinforcement for GFRP-RC bridge deck slabs cast with normal strength concrete incorporating 13% silica fume by mass of binder (to stimulate a critical case for early-age shrinkage of concrete). This reinforcement ratio satisfied the serviceability requirements of the CHBDC (CSA 2006) after being subjected to severe environmental conditions. Also, a CFRP reinforcement ratio of 0.45% can keep the early-age crack width and reinforcement strain within allowable code limits (CSA 2006) under normal conditions.

7.4 RECOMMENDATIONS FOR FUTURE WORK

The research findings are extremely useful to the knowledge in this field and can be helpful in the development of Canadian and international codes addressing this subject. Based on the findings and conclusions of the current work, the following recommendations are made for future research:

1. As the present study was carried out using mainly GFRP reinforcement, more experiments should be conducted on slabs reinforced with other FRP reinforcement such as carbon or aramid FRP bars.

2. Further experimental and analytical studies are needed to investigate the behavior of FRP-RC slabs with a wider range of reinforcement ratios, volume-to-surface ratios and slab thicknesses.
3. Since the internal relative humidity plays an important role on early-age behavior of the concrete slabs subjected to freezing-thawing environments, further experimental studies are needed to investigate the early-age cracking in bridge deck slabs subjected to these conditions with different internal relative humidity ranges.
4. Research is further needed to investigate the effect of early-age cracking when longitudinal and transverse FRP reinforcement is used.
5. Admixtures have an effect on the cracking tendencies of concrete structures. The primary admixtures that affect this cracking tendency are water reducers, retarders, accelerators and highly reactive mineral admixtures. More research is needed to study the effect of these admixtures on early-age cracking of bridge deck slabs reinforced with FRP bars.
6. Finite elements results are contradictory to those obtained from the specimens subjected to freezing-thawing and wetting-drying conditions in the experimental study. Therefore, further research is required to provide enough data that could contribute to build a robust FEM under freezing-thawing and wetting-drying environments.

REFERENCES

AASHTO. (2007). "LRFD Bridge Design Specifications." *American Association of State Highway and Transportation Officials (AASHTO)*, Washington, DC, USA.

AASHTO. (1998). "Standard Practice for Estimating the Cracking Tendency of Concrete." *American Association of State Highway and Transportation Officials (AASHTO)*, Washington, DC, USA.

AASHTO . (1997). "Standard Method of Test for Length Change of Hardened Hydraulic Cement Mortar and Concrete." *American Association of State Highway and Transportation Officials (AASHTO)*, Washington, DC, USA.

ACI Committee 318. (2011). "Building Code Requirements for Structural Concrete and Commentary." *American Concrete Institute (ACI 318-11)*, Detroit.

American Concrete Institute (ACI). (2006). "Guide for the Design and Construction of Structural Concrete Reinforced with FRP Bars." *ACI 440.IR-06*, Farmington Hills, MI.

ACI Committee 224. (2001). "Control of Cracking in Concrete Structures." *American Concrete Institute (ACI 224.R-01)*, Washington, DC, USA.

ACI Committee 363. (1998). "Guide to Quality Control and Testing of High Strength Concrete." ACI 363.2R-98, American Concrete Institute, Detroit, MI.

American Concrete Institute (ACI). (2008). "Guide for Modeling and Calculating Shrinkage and Creep in Hardened Concrete." *ACI 209.2R-08*, Farmington Hills, MI.

ASTM Standards (ASTM C 157M-06). (2006). "Standard Test Method for Length Change of Hardened Hydraulic-Cement Mortar and Concrete." *ASTM International (ASTM C 157M-06)*, USA.

ASTM Standards (ASTM C 39/C 39M-05). (2005). "Compressive Strength of Cylindrical Concrete Specimens." *ASTM International (ASTM C 39/C 39M-05)*, USA.

ASTM Standards (ASTM C496M-04). (2004). "Splitting Tensile Strength of Cylindrical Concrete Specimens." *ASTM International (ASTM C496M-04)*, USA.

ASTM Standards (ASTM C 469-02). (2002). "Static Modulus of Elasticity and Poisson's Ratio of Concrete in Compression." *ASTM International (ASTM C 469-02)*, USA.

ASTM C666 M-03, (2008). "Standard Test Method for Resistance of Concrete to Rapid Freezing and Thawing". *ASTM International*, US.

ASTM C597, (2009). "Standard Test Method for Pulse Velocity through Concrete," *ASTM International*, US.

ASTM C1202, (2012). "Standard Test Method for Electrical Indication of Concrete's Ability to Resist Chloride Ion Penetration," *ASTM International*, US.

ASTM A400, (2012). "Standard Practice for Steel Bars, Selection Guide, and Mechanical Properties," *ASTM International*, US.

Alves, J., El-Ragaby, A. and El-Salakawy, E. (2011). "Durability of GFRP Bars Bond to Concrete under Different Loading and Environmental Conditions." *Journal of Composite for Construction, ASCE,* Vol. 15, No. 3, pp. 249-262.

Ayano, T. and Wittmann, F.H. (2002). "Drying, moisture distribution, and Shrinkage of cement-based materials". *Journal of Materials and Structures*, Vol. 35, No. 247, pp. 134-140.

Bassuoni M. T., Nehdi M. L. and Greenough T. R., (2006). "Enhancing the Reliability of Evaluating Chloride Ingress in Concrete Using the ASTM C 1202 Rapid Chloride Penetrability Test," *Journal of ASTM International*, Vol. 3, No. 3, pp. 13.

Bischoff, P. H. and Paixao, R. (2004). "Tension Stiffening and Cracking of Concrete Reinforced with Glass Fibre Reinforced Polymer (GFRP) Bars." *Canadian Journal of Civil Engineering*, Vo. 31, No. 1, pp. 579-588.

Bishnoi, S. (2004). "Strain variations in concrete subjected to cyclic freezing and thawing." MSc Thesis, *Department of civil Eng. of Tokyo University*, Tokyo, Japan.

Bloom, R. and Bentur, A. (1995). "Free and Restrained Shrinkage of Normal and High-Strength Concretes." *ACI Materials Journal*, Vol. 92, No. 2, pp. 211-217.

BNQ NQ 2621-900. (2002). "Determination of the Scaling Resistance of Concrete Surfaces Exposed to Freezing-and-Thawing Cycles in the Presence of De-icing Chemicals," Bureau de normalisation du Québec, Annex A, pp. 19-22.

Brown, M. D., Smith, C. A., Sellers, J. G., Folliard, K. J. and Breen, J. E. (2007). "Use of Alternative Materials to Reduce Shrinkage Cracking in Bridge Decks." *ACI Materials Journal*, Vol. 104, No. 6, pp. 629-637.

Byard, B. E., Schindler, A. K., Barnes, R. W. and Rao, A. (2010). "Cracking Tendency of Bridge Deck Concrete." *Journal of the Transportation Research Board* ,No. 2164, Washington, D.C., pp.122-131.

CEB-FIP. (1990). "Model code for concrete structures." *Comite Europeen du beton*, Paris France.

CEB. (1999). "Structural Concrete-Textbook on Behaviour, Design and Performance. Updated Knowledge of the CEB-FIP Model Code 1990." *fib Bulletin 2, Federation International du Beton*, Lausanne, Switzerland, pp. 37-52.

Cervenka, V. and Niewald, J. (2005). "ATENA-FEMAP User's Guide." Cervenka Consulting Ltd., Prague, Czech Republic.

Cervenka, V., Jendele, L. and Cervenka, J. (2012). "ATENA Program Documentation Part 1: Theory." Cervenka Consulting Ltd., Prague, Czech Republic.

Chariton, T. and Weiss, W. J. (2002). "Using Acoustic Emission to Monitor Damage Development in Mortars Restrained from Volumetric Changes." *Concrete: Material Science to Application, American Concrete Institute*, Vol. 206, No. 1, pp. 205-218.

Cheng, T. T. and Johnson, D. W. (1985). "Incidence Assessment of Transverse Cracking in Bridge Decks: Construction and Material Considerations." *FHWA/NC/85-002*, Raleigh, North Carolina, North Carolina State University, Department of Civil Engineering.

Chen, R. H. and Choi, J. H. (2002). "Effects of GFRP Reinforcing Rebars on Shrinkage and Thermal Stresses in Concrete." *Proceedings of 15th ASCE Engineering Mechanics Conference*, June 4, Columbia University, New York.

Concrete Cracking Workshop. (2005). http://acbm.northwestern.edu/ccw.html.

CSA (CSA/S806-12). (2012). "Design and Construction of Building Structures with Fibre-Reinforced Polymers." *A National Standard of Canada (CSA/S806-12)*, Canadian Standards Association. Toronto, Ontario, Canada.

Canadian Standards Associations (CSA). (2006). "Canadian Highway Bridge Design Code-CHBDC." *CAN/CSA-S6-06,* 2nd Edition, Rexdale, Ontario, Canada.

CSA (CSA/A23.1-04). (2004). "Concrete Materials and Methods of Concrete Construction." *A National Standard of Canada (CSA/A23.1-04),* Canadian Standards Association, Mississauga, Ontario, Canada.

CSA (CSA/A23.3-04). (2004). "Design of Concrete Structures." *A National Standard of Canada (CSA/A23.3-04),* Canadian Standards Association, Ontario, Canada.

Chen, R. H. and Choi, J.-H. (2002). "Effects of GFRP Reinforcing Rebars on Shrinkage and Thermal Stresses in Concrete," *Proceedings of 15th ASCE Engineering Mechanics Conference,* June 4, Columbia University, New York. pp. 1-8.

Cusick, R. W. and Kesler, C. E. (1980). "Behavior of Shrinkage-Compensating Concretes Suitable for Use in Bridge Decks." *American Concrete Institute (ACI SP64-15),* Vol. 64, No.1, pp. 293-310.

Dakhil, F. H., Cady, P. D. and Carrier, R. E. (1975). "Cracking of fresh concrete as related to reinforcement," *American Concrete Institution journal, ACI,* Vol. 72, No. 8, pp.421-428.

Darwin, D., Browning, J. and Lindquist, W. D. (2004). "Control of Cracking in Bridge Decks: Observations from the Field." *Cement, Concrete, and Aggregates*, Vol. 26, pp. 148-154.

Ducret, J., Lebet, J. and Monney, C. (1997). "Hydration effect and deck cracking during the construction of steel composite bridges." *Proceedings, ICOM- Construction conference*, Article 359.

El-Ragaby, A. (2007). "Fatigue Behaviour of Concrete Bridge Deck Slabs Reinforced with Glass FRP Bars." *Doctor of Philosophy Thesis in Civil Engineering*, University of Sherbrook, Quebec, Canada.

Favre, R. (1983). "Fissuration et deformations." *Manual du Comité Euro-Internationale du Beton (CEB). Ecole Polytechnique Federale de Lausanne,* Swizerland, pp. 249.

Folliard, K., Smith, C., Sellers, G., Brown, M. and Breen, J. E. (2003). "Evaluation of Alternative Materials to Control Drying Shrinkage Cracking in Concrete Bridge Decks." *E-port No: FHWA/TX-04/0-4098-4, Center for Transportation Research*, University of Texas at Austin.

French, C., Laurice, E., Le, Q. and Hajjar, J. F. (1999). "Transverse Cracking in Concrete Bridge Decks." *Transportation Research Record 1688 (TRB),* Washington, D. C.

Frosch, R. J. (1999). "Another Look at Cracking and Crack Control in Reinforced Concrete." *American Concrete Institution journal,* ACI, Vol. 96, pp. 437-442.

Frosch, R. J., Blackman, D. T. and Radabaugh, R. D. (2003). "Investigation of Bridge Deck Cracking in Various Bridge Superstructure Systems." *Joint Transportation Research Program*, E-port No: FHWA/IN/JTRP-2002/25, Department of Transportation and Purdue University, West Lafayette, Indiana.

Frosch, R., Brice, J. and Ericson, J. (2006). "Design methods for the Control of Restrained Shrinkage Cracking." *Joint Transportation Research Program,* Project no. C-36-56MMM, File no. 7 4-63. Final Report.

Fung, R. (2002). "HPC Bridges in Canada." *HPC Bridge Views*, Issue No. 24.

Ghatefar, A., El-Salakawy, E. and Bassuoni, M. (2014). "Effect of Reinforcement Ratio on Transverse Early-Age Cracking of GFRP-RC Bridge Deck Slabs." *Journal of Composite for Construction, ASCE,* Vol. 18, No. 6, DOI: 10.1061/ (ASCE) CC.1943-5614.0000479.

Gardner, N. J. and Tsuruta, H., (2004). "Is Superposition of Creep Strains Valid for Concretes Subjected to Drying Creep?" *ACI Materials Journal*, Vo. 101, No. 5, pp. 409-415.

Gilbert, R. I. (1992). "Shrinkage Cracking in Fully Restrained Concrete Members." *ACI Structural Journal*, Vol.89, No. 2, pp. 141-149.

Gruner, P. W. and Plain, G. A. (1993). "Type K Shrinkage-Compensating Cement in Bridge Deck Construction." *Concrete International Journal*, Vol. 5, No. 10, pp. 44-47.

Hadidi, R. and Saadeghvaziri, M. A. (2005). "Transverse Cracking of Concrete Bridge Decks: State-of-the-Art." *Journal of Bridge Engineering, ASCE,* Vol. 10, No. 5, pp. 503-510.

Hillerborg, A., Modeer M. and Peterson, P. E. (1976). "Analysis of crack formation and crack growth in concrete by means of fracture mechanics and finite elements." *Cement Concrete Research journal*, Vol. 6, No. 8, pp. 773-782.

Hordijk, D. A. (1991). "Local approach to fatigue of concrete." Ph.D thesis, Delft University of Technology, Delft.

Holt, E. E. and Leivo, M. T. (2000). "Methods of Reducing Early Age Shrinkage." *VTT building Technology Conference proceeding*, Technical Research Centre of Finland, PRO 17, pp. 435-447.

ISIS Canada. (2007). "Reinforcing Concrete Structures with Fibre Reinforced Polymers." *The Canadian Network for Centers of Excellence on Intelligent Sensing for Innovative Structures (ISIS-M03-07).* Winnipeg, MB, Canada.

ISIS Canada. (2006). "Durability of Fiber Reinforced Polymers in Civil Infrastructure." Durability Monograph, the Canadian Network for Centers of Excellence on Intelligent Sensing for Innovative Structures (ISIS), Winnipeg, MB. Canada.

Issa, M. A. (1999). "Investigation of Cracking in Concrete Bridge Decks at Early Ages." *Journal of Bridge Engineering, ASCE*, Vol. 4, No. 4, pp. 116-124.

Jaber, T. and Ardani, A. (2004). "HPC and FRP for Colorado Bridge Deck." *HPC Bridge Views*, Issue No. 35.

Koenigsfeld, D. and Myers, J. J. (2003). "Secondary Reinforcement for Fibre Reinforced Polymers Reinforced Concrete Panels." *Center for Infrastructure Engineering Studies (CIES 03-45)*, University of Missouri, Missouri, Rolla.

Krauss, P. D. and Rogalla, E. A. (1996). "Transverse Cracking in Newly Constructed Bridge Decks." Transportation Research Board Business Office, *National Research Council NCHRP Report No*. 380, Washington, USA.

Laoubi, K., El-Salakawy, E. and Benmokrane, B. (2006). "Creep and durability of sand-coated glass FRP bars in concrete elements under freeze/thaw cycling and sustained loads". *Journal of Concrete and Composites,* Vol. 10, No. 28, pp. 869-878.

Li, Z., Qi, M., Li, Z. and Ma, B. (1999). "Crack Width of High-Performance Concrete due to Restrained Shrinkage." *Journal of Materials in Civil Engineering*, Vol. 11, No. 3, pp. 214-223.

Lopez, M., Kahn, L. F. and Kurtis, K. E. (2008). "Effect of Internally Stored Water on Creep of High Performance Concrete." *ACI Materials Journal*, Vol. 105, No. 1, pp. 265-273.

MacGregor, J. G. and Wight, J. K. (2005). "Reinforced Concrete: Mechanics and Design." *Prentice-Hall Inc*., Englewood Cliffs, NJ. 4th Edition. New Jersey.

Mady, M. H. A. (2011). "Seismic Behaviour of Exterior Beam-Column Joints Reinforced with FRP bars and Stirrups." *Ph.D. Thesis*, Department of Civil Engineering, University of Manitoba, Winnipeg, Manitoba.

Malvar, L. J., Cox, J. V. and Cochran, K.B. (2003). "Bond between carbon fiber reinforced polymer bars and concrete. I: Experimental study." *Journal of composite for construction, ASCE*, Vol. 7, No. 2, pp. 154-163.

Mehta, P. K. and Montherio, P. J. M. (2014). "Concrete (microstructure, properties, and materials)." Book, *MC Graw Hill*, New York, NY, USA.

Mokarem, D. W., Meyerson, R. M. and Weyers, R. E. (2003). "Development of Concrete Shrinkage Performance Specifications." *Report No: VTRC 04-CR1*. Virginia Transportation Research Council.

Minnetyan, L. (2011). "Tool for Analysis of Early Age Transvers Cracking of Composite Bridge decks." *Joint Transportation Research Program,* Project no. SPR-06-37(C-06-37), Final report. Clarkson University, New York, NY, USA.

Muller, H. S.; Bažant, Z. P. and Kuttner, C. H., (1999). "Data Base on Creep and Shrinkage Tests." *Rilem Subcommittee 5 Report RILEM TC 107-CSP*, RILEM, Paris.

Myers, C. (1982). "Survey of cracking on underside of classes B-1 and B-2 concrete bridge decks in district 4." *Investigation No. 82-2*, Division of Material and Research, Missouri Highway and Transportation Department, Jefferson, Missouri, USA.

NCHRP Synthesis of Highway Practice 333. (2004). "Concrete Bridge Deck Performance." *Transportation Research Board*, Washington, D.C.

Newman, J. and Choo, B. S. (2003). "Advanced Concrete Technology" Book, *Butterworth-Heinemann (Elsevier),* Oxford, UK.

Nevillle, A. M., (2011). "Properties of Concrete." *Book,* Pearson publisher, New York, NY, USA

Pease, B. J., Shah, H. R. and Weiss, W. J. (2005). "Shrinkage Behavior and Residual Stress Development in Mortar Containing Shrinkage Reducing Admixture (SRA)." *Shrinkage and Creep of Concrete (ACI),* Vol. 227, No. 1, pp. 285-230.

Petrou, M. F., Harries, K. A. and Schroeder, G. E. (2001). "Field Investigation of High-Performance Concrete Bridge Decks in South Carolina." Transportation Research Record 1770, pp. 12-19.

Powers, T. C. and Brownyard, T. L. (1947). "Studies of the Physical Properties of Hardened Portland Cement Paste - Part 5: Studies of the Hardened Paste by Means of Specific-Volume Measurements." *ACI Journal, Proceedings*. Vo. 43, No.1, pp. 249-336.

Pultrall Inc., "V-ROD^{TM}-Technical data sheet, " *ADS Composites Group Inc.*, Thetford Mines, Quebec, Canada, 2012. http://www.pultrall.com (visited on October 15, 2012).

RILEM Technical Committee, (1988), "Material Models for Structural Creep Analysis." Chapter 2 in Mathematical Modeling of Creep and Shrinkage of Concrete, pp. 99-215, New York.

Ramey, G. E., Pittman, D. W. and Webster, G. K. (1999). "Shrinkage-Compensating Concrete for Bridge Decks." *Concrete International Journal*, Vol. 21, No. 4, pp. 29-34.

Ramey, G. E., Wolff, A. R. and Wright, R. L. (1997). "Structural Design Actions to Mitigate Bridge Deck Cracking." *Practice Periodical Structural Design and Construction*, Vol. 2, No. 3, pp. 118-124.

Saadeghvaziri, M. A. and Hadidi, R. (2005). "Transverse Cracking of Concrete Bridge Decks: Effects of Design Factors." *Journal of Bridge Engineering (ASCE)*, Vol. 10, No. 1, pp. 511-519.

Shing, P. B. and Xi, Y. (2003). "Studies on the Use of High-Performance Concrete and FRP Reinforcement for the I-225/Parker Road Bridge." *Report No. CDOT-DTD-R-2003-13*. Colorado Department of Transportation.

Scherer, W., Chen, J., Valenza, J. (2002). "Method of Protecting Concrete from Freeze Damage." U.S. Patent No. 6485-560.

Sooriyaarachchi, H., Polakoutas, k. and Byars, F. (2005). "Tension stiffening Behavior of GFRP-Reinforced Concrete." *7th International Symposium on Fiber-Reinforced polymer (FRP) Reinforcement for concrete structures (FRPRCS-7), 6-9 November*, Kansas, Missouri, pp. 975-990.

Soudli, K., El-Salakawy, E. and Craig, B. (2007). "Behavior of CFRP Strengthened Reinforced Concrete Beams in Corrosive Environment." *Journal of Composites for Construction, (ASCE*), Vol. 11, No. 1, pp. 291-298.

Tangtermsirikul, S. and Sudsangiam. (1995). "Class C Fly Ash as a Shrinkage Reducer for Cement Paste." *5th International Conference*, Milwaukee, Wisconsin, USA.

TRB. (2006). "Control of Cracking in Concrete-State of the Art." *Transportation Research Circular E-C107*, Transportation Research Board of the National Academic, Basic research and emerging technologies related concrete committee, New York, NY, USA.

Towers, T.C., and Helmuth, R.A. (2008). "Theory of Volume Changes in Hardened Portland-Cement Paste during Freezing"., *American Concrete Institution (ACI). Special Publication*, SP-249, pp. 141-160.

Turton, C. (1981). "Plastic Cracking of Concrete." Paper for publication PP/284, *Cement and Concrete Association*, Vol. 2, No.1, pp. 365-375.

U.S. Army Corps of Engineers. (1981). "Test Method for Coefficient of Linear Thermal Expansion of Concrete." *CRD C 39-81, issued 1 June 1981*. Available at: http://www.wes.army.mil/SL/MTC/handbook/crd_c39.pdf.

Weiss, W. J., Yang, W. and Shah, S. P. (1998). "Shrinkage Cracking of Restrained Concrete Slabs" *Journal of Engineering Mechanics*, Vol. 124, No. 7, pp. 765-774.

Weng, J. K., Langan, B. and Ward, M. (1997). "Pozzolanic reaction in portland cement, silica fume and fly ash mixtures." *Canadian Journal of Civil Engineering*, Vol. 24, No. 1, pp. 754-760.

Weyers, R. E., Conway, J. C. and Cady, P. D. (1982). "Photo-Elastic Analysis of Rigid Inclusions in Fresh Concrete." *Cement and Concrete Research*, Vo.12, No. 4, pp. 475-484.

Whiting, D. A., Detwiler, R. J. and Lagergren, E. S. (2000). "Cracking Tendency and Drying Shrinkage of Silica Fume Concrete for Bridge Deck Applications." *Materials Journal (ACI),* Vol. 97, No. 1, pp. 71-77.

Xi, Y., Shing, B., Abu-Hejleh, N., Asiz, A., Suwito and Xie, Z. (2003). "Assessment of the Cracking Problem in Newly Constructed Bridge Decks in Colorado." *Report No. CDOT-DTD-R- 2003-3*. Colorado Department of Transportation-Research.

Zhang, J., Gao, Y., Han, Y. and Sun, W. (2012). "Shrinkage and Interior Humidity of Concrete under Dry–Wet Cycles." *An International Journal of Drying Technology of Bridge Engineering,* Vol. 30, No. 6, pp. 583-596.

APPENDIX A

SHRINKAGE PREDICTION MODELS

A-1: DIFFERENT SHRINKAGE PREDICTION MODELS

ACI 209.2R-08 recommended to use the following method to predict time dependent shrinkage in the concrete; ACI 209R-92 (ACI Committee 209 1992), Bažant-Baweja B3 (Bažant and Baweja 1995, 2000), CEB MC90-99 (Muller and Hillsdorf 1990; CEB 1991, 1993, 1999), and GL2000 (Gardner and Lockman 2001). According the parameter ranges for each model (Table App.1), ACI 209.2R-8, Bažant-Baweja B3, and GL200 can be used for the curing time of 1 day. The other methods predict the shrinkage of the concrete with curing time at least 14 days. Nevertheless CEB MC90-99 has been adjusted to take into account the particular characteristics of concrete strength (for high concrete strength).

Table A-1: Parameter ranges of each model

Input variables	ACI 209R-92	Bažant-Baweja B3	GL2000	CEB MC90-99
f_{cm28} (MPa)	—	17 to 70	16 to 82	15 to 120
a/c	—	2.5 to 13.5	—	—
Cement content (kg/m^3)	279 to 446	160 to 720	—	—
w/c	—	0.35 to 0.85	—	—
Relative humidity (%)	40 to 100	41 to 100	20 to 100	40 to 100
Type of cement	I,II	I,II,III	I,II,III	I,II,III
Moist cured	≥ 1 days	≥ 1 days	≥ 1 days	≥ 14 days
Steam cured	1 to 3 days	—	—	—
Loading time	≥ 7 days	≥ 1 days	≥ 1 days	≥ 1 days

a/c: air to cement ratio, *w/c*: water to cement ratio, f_{cm28}: concrete compressive strength in 28 days.

In this research the following input values were used to predict the amount of shrinkage (Table A-2):

Table A-2: Input values for theoretical equations to predict shrinkage

Thickness	mm	180
Specified 28-day strength f'c	$f'_{c\,(MPa)}$	38
Ambient relative humidity	h (%)	70
Temprature	T (^{0}C)	20
Valume /surface	V/S (mm)	180
Shape	-	Infinite Slab
Curing time	T_c (days)	1
Curing conditions	-	air
Age at loading	T_0 (days)	1
Applied stress range	k_s (%)	40
Cement type	GU	I
Max agg. Size	mm	20
Cement content	c (kg/m^3)	420
Water content	w (kg)	170
water-cement ratio	w/c	0.40
Aggregate-cement ratio	a/c	4
Fine agg. Percentage	ψ (%)	40
Air content	α (%)	6
Slump	s (mm)	140
Unit weight of concrete	γ_c (kg/m^3)	2450

A-1.1 ACI 209R-92 Model Solution:

Nominal ultimate shrinkage strain $\varepsilon_{shu} = 780 \times 10^{-6}$

Moist curing correction factor $\gamma_{sh,tc} = 1.202 - 0.2337\log(tc)$

Ambient relative humidity factor $\gamma_{sh,RH} = 1.40 - 1.02h$

Volume-to-surface ratio factor $\gamma_{sh,vs} = 1.2e^{[-0.00472(V/S)]}$

Slump of fresh concrete factor $\gamma_{sh,s} = 0.89 + 0.00161$

Fine aggregate factor $\gamma_{sh,\psi} = 0.30 + 0.014\psi$ if $\psi \leq 50\%$

Cement content factor $\gamma_{sh,c} = 0.75 + 0.00061c$

Air content factor $\gamma_{sh,\alpha} = 0.95 + 0.008\alpha \geq 1$

Cumulative correction factor $\gamma_{sh} = \gamma_{sh,tc} \times \gamma_{sh,RH} \times \gamma_{sh,vs} \times \gamma_{sh,s} \times \gamma_{sh,\psi} \times \gamma_{sh,c} \times \gamma_{sh,\alpha}$

Ultimate shrinkage strain $\varepsilon_{shu} = 780\gamma_{sh} \times 10^{-6}$

Shrinkage time function $f_{(t,tc)} = [(t - tc)^{\alpha}/(f + (t - tc)^{\alpha})]$

A-1.2 Bažant-Baweja B3 Model Solution

Ambient relative humidity factor $k_h = 12.74 - 12.94h$ if $0.98 < h < 1$

Cement type factor $\alpha_1 = 1$

Curing condition factor $\alpha_2 = 1$

Nominal ultimate shrinkage $\varepsilon_{s\infty} = -\alpha_1\alpha_2 [0.019^{w2.1} f_{cm28}^{-0.28} + 270] \times 10^{-6}$

Member shape factor $k_s = 1$

Shrinkage half-time $\tau_{sh} = 0.085t_c - 0.08f_{cm28} - 0.25 [2k_s (V/S)]$ 2

Time dependence factor $E_{cm607}/E_{cm(tc+\tau sh)} = 1.0805/[(t_c + \tau_{sh})/(4 + 0.85(t_c + \tau_{sh}))]^{0.5}$

Ultimate shrinkage strain $\varepsilon_{sh\infty} = -\varepsilon_{s\infty} E_{cm607}/E_{cm(tc+\tau sh)}$

Shrinkage time function $S(t - t_c) = tanh[(t - t_c)/\tau_{sh}]^{0.5}$

Shrinkage strains $\varepsilon_{sh}(t,tc) = -\varepsilon_{sh\infty} k_h tanh[(t - t_c)/\tau_{sh}]^{0.5}$

A-1.3 GL2000 model solution

Cement type factor $k = 1$

Ultimate shrinkage strain

Ambient relative humidity factor $\beta(h) = (1 - 1.18h_4)$

Shrinkage time function $\beta(t - t_c) = [(t - t_c)/\{t - t_c + 0.12(V/S)^2\}]^{0.5}$

Shrinkage strains $\varepsilon_{sh}(t,tc) = \varepsilon_{shu}\beta(h)\beta(t - t_c)$

A-1.4 CEB MC90-99 model solution:

Autogenous shrinkage $\varepsilon_{cas}(t)$+ Drying shrinkage $\varepsilon_{cds}(t,t_c)$

$\varepsilon_{sh}(t,tc)$ $\varepsilon_{sh}(t,tc) = \varepsilon_{cas}(t) + \varepsilon_{cds}(t,tc)$

a) Autogenous shrinkage $\varepsilon_{cas}(t)$

Cement type factor $\alpha_{as} = 700$

Notional autogenous shrinkage $\varepsilon_{caso}(f_{cm28}) = -\alpha_{as}[(f_{cm28}/f_{cmo})/\{6 + (f_{cm28}/f_{cmo})\}]^{2.5} \times 10^{-6}$

Autogenous shrinkage time function $\beta_{as}(t) = 1 - exp[-0.2(t/ti)^{0.5}]$

Autogenous shrinkage strains $\varepsilon_{cas}(t) = \varepsilon_{caso}(f_{cm28})\beta_{as}(t)$

b) Drying shrinkage $\varepsilon_{cds}(t,t_c)$

Cement type factors $\alpha_{ds1} = 4$ $\alpha_{ds2} = 0.12$

Notional drying shrinkage coefficient $\varepsilon_{cdso}(f_{cm28}) = [(220 + 110\alpha_{ds1})exp(-\alpha_{ds2}\, f_{cm28}/f_{cmo})] \times 10^{-6}$

Ambient relative humidity factor $\beta_{RH(h)} = -1.55[1 - (h/h_o)^3]$ *for* $0.4 \le h < 0.99$ β_{s1} *where* $\beta_{s1} = [3.5f_{cmo}/f_{cm28}]^{0.1} \le 1.0$

Drying shrinkage time function $\beta_{ds}(t - t_c) = [\{(t - t_c)/1\}/\{350([(V/S)/(V/S)_o]2 + (t - t_c)/t_i\}]^{0.5}$

Drying shrinkage strains $\varepsilon_{cds}(t,t_c) = \varepsilon_{cdso}(f_{cm28})\beta_{RH}(h)\beta_{ds}(t - t_c)$

Table App. 3 shows the calculated shrinkage value according to different model solutions. While Table App. 4 represent calculated shrinkage value used in the analytical section for different concrete strength of 20, 30, 40, 50, 60, 70 and 80 GPa.

Table A-3: The calculated shrinkage value according to different model solutions

t (days)	ACI 209R-92	Bažant-Baweja B3	GL2000	Average
1	0.00E+00	0.00E+00	0.00E+00	0.00E+00
2	-1.76E-06	-1.84E-05	-2.11E-05	-1.38E-05
3	-3.52E-06	-2.61E-05	-2.98E-05	-1.98E-05
4	-5.26E-06	-3.19E-05	-3.65E-05	-2.45E-05
5	-7.00E-06	-3.68E-05	-4.21E-05	-2.86E-05
6	-8.72E-06	-4.11E-05	-4.70E-05	-3.23E-05
7	-1.04E-05	-4.50E-05	-5.15E-05	-3.56E-05
8	-1.21E-05	-4.86E-05	-5.55E-05	-3.88E-05
9	-1.38E-05	-5.19E-05	-5.93E-05	-4.17E-05
10	-1.55E-05	-5.51E-05	-6.29E-05	-4.45E-05
11	-1.72E-05	-5.80E-05	-6.62E-05	-4.71E-05
12	-1.89E-05	-6.08E-05	-6.94E-05	-4.97E-05
13	-2.05E-05	-6.35E-05	-7.24E-05	-5.21E-05
14	-2.22E-05	-6.60E-05	-7.53E-05	-5.45E-05
15	-2.38E-05	-6.85E-05	-7.81E-05	-5.68E-05
16	-2.54E-05	-7.09E-05	-8.07E-05	-5.90E-05
17	-2.70E-05	-7.31E-05	-8.33E-05	-6.12E-05
18	-2.86E-05	-7.54E-05	-8.58E-05	-6.33E-05
19	-3.02E-05	-7.75E-05	-8.82E-05	-6.53E-05
20	-3.18E-05	-7.96E-05	-9.05E-05	-6.73E-05
21	-3.34E-05	-8.16E-05	-9.28E-05	-6.93E-05
22	-3.50E-05	-8.36E-05	-9.50E-05	-7.12E-05
23	-3.65E-05	-8.55E-05	-9.72E-05	-7.31E-05
24	-3.81E-05	-8.74E-05	-9.93E-05	-7.49E-05
25	-3.96E-05	-8.92E-05	-1.01E-04	-7.67E-05
26	-4.12E-05	-9.10E-05	-1.03E-04	-7.85E-05
27	-4.27E-05	-9.27E-05	-1.05E-04	-8.02E-05
28	-4.42E-05	-9.45E-05	-1.07E-04	-8.20E-05
90	-1.24E-04	-1.66E-04	-1.85E-04	-1.59E-04
91	-1.26E-04	-1.67E-04	-1.86E-04	-1.60E-04
92	-1.27E-04	-1.68E-04	-1.87E-04	-1.60E-04
93	-1.28E-04	-1.69E-04	-1.88E-04	-1.61E-04
94	-1.29E-04	-1.69E-04	-1.89E-04	-1.62E-04
108	-1.44E-04	-1.80E-04	-2.00E-04	-1.75E-04
109	-1.45E-04	-1.81E-04	-2.01E-04	-1.76E-04
110	-1.46E-04	-1.82E-04	-2.02E-04	-1.76E-04
111	-1.47E-04	-1.83E-04	-2.03E-04	-1.77E-04
112	-1.48E-04	-1.83E-04	-2.04E-04	-1.78E-04

Table A-4: The calculated shrinkage value according to different concrete compressive strength (CEB MC90-99 model solution)

	***f'(c)* (MPa)**					
Time (days)	**30**	**40**	**50**	**60**	**70**	**80**
0	0	0	0	0	0	0
1	-1.19E-05	-1.67E-05	-2.15E-05	-2.61E-05	-3.05E-05	-3.46E-05
2	-1.61E-05	-2.27E-05	-2.92E-05	-3.55E-05	-4.14E-05	-4.70E-05
3	-1.92E-05	-2.70E-05	-3.47E-05	-4.22E-05	-4.92E-05	-5.59E-05
4	-2.16E-05	-3.04E-05	-3.91E-05	-4.75E-05	-5.54E-05	-6.29E-05
5	-2.36E-05	-3.32E-05	-4.28E-05	-5.19E-05	-6.06E-05	-6.88E-05
6	-2.54E-05	-3.57E-05	-4.59E-05	-5.58E-05	-6.51E-05	-7.39E-05
7	-2.69E-05	-3.79E-05	-4.87E-05	-5.92E-05	-6.91E-05	-7.84E-05
8	-3.97E-05	-4.99E-05	-6.02E-05	-7.02E-05	-7.97E-05	-8.87E-05
9	-4.57E-05	-5.59E-05	-6.62E-05	-7.62E-05	-8.58E-05	-9.49E-05
10	-5.04E-05	-6.07E-05	-7.11E-05	-8.12E-05	-9.10E-05	-1.00E-04
11	-5.45E-05	-6.49E-05	-7.54E-05	-8.57E-05	-9.56E-05	-1.05E-04
12	-5.82E-05	-6.86E-05	-7.93E-05	-8.97E-05	-9.98E-05	-1.09E-04
13	-6.15E-05	-7.20E-05	-8.28E-05	-9.34E-05	-1.04E-04	-1.13E-04
14	-6.46E-05	-7.52E-05	-8.61E-05	-9.68E-05	-1.07E-04	-1.17E-04
15	-6.74E-05	-7.82E-05	-8.92E-05	-1.00E-04	-1.11E-04	-1.21E-04
16	-7.01E-05	-8.10E-05	-9.21E-05	-1.03E-04	-1.14E-04	-1.24E-04
17	-7.27E-05	-8.36E-05	-9.48E-05	-1.06E-04	-1.17E-04	-1.27E-04
18	-7.51E-05	-8.61E-05	-9.74E-05	-1.09E-04	-1.19E-04	-1.30E-04
19	-7.74E-05	-8.85E-05	-9.99E-05	-1.11E-04	-1.22E-04	-1.33E-04
20	-7.96E-05	-9.07E-05	-1.02E-04	-1.14E-04	-1.25E-04	-1.35E-04
21	-8.17E-05	-9.29E-05	-1.04E-04	-1.16E-04	-1.27E-04	-1.38E-04
22	-8.37E-05	-9.50E-05	-1.07E-04	-1.18E-04	-1.29E-04	-1.40E-04
23	-8.57E-05	-9.70E-05	-1.09E-04	-1.20E-04	-1.32E-04	-1.43E-04
24	-8.76E-05	-9.90E-05	-1.11E-04	-1.22E-04	-1.34E-04	-1.45E-04
25	-8.94E-05	-1.01E-04	-1.13E-04	-1.25E-04	-1.36E-04	-1.47E-04
26	-9.12E-05	-1.03E-04	-1.15E-04	-1.26E-04	-1.38E-04	-1.49E-04
27	-9.29E-05	-1.04E-04	-1.16E-04	-1.28E-04	-1.40E-04	-1.51E-04
28	-9.46E-05	-1.06E-04	-1.18E-04	-1.30E-04	-1.42E-04	-1.53E-04
29	-9.62E-05	-1.08E-04	-1.20E-04	-1.32E-04	-1.44E-04	-1.55E-04
30	-9.78E-05	-1.09E-04	-1.22E-04	-1.34E-04	-1.45E-04	-1.57E-04
31	-9.93E-05	-1.11E-04	-1.23E-04	-1.35E-04	-1.47E-04	-1.59E-04
32	-1.01E-04	-1.12E-04	-1.25E-04	-1.37E-04	-1.49E-04	-1.60E-04
33	-1.02E-04	-1.14E-04	-1.26E-04	-1.38E-04	-1.50E-04	-1.62E-04
34	-1.04E-04	-1.15E-04	-1.28E-04	-1.40E-04	-1.52E-04	-1.64E-04
35	-1.05E-04	-1.17E-04	-1.29E-04	-1.42E-04	-1.54E-04	-1.65E-04
36	-1.06E-04	-1.18E-04	-1.31E-04	-1.43E-04	-1.55E-04	-1.67E-04

37	-1.08E-04	-1.20E-04	-1.32E-04	-1.44E-04	-1.56E-04	-1.68E-04
38	-1.09E-04	-1.21E-04	-1.33E-04	-1.46E-04	-1.58E-04	-1.70E-04
39	-1.10E-04	-1.22E-04	-1.35E-04	-1.47E-04	-1.59E-04	-1.71E-04
40	-1.12E-04	-1.23E-04	-1.36E-04	-1.48E-04	-1.61E-04	-1.72E-04
41	-1.13E-04	-1.25E-04	-1.37E-04	-1.50E-04	-1.62E-04	-1.74E-04
42	-1.14E-04	-1.26E-04	-1.38E-04	-1.51E-04	-1.63E-04	-1.75E-04
43	-1.15E-04	-1.27E-04	-1.40E-04	-1.52E-04	-1.65E-04	-1.76E-04
44	-1.17E-04	-1.28E-04	-1.41E-04	-1.53E-04	-1.66E-04	-1.78E-04
45	-1.18E-04	-1.30E-04	-1.42E-04	-1.55E-04	-1.67E-04	-1.79E-04
46	-1.19E-04	-1.31E-04	-1.43E-04	-1.56E-04	-1.68E-04	-1.80E-04
47	-1.20E-04	-1.32E-04	-1.44E-04	-1.57E-04	-1.69E-04	-1.81E-04
48	-1.21E-04	-1.33E-04	-1.45E-04	-1.58E-04	-1.71E-04	-1.83E-04
49	-1.22E-04	-1.34E-04	-1.47E-04	-1.59E-04	-1.72E-04	-1.84E-04
50	-1.23E-04	-1.35E-04	-1.48E-04	-1.60E-04	-1.73E-04	-1.85E-04
51	-1.24E-04	-1.36E-04	-1.49E-04	-1.61E-04	-1.74E-04	-1.86E-04
52	-1.25E-04	-1.37E-04	-1.50E-04	-1.62E-04	-1.75E-04	-1.87E-04
53	-1.26E-04	-1.38E-04	-1.51E-04	-1.63E-04	-1.76E-04	-1.88E-04
54	-1.27E-04	-1.39E-04	-1.52E-04	-1.64E-04	-1.77E-04	-1.89E-04
55	-1.28E-04	-1.40E-04	-1.53E-04	-1.65E-04	-1.78E-04	-1.90E-04
56	-1.29E-04	-1.41E-04	-1.54E-04	-1.66E-04	-1.79E-04	-1.91E-04
57	-1.30E-04	-1.42E-04	-1.55E-04	-1.67E-04	-1.80E-04	-1.92E-04
58	-1.31E-04	-1.43E-04	-1.56E-04	-1.68E-04	-1.81E-04	-1.93E-04
59	-1.32E-04	-1.44E-04	-1.56E-04	-1.69E-04	-1.82E-04	-1.94E-04
60	-1.33E-04	-1.45E-04	-1.57E-04	-1.70E-04	-1.83E-04	-1.95E-04
61	-1.34E-04	-1.46E-04	-1.58E-04	-1.71E-04	-1.84E-04	-1.96E-04
62	-1.35E-04	-1.47E-04	-1.59E-04	-1.72E-04	-1.85E-04	-1.97E-04
63	-1.36E-04	-1.47E-04	-1.60E-04	-1.73E-04	-1.85E-04	-1.98E-04
64	-1.37E-04	-1.48E-04	-1.61E-04	-1.74E-04	-1.86E-04	-1.99E-04
65	-1.37E-04	-1.49E-04	-1.62E-04	-1.75E-04	-1.87E-04	-1.99E-04
66	-1.38E-04	-1.50E-04	-1.63E-04	-1.75E-04	-1.88E-04	-2.00E-04
67	-1.39E-04	-1.51E-04	-1.63E-04	-1.76E-04	-1.89E-04	-2.01E-04
68	-1.40E-04	-1.52E-04	-1.64E-04	-1.77E-04	-1.90E-04	-2.02E-04
69	-1.41E-04	-1.52E-04	-1.65E-04	-1.78E-04	-1.90E-04	-2.03E-04
70	-1.42E-04	-1.53E-04	-1.66E-04	-1.79E-04	-1.91E-04	-2.04E-04
71	-1.42E-04	-1.54E-04	-1.67E-04	-1.79E-04	-1.92E-04	-2.04E-04
72	-1.43E-04	-1.55E-04	-1.67E-04	-1.80E-04	-1.93E-04	-2.05E-04
73	-1.44E-04	-1.56E-04	-1.68E-04	-1.81E-04	-1.94E-04	-2.06E-04
74	-1.45E-04	-1.56E-04	-1.69E-04	-1.82E-04	-1.94E-04	-2.07E-04
75	-1.46E-04	-1.57E-04	-1.70E-04	-1.82E-04	-1.95E-04	-2.07E-04
76	-1.46E-04	-1.58E-04	-1.70E-04	-1.83E-04	-1.96E-04	-2.08E-04

77	-1.47E-04	-1.59E-04	-1.71E-04	-1.84E-04	-1.97E-04	-2.09E-04
78	-1.48E-04	-1.59E-04	-1.72E-04	-1.85E-04	-1.97E-04	-2.10E-04
79	-1.49E-04	-1.60E-04	-1.73E-04	-1.85E-04	-1.98E-04	-2.10E-04
80	-1.49E-04	-1.61E-04	-1.73E-04	-1.86E-04	-1.99E-04	-2.11E-04
81	-1.50E-04	-1.62E-04	-1.74E-04	-1.87E-04	-1.99E-04	-2.12E-04
82	-1.51E-04	-1.62E-04	-1.75E-04	-1.87E-04	-2.00E-04	-2.12E-04
83	-1.52E-04	-1.63E-04	-1.75E-04	-1.88E-04	-2.01E-04	-2.13E-04
84	-1.52E-04	-1.64E-04	-1.76E-04	-1.89E-04	-2.01E-04	-2.14E-04
85	-1.53E-04	-1.64E-04	-1.77E-04	-1.89E-04	-2.02E-04	-2.14E-04
86	-1.54E-04	-1.65E-04	-1.77E-04	-1.90E-04	-2.03E-04	-2.15E-04
87	-1.54E-04	-1.66E-04	-1.78E-04	-1.91E-04	-2.03E-04	-2.16E-04
88	-1.55E-04	-1.66E-04	-1.79E-04	-1.91E-04	-2.04E-04	-2.16E-04
89	-1.56E-04	-1.67E-04	-1.79E-04	-1.92E-04	-2.05E-04	-2.17E-04
90	-1.56E-04	-1.68E-04	-1.80E-04	-1.93E-04	-2.05E-04	-2.18E-04
91	-1.57E-04	-1.68E-04	-1.81E-04	-1.93E-04	-2.06E-04	-2.18E-04
92	-1.58E-04	-1.69E-04	-1.81E-04	-1.94E-04	-2.07E-04	-2.19E-04
93	-1.58E-04	-1.70E-04	-1.82E-04	-1.95E-04	-2.07E-04	-2.19E-04
94	-1.59E-04	-1.70E-04	-1.83E-04	-1.95E-04	-2.08E-04	-2.20E-04
95	-1.60E-04	-1.71E-04	-1.83E-04	-1.96E-04	-2.08E-04	-2.21E-04
96	-1.60E-04	-1.72E-04	-1.84E-04	-1.96E-04	-2.09E-04	-2.21E-04
97	-1.61E-04	-1.72E-04	-1.84E-04	-1.97E-04	-2.09E-04	-2.22E-04
98	-1.62E-04	-1.73E-04	-1.85E-04	-1.98E-04	-2.10E-04	-2.22E-04
99	-1.62E-04	-1.73E-04	-1.86E-04	-1.98E-04	-2.11E-04	-2.23E-04
100	-1.63E-04	-1.74E-04	-1.86E-04	-1.99E-04	-2.11E-04	-2.23E-04
101	-1.64E-04	-1.75E-04	-1.87E-04	-1.99E-04	-2.12E-04	-2.24E-04
102	-1.64E-04	-1.75E-04	-1.87E-04	-2.00E-04	-2.12E-04	-2.24E-04
103	-1.65E-04	-1.76E-04	-1.88E-04	-2.00E-04	-2.13E-04	-2.25E-04
104	-1.65E-04	-1.76E-04	-1.88E-04	-2.01E-04	-2.13E-04	-2.26E-04
105	-1.66E-04	-1.77E-04	-1.89E-04	-2.01E-04	-2.14E-04	-2.26E-04
106	-1.67E-04	-1.78E-04	-1.90E-04	-2.02E-04	-2.14E-04	-2.27E-04
107	-1.67E-04	-1.78E-04	-1.90E-04	-2.03E-04	-2.15E-04	-2.27E-04
108	-1.68E-04	-1.79E-04	-1.91E-04	-2.03E-04	-2.15E-04	-2.28E-04
109	-1.68E-04	-1.79E-04	-1.91E-04	-2.04E-04	-2.16E-04	-2.28E-04
110	-1.69E-04	-1.80E-04	-1.92E-04	-2.04E-04	-2.16E-04	-2.29E-04
111	-1.70E-04	-1.80E-04	-1.92E-04	-2.05E-04	-2.17E-04	-2.29E-04
112	-1.70E-04	-1.81E-04	-1.93E-04	-2.05E-04	-2.18E-04	-2.30E-04

According the CEB MC90-99 model solution the amount of total shrinkage is increasing with increasing concrete strength, while drying shrinkage is decreasing with decreasing water content in high strength concrete (Fig. App1).

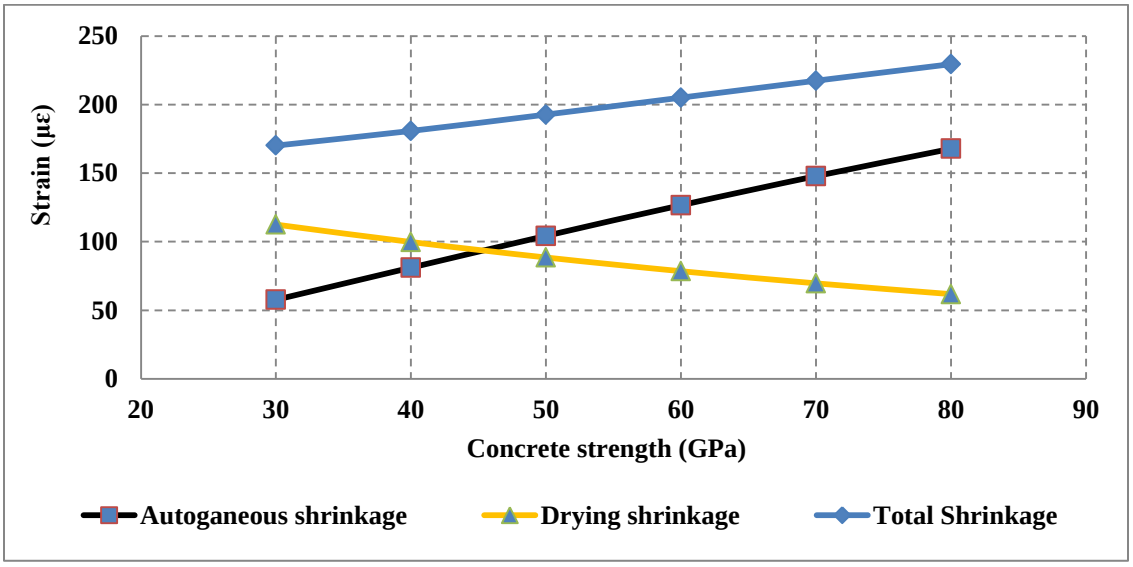

Fig. A-1: The final calculated shrinkage for different concrete strength (CEB MC90-99 model solution).

APPENDIX B

CALCULATION OF FINAL CRACK WIDTH AND REINFORCEMENT STRAIN

B-1 GILBERTS PREDICTION MODEL

In this part, the crack width and bar strain for GFRP-RC bridge deck slabs subjected to shrinkage are predicted based on analytical model developed for steel-RC members (Gilbert 1992).

Determination of final crack width and bar stress at cracking location using Gilbert's model (Gilbert 1992) for all slabs:

Table B-1: Input data for parameters used in Gilbert's model

Slab	***L*** **(mm)**	***t*** **(mm)**	A_{GFRP} **(mm2)**	d_b **(mm)**	ϕ^*	ε^*_{sh}	$f_{t\,(7)}$ **(MPa)**	$f_{t\,(28)}$ **(MPa)**	$f_{c\,(3)}$ **(MPa)**	$f_{c\,(28)}$ **(MPa)**	$E_{c\,(3)}$ **(MPa)**	$E_{c\,(28)}$ **(MPa)**	E_{GFRP} **(MPa)**	$f_{t\,(GFRP)}$ **(MPa)**
SG1	2500	180	284	9.5	0.6	-3.48e-4	3.4	3.7	25	38	20200	21800	74351	1572
SG2	2500	180	508	12.7	0.6	-3.48e-4	3.4	3.7	25	38	20200	21800	69607	1759
SG3	2500	180	764	15.9	0.6	-3.48e-4	3.4	3.7	25	38	20200	21800	68297	1725
SG4	2500	180	1140	19.1	0.6	-3.48e-4	3.4	3.7	25	38	20200	21800	65374	1484
S	2500	180	508	16	0.6	-3.48e-4	3.4	3.7	25	38	20200	21800	200000	f_y:546
G-WD	2500	180	764	15.9	0.6	-4e-4(dry) 2.86(wet)	3.4	3.7	25	41	20200	22200	68297	1725
G-FT	2500	180	1140	15.9	0.6	-2.84e-4(thaw) -2.6e-4(freeze)	3.4	3.7	25	35	20200	21000	68297	1725

For specimen SG1:

The concrete area and reinforcement ratio are:

$$A_c = A_{gross} - A_S = 765 \times 180 - 792 = 136908 \text{ mm}^2$$

$$\rho = {A_s}/{A_c} = 0.00578$$

The modular ratio is

$$n = {E_s}/{E_c^{(3)}} = {69607}/{20200} = 3.44$$

The distance S_0, over which the concrete and reinforcement stress vary is given by:

$$S_0 = {d_b}/{10\rho} = 275 \text{ mm}$$

The final effective modulus is

$$E_e^* = {E_c^{(3)}}/{1 + \varphi^*} = {20200}/{1 + 0.6} = 12625 \text{ MPa}$$

And the corresponding effective modular ratio is

$$n^* = {E_s}/{E_e^*} = {69607}/{12625} = 5.51$$

The ratio C_1 is given by

$$c_1 = \frac{2S_0}{3L - 2S_0} = \frac{2\times275}{3\times2500 - 2\times275} = 0.0790$$

And the restraining force immediately after first cracking is obtained by

$$\mathrm{N_{cr}} = \frac{\mathrm{n\rho f_t A_c}}{\mathrm{C_1 + n\rho(1+C_1)}} = \frac{3.44\times0.00578\times3.24\times136908}{0.079 + 3.44\times0.00578\times(1+0.079)} = 87895.30483 \text{ N}$$

The concrete stress away from the crack immediately after first cracking is given by:

$$\sigma_{c1} = \frac{(1+C_1)N_{cr}}{A_c} = \frac{87895.3(1+0.079)}{136908} = 0.6928$$

And the estimate of the average concrete stress in the period after first cracking is given by:

$$\sigma_{av} = \frac{\sigma_{c1} + f_t}{2} = \frac{0.6928 + 3.24}{2} = 1.96639$$

For long-term calculations, the final value for S_0 over which the concrete and bars stress vary, is given by:

$$S_0 = \frac{1.33d_b}{10\rho} = 365.55 \text{ mm}$$

The final restraining force is

$$N_{(\infty)} = \frac{-3A_s n^* E_s \Delta u}{2s_0 m} - \frac{(3L - 2s_0 m)n^* A_s}{2s_0 m}(\sigma_{av} + \varepsilon^*_{sh} E^*_e) = 48176.3 \text{ N}$$

The final bar stress at cracking obtained by

$$\sigma^*_{s2} = \frac{N_{(\infty)}}{A_s} = 60.83 \text{ MPa}$$

The final bar stress away from crack in obtained by

$$\sigma^*_{s1} = \frac{-2S_0 m}{3l - 2S_0 m}\sigma^*_{s2} + \frac{3\Delta u E_s}{3l - 2S_0 m} = -13.4 \text{ MPa}$$

The final concrete stress away from crack is obtained by

$$\sigma^*_{c1} = \frac{N(\infty) - \sigma^*_{s1} A_s}{A_c} = 0.43 \text{ MPa}$$

The final crack width is now calculated by

$$w = -\left[\frac{\sigma^*_{c1}}{E^*_e}\left(s - \frac{2}{3}S_0\right) + \varepsilon^*_{sh} S\right] = 0.39 \text{ mm}$$

Table B-2: The intermediate calculations for the theoretical predictions of crack width and the stress on the GFRP bars

Increment	Specimen	Experimental		Theoretical		Error %	
		Bar stress at cracking (Mpa)	Crack width (mm)	Bar stress at cracking (Mpa)	Crack width (mm)	Bar stress at cracking	Crack width
0.1	S1	279	0.73	1314	0.39	371	46
	S2	173	0.64	1601	-0.21	828	133
	S3	104	0.33	890	0.02	758	95
	S4	66	0.24	658	-0.01	902	103
0.2	S1	279	0.73	649	0.63	133	13
	S2	173	0.64	794	0.33	360	48
	S3	104	0.33	439	0.23	323	32
	S4	66	0.24	323	0.14	392	41
0.3	S1	279	0.73	428	0.71	53	3
	S2	173	0.64	525	0.51	204	20
	S3	104	0.33	288	0.30	178	10
	S4	66	0.24	212	0.19	222	20
0.4	S1	279	0.73	317	0.75	14	3
	S2	173	0.64	390	0.60	126	6
	S3	104	0.33	213	0.33	105	0
	S4	66	0.24	156	0.22	138	10
0.5	S1	279	0.73	250	0.78	10	6
	S2	173	0.64	309	0.65	79	2
	S3	104	0.33	168	0.35	62	7
	S4	66	0.24	123	0.23	87	4
0.6	S1	279	0.73	206	0.79	26	8
	S2	173	0.64	255	0.69	48	8
	S3	104	0.33	138	0.37	33	11
	S4	66	0.24	100	0.24	53	0
0.7	S1	279	0.73	175	0.80	37	10
	S2	173	0.64	217	0.72	26	12
	S3	104	0.33	116	0.38	12	14
	S4	66	0.24	84	0.25	28	3
0.8	S1	279	0.73	151	0.81	46	11
	S2	173	0.64	188	0.74	9	15
	S3	104	0.33	100	0.38	4	16
	S4	66	0.24	72	0.25	10	5
0.9	S1	279	0.73	132	0.82	53	12
	S2	173	0.64	166	0.75	4	17
	S3	104	0.33	88	0.39	16	18
	S4	66	0.24	63	0.26	4	7
1	S1	279	0.73	118	0.82	58	13
	S2	173	0.64	148	0.76	14	19
	S3	104	0.33	78	0.39	25	19
	S4	66	0.24	56	0.26	15	9
1.1	S1	279	0.73	106	0.83	62	13
	S2	173	0.64	133	0.77	23	21
	S3	104	0.33	69	0.40	33	20
	S4	66	0.24	50	0.26	25	10
1.2	S1	279	0.73	95	0.83	66	14
	S2	173	0.64	121	0.78	30	22
	S3	104	0.33	62	0.40	40	21
	S4	66	0.24	44	0.27	32	11
1.3	S1	279	0.73	87	0.83	69	14
	S2	173	0.64	111	0.79	36	23
	S3	104	0.33	57	0.40	45	22
	S4	66	0.24	40	0.27	39	11
1.33	S1	279	0.73	85	0.84	70	14
	S2	173	0.64	108	0.79	38	23
	S3	104	0.33	55	0.40	47	22
	S4	66	0.24	39	0.27	41	12
1.4	S1	279	0.73	80	0.84	71	15
	S2	173	0.64	102	0.79	41	24
	S3	104	0.33	52	0.41	50	23
	S4	66	0.24	37	0.27	44	12
1.5	S1	279	0.73	73	0.84	74	15
	S2	173	0.64	94	0.80	46	25
	S3	104	0.33	47	0.41	54	24
	S4	66	0.24	33	0.27	49	13